Master's thesis

NTNU
Norwegian University of Science and Technology
Faculty of Natural Sciences
Department of Materials Science and Engineering

Olav Wadseth Sandvik

Domain Engineering in Polycrystalline $ErMnO_3$ Using Strain- and Electrical Fields

Master's thesis in TMT4900 Materials Chemistry and Energy Technology
Supervisor: Prof. Dennis Gerhard Meier
Co-supervisor: Dr. Jan Schultheiß

June 2022

NTNU
Norwegian University of
Science and Technology

Olav Wadseth Sandvik

Domain Engineering in Polycrystalline $ErMnO_3$ Using Strain- and Electrical Fields

Master's thesis in TMT4900 Materials Chemistry and Energy Technology
Supervisor: Prof. Dennis Gerhard Meier
Co-supervisor: Dr. Jan Schultheiß
June 2022

Norwegian University of Science and Technology
Faculty of Natural Sciences
Department of Materials Science and Engineering

NTNU
Norwegian University of
Science and Technology

Preface

This master's thesis was written as the concluding part of a Master's degree in Chemical Engineering and Biotechnology at the Norwegian University of Science and Technology (NTNU). The work presented was carried out within the Functional Materials and Materials Chemistry group (FACET) at the Department of Materials Science and Engineering, more specifically, in the Functional Topological Systems Group (FUNTOPS). Prof. Dr. Dennis Meier has been my main supervisor, and Dr. Jan Schultheiß my co-supervisor.

I want to thank my supervisors for including me in FUNTOPS, especially since the original master's project was abruptly terminated. I was lucky to be included in such a welcoming and supportive group, where I could discuss my findings with the knowledgeable members. My main supervisor, Dennis Meier, deserves thanks for giving me the opportunity to dive deep into the field of ferroelectrics and for helping me stay motivated throughout the semester. I would also like to thank my co-supervisor, Jan Schultheiß, for his guidance and great feedback as my thesis took shape. His flexibility and engagement made meeting up and discussing both results and theory easy. I could not have asked for a better co-supervisor. Jan also gave me training on the piezoresponse force microscope (PFM) and supplied the samples investigated in the thesis.

There are also others who deserve thanks for helping me with my thesis. First of all, I would like to thank all the members of FACET who supplied valuable input as I presented my results in group meetings. I would also like to give extra thanks to specific individuals who helped me in other ways. Thank you, Jiali He, who helped me image my samples with the SEM in the NanoLab, Ivan Ushakov, who helped me with resonance PFM, and Leonie Richarz, who helped me with conductive atomic force microscopy (cAFM). From outside the group, I would also like to thank Håkon Wiik Ånes for his invaluable help with the electron backscatter diffraction (EBSD) data acquisition and analysis. Lastly, I would also like to thank our two collaborators. First, Tadej Rojac from the Jožef Stefan Institute in Slovenia, who annealed the samples, and second, Kyle Kelley from Oak Ridge National Laboratory in Tennessee, the United States of America, who helped me investigate the impact of electric fields on the $ErMnO_3$ samples. Last but not least, I want to thank my family, friends, and my dear Jenny for their love and support this last semester.

The scanning electron microscope (SEM) images included in this thesis were acquired in the NanoLab at NTNU with financial support from the Norwegian Research Council (NRC) and the Norwegian Micro- and Nanofabrication Facility (NorFab). Switching spectroscopy piezoresponse force microscopy (SS-PFM) data was acquired at Oak Ridge National Laboratory in Tennessee, United States of America, in collaboration with Kyle Kelley.

Trondheim, June 16th 2022

Olav Wadseth Sandvik

Abstract

Engineering of ferroelectric domains is crucial for utilizing ferroelectric materials as electronic components such as capacitors, sensors, and transducers. At present, ferroelectric domains can be controlled through chemical doping, microstructural engineering, and by applying electric fields. Still, the techniques have varying results based on the model system, and the mechanisms often remain to be explored in detail. The aim of this thesis is to investigate two parameters; the impact of applied mechanical pressure and the impact of electric fields on the ferroelectric domain structure of polycrystalline $ErMnO_3$.

To accomplish the first part of the goal, three samples were annealed under different uniaxial pressures, 0 MPa, 24 MPa, and 47 MPa. Then the micro- and nanostructure of both the in-plane and out-of-plane faces of the samples were inspected with piezoresponse force microscopy and electron backscatter diffraction. The second part of the goal was accomplished by examining a polycrystalline $ErMnO_3$ sample without the thermomechanical treatment with switching spectroscopy piezoresponse force microscopy.

The experiments demonstrated that the higher applied uniaxial pressures resulted in more and narrower striped domains and a new domain structure referred to as ”ripped domains”. Furthermore, it was found that the orientation of the grains had a significant impact on the formation of the domains, and that intergranular stresses also play a role. In contrast, the influence of electrical fields was found to be small in the investigated range. The electric fields applied to the polycrystalline sample did not result in polarization reversal, nor was any conclusive domain wall movement detected.

Based on the results, it is concluded that the most viable option for controlling the domain structure in $ErMnO_3$ is by utilizing stress. Future work should focus on improving the understanding of the local strain fields in the polycrystalline sample and their effect on the domain structures. This could be done by utilizing finite element simulations that can capture the strains induced by neighboring grains and the orientation of the grains. Another exciting path would be to probe the ripped domains with aberration-corrected high-angle annular-dark-field imaging to gain insight into the mechanism responsible for their formation. The research presented in this thesis is part of a larger search for new domain engineering strategies enabling greater control of ferroelectric properties. This contributes not only to the betterment of devices relying on ferroelectrics such as capacitors, sensors, and transducers but also to the understanding of fundamental physics.

Sammendrag

Utforming av ferroelektriske domener er avgjørende for å bruke ferroelektriske materialer som elektroniske komponenter, eksempelvis kondensatorer, sensorer og transdusere. For tiden kan ferroelektriske domener kontrolleres gjennom kjemisk doping, mikrokonstruksjon og ved å bruke elektriske felt. Likevel har metodene varierende resultater basert på materialet, og mekanismene bak er ikke fullstendig forstått. Målet med denne oppgaven er å undersøke to parametere; virkningen av påført mekanisk trykk og virkningen av elektriske felt på den ferroelektriske domenestrukturen til polykrystallinsk $ErMnO_3$.

Den første delen av målet ble oppnådd ved å gløde tre prøver under forskjellige belastninger, 0 MPa, 24 MPa, 47 MPa, og deretter inspisere mikro- og nanostrukturen både i planet og ut av planet ved bruk av piezorespons kraftmikroskopi og elektron bakspredningsdiffraksjon. Den andre delen av målet ble oppnådd ved å undersøke en polykrystallinsk $ErMnO_3$ prøve uten termomekanisk behandling med vekslingsspektroskopi piezorespons kraftmikroskopi.

Eksperimentene viste at de høyere belastningene resulterte i flere og smalere stripete domener og en ny domenestruktur referert til som "revnede domener". Videre ble det bestemt at orienteringen av kornene hadde en betydelig innvirkning på dannelsen av domenene, og at intergranulære spenninger også spiller en rolle. Effekten av elektriske felt var derimot liten i det undersøkte området. De elektriske feltene påført den polykrystallinske prøven resulterte ikke i polarisasjonsreversering, og det ble heller ikke oppdaget noen klar domeneveggbevegelse.

Basert på resultatene, konkluderes det med at det beste alternativet for å kontrollere domenestrukturen i $ErMnO_3$ er ved å utnytte stress. Fremtidig arbeid bør fokusere på å øke forståelsen av de lokale tøyningene i den polykrystallinske prøven og deres effekt på domenestrukturen. Dette kan gjøres ved å bruke endelige element-simuleringer som kan simulere tøyningene som oppstår i korn på grunn av nabokorn samt orienteringen til kornene. En annen spennende vei videre ville vært å undersøke de revnede domenene med aberrasjonskorrigert høyvinklet ringformet-mørkefelt-avbildning for å få innsikt i mekanismen som er ansvarlig for dannelsen deres. Forskningen som presenteres i denne masteroppgaven er en del av et større søk etter nye metoder for å utforme ferroelektriske domener for økt kontroll av de ferroelektriske egenskapene. Dette bidrar ikke bare til forbedring av komponenter som er avhengige av ferroelektriske materialer, eksempelvis kondensatorer, sensorer og transdusere, men også til grunnforskning innen fysikk.

Abbreviations

AFM - Atomic force microscopy

AP - Pure antiphase

BLD - Blob-like domain

DFT - Density functional theory

FE - Pure ferroelectric

FWHM - Full width at half maximum

HAADF - Aberration-corrected high-angle annular-dark-field

HAADF-STEM - High-angle annular-dark-field scanning transmission electron microscopy

OR-sample - Oak Ridge sample

PCA - Principal component analysis

PFM - Piezoresponse force microscopy

PN - Plane normal

PVL - Piezoresponse-voltage loop

RMS - Root mean square

SEM - Scanning electron microscopy

SPM - Scanning probe microscopy

SS-PFM - Switching spectroscopy piezoresponse force microscopy

STM - Scanning transmission microscopy

$\boldsymbol{T_C}$ - Curie temperature

XRD - X-ray diffraction

Table of Contents

List of Figures

Chapter 1

Introduction

1.1 Background and motivation

Since the discovery of ferroelectricity in 1920 [1], ferroelectric materials have found applications in several industries as high-dielectric-constant capacitors, ultrasonic transducers, room-temperature magnetic field detectors, high-density non-volatile memories, and much more [2, 3]. What makes ferroelectrics unique in comparison to all other polar materials is their switchable spontaneous polarization which is analogous to the switchable magnetization of ferromagnets [4]. Furthermore, the macroscopic properties of a ferroelectric can be controlled through domain engineering, which gives rise to great variation of properties even within chemically homogeneous ferroelectrics [5–11].

Improper ferroelectrics are a particularly interesting sub-group of ferroelectrics. In improper ferroelectrics, ferroelectricity arises as a by-product of structural or magnetic instabilities breaking the inversion symmetry of the unit cell [7]. Because the ferroelectricity is coupled to properties other than polarization, improper ferroelectrics have additional functionality such as multiferroic hybrid domain walls [12] and stabilized charged domain walls [13]. These additional functionalities make improper ferroelectrics possible candidates for exiting future applications such as domain wall nanoelectronics and next-generation capacitors [7, 14].

In some improper ferroelectric materials, vortex structures and charged domain walls, shown in Figure 1.1.1, form naturally [7, 15]. These topologically protected defects can be as small as a few nanometers and can have properties not found in the bulk of the ferroelectric [7, 15, 16]. Because of this, they can function as information carriers and electrical components and thus contribute to the miniaturization and energy effectiveness of electronics [17–19].

Ferroelectric vortices have recently drawn interest in several ferroelectric materials, including hexagonal tungsten bronzes [20], hexagonal ferrites [21], hexagonal gallates [22], and hexagonal manganites [13]. As shown in Figure 1.1.1, the vortices are situated at points where six domains meet. Investigation of the vortices has found that they host unusual electrostatics and that they prevent the complete poling of the ferroelectric domain structure by remaining stationary and preventing the collapse of the domains [15, 23]. These attributes make vortices useful for domain engineering, and possibly information storage [18, 19]. Despite the vortices not yet being fully understood, they have already found possible uses. For instance, in fundamental research where they have been used to test cosmological scaling laws [24–26].

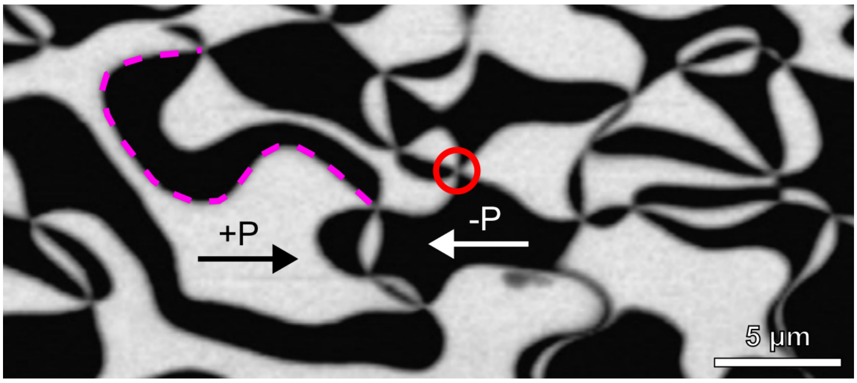

Figure 1.1.1: Ferroelectric domains in $ErMnO_3$ with different polarizations, $-P$ and $+P$ in black and white, respectively. A vortex core and a domain wall are indicated by a red circle and a dashed magenta line, respectively. Adapted from ref. [27].

Thus far, methods for engineering ferroelectric domains include flexoelectricity induced by large local strain gradients [28], thin-film thickness [29], chemical doping [30], epitaxial strain [31], dislocations [32], annealing [33] and electric fields [23]. In addition, it was recently discovered that vortex cores could be moved under the influence of non-uniform strain in improper ferroelectrics [34]. This discovery holds promise for domain engineering in hexagonal manganites by using the vortices to customize the ferroelectric domain structure. However, much is still unknown about utilizing vortex cores for domain engineering.

1.2 Aim and scope of the work

The aim of this master thesis is to investigate the impact of mechanical pressure and electric fields on the domain structure of polycrystalline $ErMnO_3$. Therefore, the study is divided into two parts pertaining to each of these influences.

The impact of mechanical pressure is investigated by applying three different pressures: 0 MPa, 24 MPa, and 47 MPa to the polycrystalline sample during the phase transition from paraelectric to ferroelectric. Then the ferroelectric domain structure is characterized through piezoresponse force microscopy (PFM) and scanning electron microscopy (SEM). Further investigation compares the orientation of the grains and the resulting domain structure by utilizing electron backscatter diffraction (EBSD). The impact of electric fields on the domain structure is probed through switching spectroscopy piezoresponse force microscopy (SS-PFM) and machine learning approaches.

Chapter 2

Theoretical background

2.1 Ferroic materials

Order parameter
The word *ferroic* brings associations of iron because of the original iron-containing ferromagnets, Fe_3O_4, discovered 2500 years ago [35]. Since then, many ferromagnets that do not contain iron have been discovered, such as YCo_5, Cu_2MnSn, or $MnNi_3$. Indeed, a ferromagnet does not necessarily contain iron, nor does a ferroic material. The definition of a ferroic is a material that develops a spontaneous alignment of an order parameter, η, resulting in a macroscopic property that can be switched by an external conjugate field [36]. The order parameter is the physical quantity fully responsible for the ferroic phase transition, in which the crystal transitions from a high symmetry prototype phase with point group G to the lower symmetry ferroic phase with point group F [37]. The phase transition happens at a critical temperature, T_c, known as the Curie temperature, and is non-disruptive, meaning that no chemical bonds are broken. As a result, the symmetry elements of the ferroic phase are always a subgroup of the symmetry elements of the prototype phase [38, 39]. The change in symmetry elements from point group G to point group F can be used to predict the number of orientations, q, the order parameter can have in the ferroic state. This is calculated by the following fraction $q = |G|/|F|$, where $|A|$ is the number of symmetry operations, including the identity transformation, in point group A. For all ferroic phase transitions, q will be larger or equal to 2 [37, 39].

Primary ferroics
Currently, four primary ferroic order parameters are known [7]. These are magnetization in ferromagnets, polarization in ferroelectrics, strain in ferroelastics, and toroidal moment in ferrotoroidics. These order parameters are switchable by their respective conjugate fields; magnetic, electric, strain, and toroidal fields [7, 39–41]. The primary ferroic orders can be classified based on whether or not they break space- and/or time-inversion symmetry, as seen in Figure 2.1.1, under the parity operations. The figure illustrates that ferroelectricity breaks space-inversion symmetry, ferromagnetism breaks time-inversion symmetry, ferroelasticity breaks neither, and ferrotoroidicity breaks both [36, 41]. For a crystal to exhibit a primary ferroic order,

it must have the correct crystal structure. This is clear from Neumann's principle, which states: "The symmetry of any physical property of a crystal must include the symmetry elements of the point group of the crystal" [39]. An example of this is ferromagnetism, which only exists in crystal structures where time-inversion symmetry is broken.

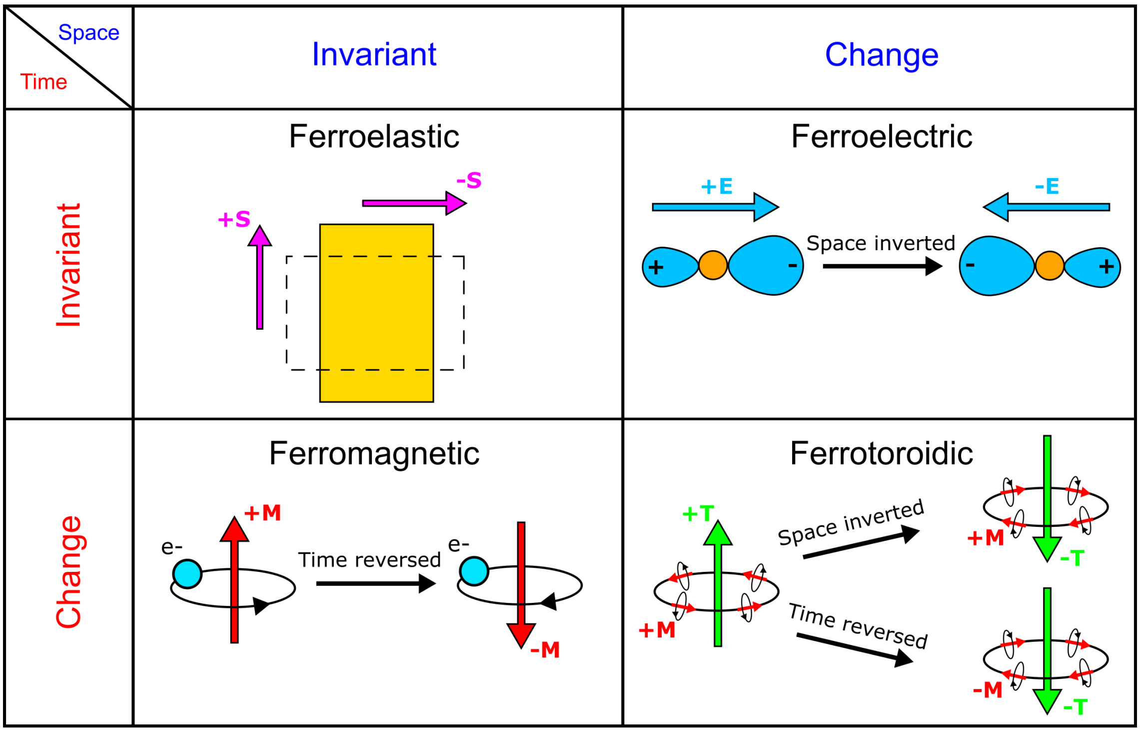

Figure 2.1.1: Primary ferroic orders and their transformations under parity operations. Their order parameters changing sign under the correct symmetry operations. Adapted from ref. [40].

Multiferroics

Materials with more than one primary ferroic order were defined as multiferroics in 1994 by Hans Schmid [42]. Since then, the definition has expanded to include more than just the primary ferroic orders. It now also includes, e.g., antiferromagnetism and multiphase systems [43]. Multiferroics can be divided into type 1 and type 2, depending on whether the ferroic orders emerge individually or jointly. Multiferroics have been sought after since the first half of the twentieth century because the order parameters can be coupled, meaning that the conjugate field of one can influence the other. For example, in some multiferroics with both magnetization and polarization, the magnetic moment can be switched by an electric field, or the polarization by a magnetic field [43, 44].

Domains

Regions with a similar orientation of the order parameter are known as domains [7]. The number of domain states in a ferroic equals q when there is no translational symmetry change between the prototype and ferroic phases. Otherwise, the number of domains, D, equals q multiplied with the number of translational domains, ν: $D = q \cdot \nu$ [37]. An example of this is hexagonal $ErMnO_3$ which has two polarization directions and three translational domains, and thus a total of six domain states.

The interfaces between the domains, known as domain walls, are regions that separate the domains. These domain walls are planar topological defects and can have interesting properties not found in any of the domains [45]. Domains and domain walls will be discussed further in section 2.2 in the context of ferroelectric materials.

2.2 Ferroelectrics

Dielectrics and piezoelectrics

Ferroelectrics are a subgroup of dielectrics and can be found at the bottom of the dielectric hierarchy as illustrated in Figure 2.2.1 [4]. Dielectrics are electrical insulators that can be polarized under the influence of an external electric field. Crystals of all 32 point groups can be dielectric according to Neumann's principle briefly discussed in section 2.1. Piezoelectrics, a subgroup of dielectrics, require a non-centrosymmetric crystal structure, only found in 20 of the point groups. Piezoelectrics are characterized by the development of electric surface charge under the influence of mechanical stress, known as the direct piezoelectric effect, and the development of mechanical strain under the influence of an electric field, known as the converse piezoelectric effect [4, 39]. Both effects are illustrated schematically in Figure 2.2.2.

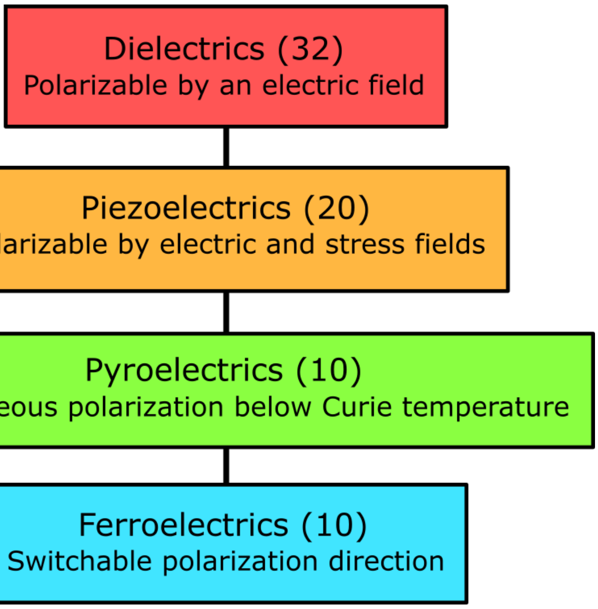

Figure 2.2.1: Symmetry hierarchy showing the relationship between dielectrics, piezoelectrics, pyroelectrics and ferroelectrics. The number of point groups is given in parentheses. Adapted from ref. [4].

Pyroelectrics and ferroelectrics

Pyroelectrics are a subgroup of piezoelectrics and require a crystal structure with a unique polar axis which is only found in 10 of the point groups [4]. In comparison to piezoelectric materials, a spontaneous polarization naturally develops in pyroelectric materials below T_C. If this spontaneous polarization can be switched by an external electric field, the pyroelectric is also a ferroelectric. [4, 39]. Ferroelectrics are divided into two sub-categories based on the origin of the ferroelectricity. The first is proper ferroelectrics, where the electric polarization is the primary symmetry-breaking order parameter. Proper ferroelectrics can further be divided into displacive, and hydrogen-bonded ferroelectrics [39]. The second sub-category is improper ferroelectrics, where the electric polarization arises as a side-effect of structural or magnetic instabilities [7]. Improper ferroelectrics include lone-pair ferroelectrics, geometric ferroelectrics, charge ordering ferroelectrics, and spin-driven ferroelectrics [43].

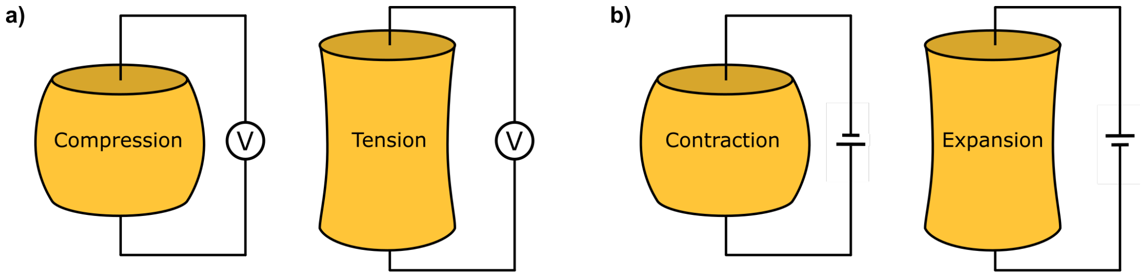

Figure 2.2.2: Visualization of the piezoelectric effects. a) The direct piezoelectric effect, polarization induced by stress, and b) the converse piezoelectric effect, strain induced by electric field. Adapted from ref. [46].

Ferroelectric domains and domain walls

As mentioned in section 2.1, ferroelectric domains are classified by the orientation of their polarizations [7]. In the simplest case, a uniaxial ferroelectric, the domains can have one of two polarization orientations that are separated by 180°. The interfaces between these domains are called 180° domain walls and are illustrated in Figure 2.2.3. In multiaxial ferroelectrics there are domain walls where the polarization orientation differs with less than 180° such as 71°, 90°, and 109° domain walls [7, 47]. At the domain walls, the polarization gradually changes from one domain to the other, as illustrated in Figure 2.2.3 a). How gradual this change is depends on the amplitude of the order parameter and polar defects, and determines the width of the domain wall. Domain wall widths in the range of 0.5 nm to 100 nm have been reported [4, 15, 48, 49].

Ferroelectric domain walls can be either neutral or charged depending on how they are oriented with respect to the spontaneous polarization [48, 50]. Neutral domain walls separate domains with anti-parallel polarization orientations as shown in Figure 2.2.3 b) and carry no charge. Charged domain walls, on the other hand, host uncompensated positive or negative bound charges, which create locally diverging electrostatic potentials. This potential needs to be screened, which drives charge carriers to the domain wall. Charged domain walls are known as head-to-head if the polarization of the adjacent domains points toward the domain wall, as in Figure 2.2.3 c), and tail-to-tail if they point away from it, as in Figure 2.2.3 d). Charged domain walls mainly form in improper ferroelectrics because they are very energetically costly in proper ferroelectrics [7].

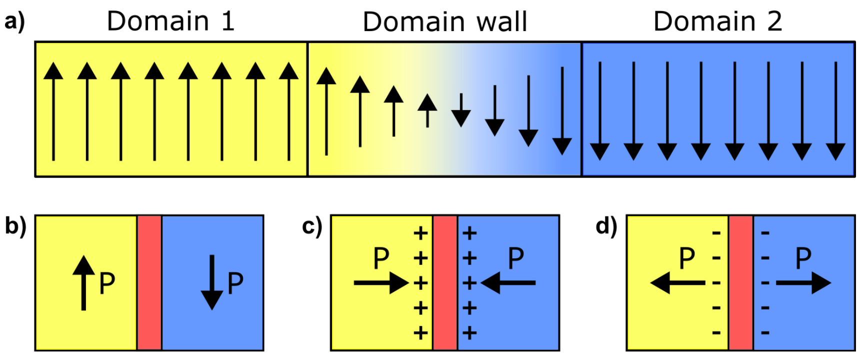

Figure 2.2.3: Schematic illustrations of 180° domain walls. a) Illustration of the gradual change in polarization between two oppositely oriented ferroelectric domains (Ising-type domain wall), b) neutral domain wall, c) positively charged head-to-head wall, and d) negatively charged tail-to-tail wall. The polarization directions are indicated with arrows, and in panel b-d, the domain walls are colored red with positive (+) and negative (-) bound charges indicated. a) is adapted from ref. [46], while b), c), and d) are adapted from ref. [50].

Hysteresis and polarization reversal

All primary ferroics show hysteric behavior under the influence of their respective conjugate fields, which means that all ferroelectrics have a hysteresis loop [38]. A schematic ferroelectric hysteresis loop is illustrated in Figure 2.2.4. The hysteresis loop shows the polarization of the ferroelectric as a function of the applied electric field and is a key characteristic of all ferroelectrics.

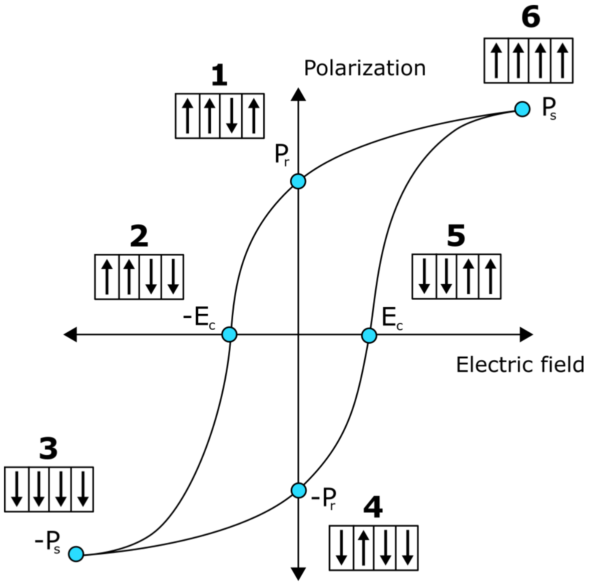

Figure 2.2.4: Schematic illustration of ferroelectric hysteresis loop, with illustrations of domain orientations (indicated by arrows) at each state numbered from 1 to 6.

To explain the correlation between the polarization reversal and the domain state, the simplest case, a uniaxial ferroelectric, is utilized. Assume the ferroelectric is in state 1, where the electric field is zero. In this state, most of the domain volume fraction is oriented the same way, "up," and the ferroelectric has a certain remnant polarization, P_r. Then suppose an electric field is applied anti-parallel to the polarization direction. In that case, the volume fraction of "up" domains will be reduced until the coercive field, $-E_c$, is reached and the net polarization is zero (state 2). Further increasing the electric field strength, the volume fraction of "down" domains will increase until the "down" polarization reaches saturation at $-P_s$ (state 3). Then if the electric field is removed, the polarization will again be reduced to a remnant polarization, $-P_r$, because the volume fraction of "up" domains increases (state 4). If then, an electric field is applied parallel to the "up" orientation, the net polarization will again become zero at the coercive field, E_c (state 5), and then reach saturation at P_s (state 6) [4].

The process of switching from one polarization state to another is called polarization reversal [51]. In the simplest case of polarization reversal, an electric field is applied anti-parallel to the domain of a uniaxial mono-domain ferroelectric in order to reverse the domain. The process is illustrated schematically in Figure 2.2.5. The first step is the nucleation of domain nuclei, mainly on the surfaces of the ferroelectric, see Figure 2.2.5 b). Second, the triangle-shaped domains grow through the sample, Figure 2.2.5 c). Third, the domains expand sideways, Figure 2.2.5 d), and fourth the domains coalesce until the polarization in the sample has been reversed, Figures 2.2.5 e) and f). In samples where both domain states are already present, the polarization reversal process starts with the third step, see Figure 2.2.5 d), and the domains mainly expand through domain wall movement. This is because the nucleation and forward growth of the domains is more energetically expensive than the sideways growth [51].

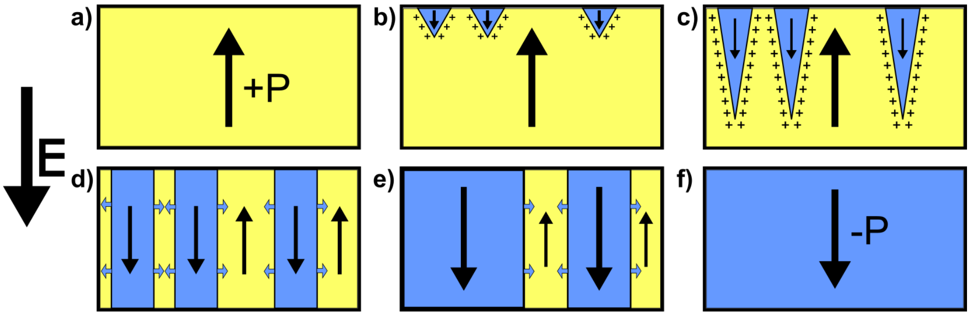

Figure 2.2.5: Schematic illustration of the polarization reversal process in a mono-domain single crystal. a) Mono-domain state with "up" oriented polarization, b) nucleation of new domains, c) forward growth of new domains, d) sideways expansion of new domains, e) coalescence of new domains, and f) mono-domain state with "down" oriented polarization. Adapted from ref. [51].

2.3 Hexagonal manganites

The hexagonal manganites $R\mathrm{MnO}_3$ (R = Sc, Y, In, Dy-Lu) belong to the improper ferroelectrics, which have several interesting properties such as exotic domain structures, conductive domain walls, and multiferroic coupling [13, 23, 52, 53]. Out of the nine hexagonal manganites, YMnO_3 has been studied the most [54]. However, many of the attributes of YMnO_3 can be generalized for the rest of the hexagonal manganites because they are isostructural [55]. As an example, all the hexagonal manganites are type 1 multiferroics, and most of them order antiferromagnetically at temperatures below 130 K in addition to being ferroelectric. The spontaneous polarization of the hexagonal manganites is small compared to many other ferroelectrics. For example, $YMnO_3$ has a spontaneous polarization of $5.6\,\mu C\,cm^{-2}$ [56], while $BaTiO_3$ has a spontaneous polarization of $21\,\mu C\,cm^{-2}$ [57]. In addition, while many ferroelectrics such as $Gd_2(MoO_4)_3$, $BiFeO_3$, and Bi_2WO_6 [58–61] are ferroelastic, $ErMnO_3$ and $YMnO_3$ are co-elastic, meaning that they do not form ferroelastic domain walls to release elastic stresses [22].

Crystal structure

The crystal structure of the hexagonal manganites is described by the polar space group $P6_3cm$, in the ferroelectric phase, at ambient temperatures, and the centrosymmetric space group $P6_3/mmc$, in the paraelectric phase, at temperatures above 1200 K, depending on the R-ion [54, 62]. The crystal structure consists of alternating non-connected layers of trigonal corner-sharing MnO_5 bipyramids and layers of R^{3+} ions. In the paraelectric phase, the bipyramids align along the c-axis, and the R^{3+} ions form a flat layer in the ab-plane as seen in Figure 2.3.1 a). Below T_C, in the ferroelectric phase, the size mismatch between the R^{3+} ions and the bipyramids causes a structural transition, where sets of three bipyramids tilt away from or towards a central R^{3+} ion, resulting in the ferroelectric structure shown in Figure 2.3.1 b). This mechanism, known as geometric ferroelectricity, is illustrated in Figure 2.3.1 c).

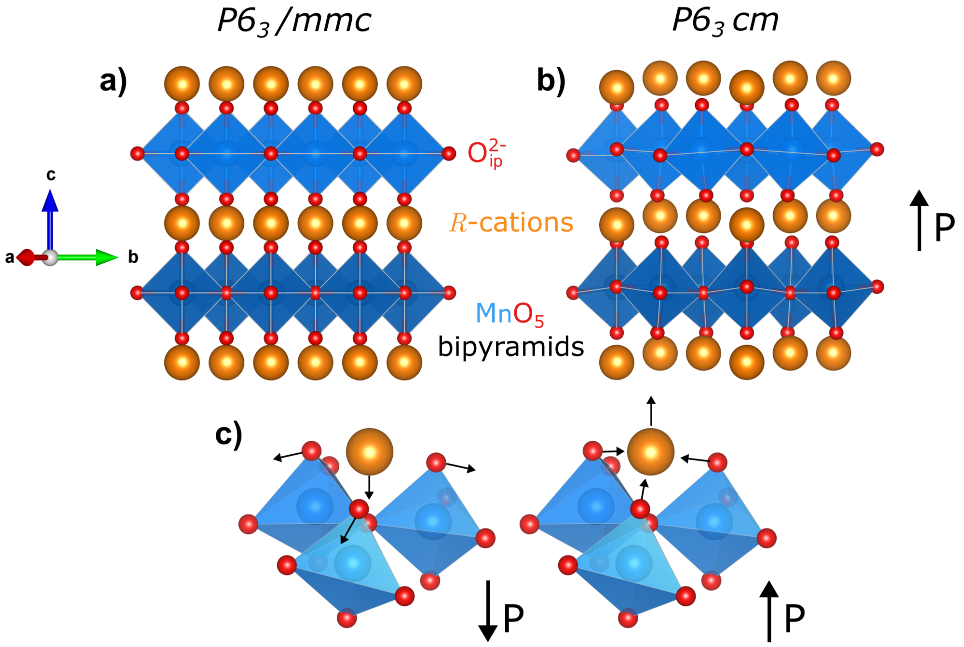

Figure 2.3.1: VESTA illustration of para- and ferroelectric crystal structures along with geometric ferroelectricity. a) The high temperature paraelectric phase $P6_3/mmc$. b) The low temperature ferroelectric phase $P6_3/cm$. c) Illustration of the mechanism behind geometric ferroelectricity. Orange, red and blue spheres represent R^{3+}, O^{2-} and Mn^{3+} ions, respectively. O^{2-}_{ip} refers to the in-plane oxygen ions that connect the bipyramids. a), b), and c) constructed in VESTA [63] using crystallographic data from refs. [64, 65].

The tilting of the bipyramids enlarges the unit cell volume by a factor of three, which is known as trimerization. Because the trimerization can occur at three different R^{3+} ion sites, it gives rise to three translational domains, α, β, and γ as illustrated in Figure 2.3.2 a). The enlarged unit cell is also shown in the ferroelectric phase in Figure 2.3.2 b) [53, 55, 66].

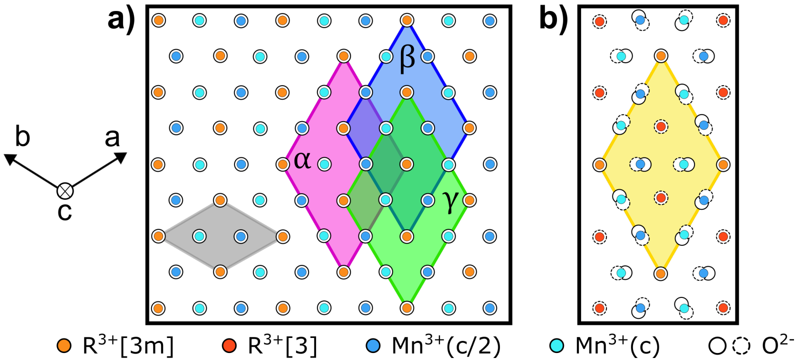

Figure 2.3.2: Schematic illustration of trimerization. a) High-temperature hexagonal manganite structure with the unit cell indicated by a small diamond and three trimerization states indicated by large diamonds. b) Low-temperature hexagonal manganite structure with one unit cell indicated by a large diamond. R^{3+} ions are differentiated by local symmetry and Mn^{3+} ions by location along the c-axis. Adapted from ref. [67].

Transition debate

In 1965, Ismailzade and Kizhaev stated that the transition in $YMnO_3$ from paraelectric to ferroelectric happens at 930 K based on temperature-dependent X-ray diffraction and pyroelectric measurements [68]. The latter was never reproduced. Then contrary evidence was put forth by Lukaszewicz et al., who found that the transition happens at 1270 K [69]. Since then, two hypotheses have been discussed. The first hypothesis involves two separate transitions, one where the structure changes and one where the polarization emerges. The second hypothesis states that the trimerization and the emergence of the polarization occur at the same temperature [53]. This debate was only recently settled through second harmonic generation in 2015 by Lilienblum et al.. They showed that the spontaneous polarization emerges simultaneously with the trimerization at 1259 K [56]. From this it was further concluded that the transition temperature of $ErMnO_3$ was 1429 K [24].

Polarization mechanism

When explaining the emergence of geometric ferroelectricity in hexagonal manganites, it is common to discuss the influence of the phonon modes K_3 and $\mathit{\Gamma}_2^-$ [55, 70]. The symmetry label K_3 represents the tilting of the MnO_5 polyhedra, which causes the trimerization of the unit cell and the corrugation of the R^{3+} ion layers, the latter pertaining to the shift of the R^{3+} ions up and down in a 2:1 or 1:2 ratio as seen in Figure 2.3.1 b). In the regions where the bipyramids tilt towards the central R^{3+} ion, the R^{3+} ions form a $_{\circ\circ}{}^{\circ}$ pattern. Where the bipyramids tilt away from the R^{3+} ion, a $^{\circ\circ}{}_{\circ}$ pattern is formed. The corrugation of the R^{3+} ion layer creates strong local dipole moments with the O_{ip}^{2-} ions, but these moments cancel each other out [53, 55, 70, 71]. Thus, the K_3 mode does not contribute to the spontaneous polarization. However, the instability of the K_3 mode pushes the Γ_2^- mode to a non-zero equilibrium position which in turn shifts the R^{3+} ions additionally with respect to the in-plane oxygen O_{ip}^{2-}, resulting in a net polarization along the z-axis [53, 55, 70, 72]. It is the strong coupling between the $K_3(1)$ and $\Gamma_2^-(\mathrm{TO1})$ lattice modes that is responsible for the polarization observed in the hexagonal manganites. Because the polarization arises from the secondary order parameter, Γ_2^-, and not the primary order parameter, K_3, all hexagonal manganites are said to be improper geometric ferroelectrics as discussed in section 2.1 [70].

Landau description

Landau theory is a phenomenological theory used to describe symmetry-breaking phase transitions [73] and has therefore been used by several researchers to describe improper ferroelectrics [66, 74, 75]. The order parameter of these improper ferroelectrics has at least two components. These are often chosen as the amplitude of the tilting, Q, and the azimuthal orientation of the tilt, Φ, as illustrated in Figure 2.3.3 a) [53]. The free energy of the hexagonal manganite system can be expressed as:

$$f = \frac{a}{2}Q^2 + \frac{b}{2}Q^4 + \frac{Q^6}{6}\left(c + c' \cos 6\Phi\right) - gQ^3P\cos 3\Phi + \frac{g'}{2}Q^2P^2 + \frac{a_P}{2}P^2 \tag{2.1}$$

where P is the local amplitude of the polar mode, and a, b, c, c', g, g' and a_P are calculated through ab inito calculations [66]. Plotting the free energy landscape as a function of the strength, Q, and direction, Φ, of the bipyramidal tilting helps to explain several phenomena, and a contour plot of the free energy is therefore shown in Figure 2.3.3 b). From the plot, it is observed that the free energy has six equidistant minima in the brim of the so-called Mexican hat. These minima represent the six different trimerization states of the ferroelectric phase, $\alpha\pm$, $\beta\pm$, and $\gamma\pm$. Situated in the middle of the hat, at $Q = 0$, is the energy maxima where the system is in the paraelectric phase [53].

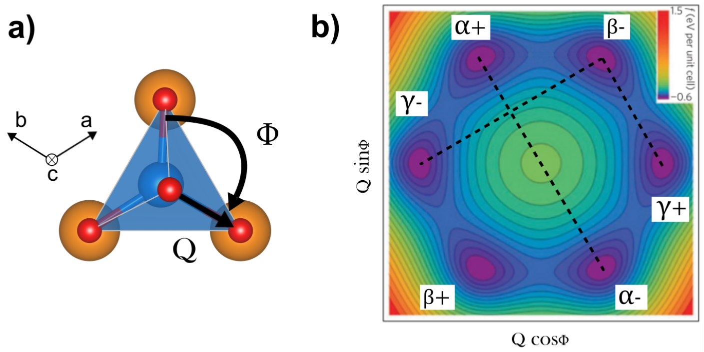

Figure 2.3.3: Schematic illustration of the order parameter components Q and Φ, and a contour plot of the free energy of uniformly trimerized states. a) Bird view of tilting MnO_5 bipyramids and the definition of the components, Q, and Φ, of the order parameter. b) Contour plot of the free energy of uniformly trimerized states as a function of the amplitude, Q, and azimuthal angle, Φ, of the K_3 mode. The dashed lines connecting energy minima correspond to different types of domain walls. a) adapted from ref. [24] and b) adapted from ref. [66].

The presence of the six domain states should, in principle, allow for pure antiphase (AP), pure ferroelectric (FE), and mixed domain walls in the hexagonal manganites. Nevertheless, only the latter has been observed thus far [23, 72]. The absence of the AP and FE domain walls can, however, be explained by looking at Figure 2.3.3 b). From the figure, it is evident that a FE transition between two domain states, such as $\alpha+$ and $\alpha-$, is energetically unfavorable as the structure would have to pass through the paraelectric phase. An AP transition between $\gamma-$ and $\beta-$ would also be unfavorable because the structure would have to pass through a high-energy state as well. That leaves only the transition between adjacent domain states that differ in polarization and translation, such as $\beta-$ and $\gamma+$. These 60° or $1/3\pi$ changes are the most energetically favorable transitions and explain the observed domain sequence: $\alpha+, \beta-, \gamma+, \alpha-, \beta+, \gamma-$, in the hexagonal manganites, where each domain is separated by a mixed domain wall [53, 66]. This intuitive explanation is further supported by the results of a density functional theory (DFT) study [76]. From this study, the researchers found that AP and FE domain walls in hexagonal manganites always consist of two or three mixed domain walls, as illustrated in Figure 2.3.4. The figure shows that the structure always passes through the adjacent domain states from Figure 2.3.3 b) first, resulting in 2-3 atomic-scale domain walls between the domains.

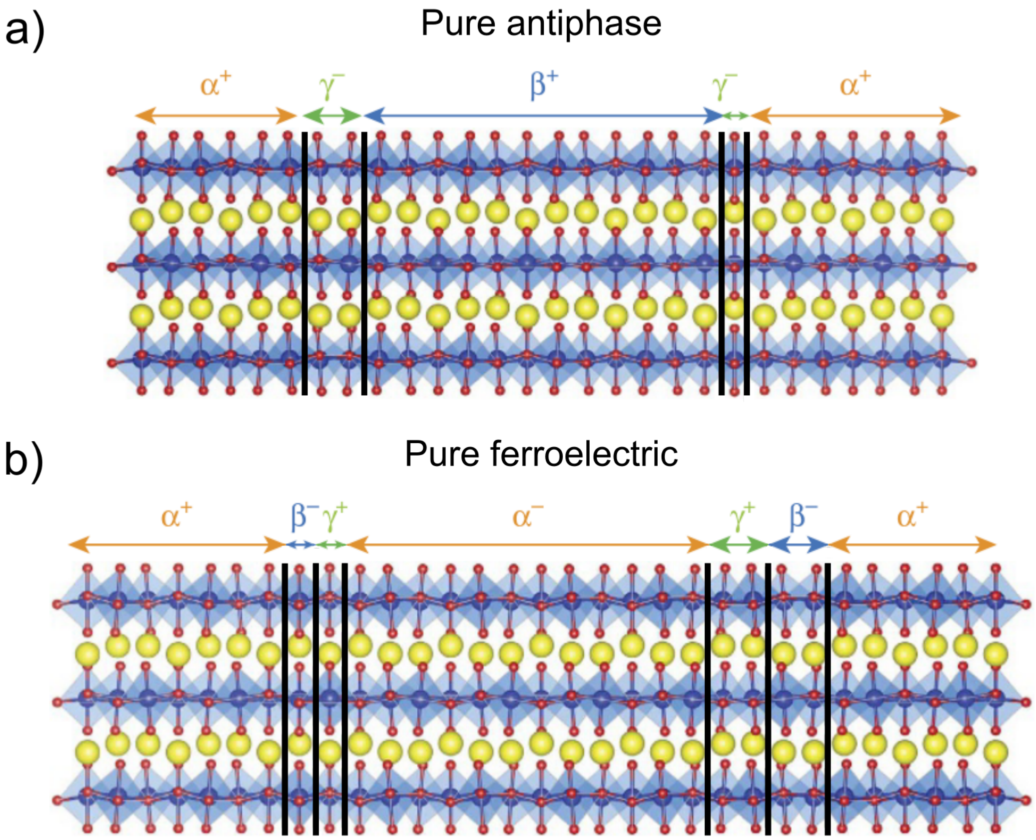

Figure 2.3.4: Domain walls in hexagonal manganites predicted by density functional theory. a) Relaxed AP domain walls. b) Relaxed FE domain walls. The difference in the widths of the intermediate domains is due to the type of domain walls separating them from the original domains and is discussed in more detail in ref. [76]. Adapted from ref. [76].

2.4 Ferroelectric domain structures in hexagonal manganites

There are currently two known topologically distinct domain structures in hexagonal manganites, the vortex domain structure, displayed in Figure 2.4.1 a), and the striped domain structure, displayed in Figure 2.4.1 b) [23, 25, 33, 34, 67, 75]. The vortex domain structure is characterized by its vortex-antivortex pairs at points where the six domain variants, mentioned in section 2.3, come together. It is also the most commonly observed domain structure in as grown $ErMnO_3$ single crystals [24]. The striped domain structure, on the other hand, is characterized by long stripe-like domains [34, 75]. It is also less common but appears, for example, when hexagonal manganites are grown and subsequently annealed below their respective T_C [33]. However, if the sample is heated above T_C and cooled again, the vortex domain structure re-emerges, even though the striped domain structure is very stable when it spans an entire sample [34]. Striped domains can vary greatly in size. Some are the same size as vortex domains, while others can be as narrow as 25 nm across [77]. The lower limit is thought to be around the size of a unit cell because the size of ferroelectric domains in hexagonal manganites can be decreased without vanishing [78]. Because high temperatures can transform the vortex domains into striped domains, it is hypothesized that the vortex domains is a meta-stable state, and that the striped domain structure is the ground state of the hexagonal manganites. This means that, given enough time, the vortex domain structure will eventually evolve into the striped domain structure [33]. However, this has not yet been observed experimentally [34].

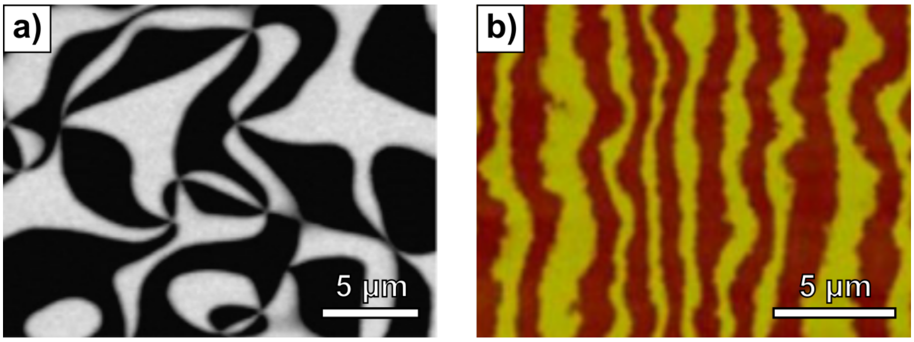

Figure 2.4.1: Illustration of the two ferroelectric domain structures in $ErMnO_3$ reported in literature, a) vortex domain structure and b) striped domain structure. Adapted from ref. [27] and ref. [34], respectively.

The ferroelectric domain structure is not a surface phenomenon but extends throughout the whole $ErMnO_3$ crystal [16]. The domain walls are described as interfaces, with length, width, and depth, while the vortices are 1D strings penetrating the bulk of the crystal [18, 26, 72]. The 3D vortex domain structure is schematically illustrated in Figure 2.4.2 a) with a 1D vortex line indicated by a red dashed line. Because of surface effects, the ferroelectric structure observed at the surface is not representative of the structure in the bulk. For example, it has been observed that surface domains can shrink anisotropically due to self-poling caused by a difference in oxygen content between the surface and the bulk of the ferroelectric. This surface phenomenon favors the negatively polarized domains over the positively polarized domains, such that the negative surface domains grow at the expense of the positive surface domains [79]. The same shrinkage of surface domains is believed to happen when utilizing non-contact electrical poling [16]. Examples of the shrunken domains can be seen in the first panels of Figures 2.4.2 b) and c), where the positive surface domains appear as thin bright lines. Figures 2.4.2 b) and c) also illustrate how the domain structure changes in the bulk and how one vortex line can appear as multiple vortices on the sample surface depending on how the crystal is cut. Striped domains have not been investigated in the literature thus far.

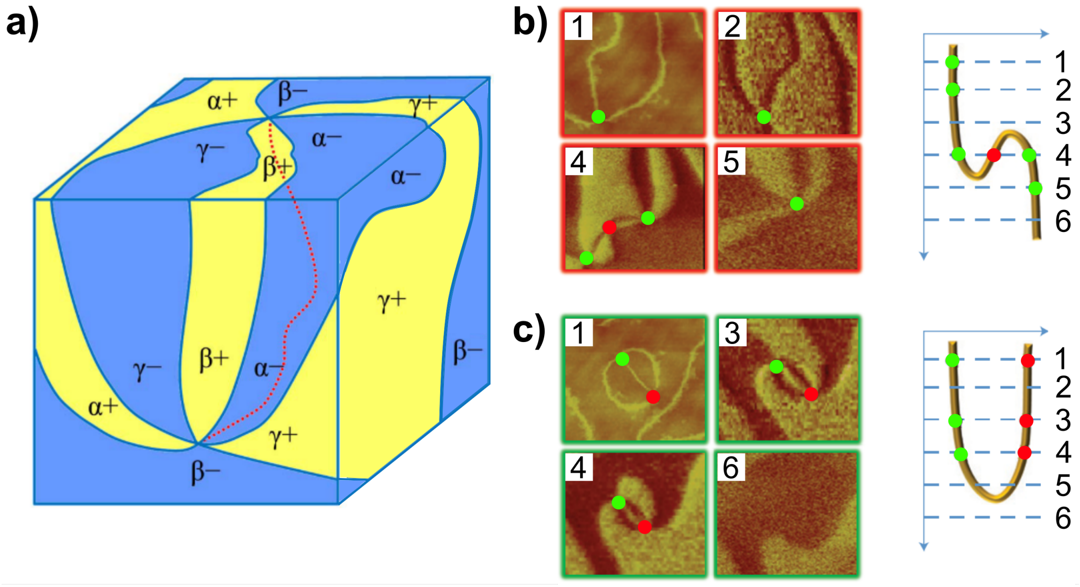

Figure 2.4.2: Illustrations of the 3D structure of ferroelectric domains and vortices. a) Schematic illustration of vortex domain structure in 3D, with a 1D vortex line indicated by the dashed red line connecting the anti-vortex on the front of the cube to the vortex on the top. b) and c) show panels and depth profiles of vortex cores at different depths of a hexagonal $LuMnO_3$ single crystal. Each depth is indicated by a number and is separated by 2 µm. Vortex and anti-vortex cores are labeled as green and red, respectively. Subfigure a) adapted from ref. [18] while b) and c) are adapted from ref. [26].

Vortex cores

There are two kinds of topological defects in the hexagonal manganites: the domain walls and the vortex cores [18]. The domain walls have already been discussed in section 2.2; thus, the focus here will be on the vortex cores. Vortex cores are about 4 unit cells wide and are the meeting points of six domains surrounding the core in one of two possible sequences, $\alpha+$, $\beta-$, $\gamma+$, $\alpha-$, etc., or in reverse $\alpha-$, $\gamma+$, $\beta-$, $\alpha+$, etc. The latter sequence applies to the anti-vortex cores [18]. Through aberration-corrected high-angle annular-dark-field (HAADF) imaging and high-angle annular-dark-field scanning transmission electron microscopy (HAADF-STEM), the inner structure of the vortex cores in $YMnO_3$ and $ErMnO_3$ was probed [15, 18]. The researchers found that the displacement of the R ions was reduced and disordered within the vortices, resulting in the extinction of the polarization [15, 18].

The researchers also found that the vortex cores host interesting electrostatics, making them possible sources for new, unusual electronic transport properties [15]. Furthermore, vortex cores are topologically protected, meaning that they do not change with continuous deformations or perturbations which makes them able to withstand strong electric fields [23, 75, 80]. This immovability is one of the reasons for why complete poling of the ferroelectric structure in hexagonal manganites has failed thus far in previous studies [23]. However, there is evidence of vortices moving under the influence of a very strong electric field close to the edge of an $\mathrm{YMnO_3}$ single crystal. However, the electric field was $500\,\mathrm{kV\,cm^{-1}}$ which is much higher than the coercive field of $75\,\mathrm{kV\,cm^{-1}}$ [79].

As previously stated, the vortex cores are the meeting points of six domains. However, partial edge dislocations (PEDs) can break the symmetry of vortices and make four-state vortices instead of the normal six-state vortices [81]. Examples of six-state and four-state vortices are shown schematically in Figure 2.4.3 a) and b), respectively. The PEDs blur the lines between domains and can allow for two different translational domains to be connected without a separating domain wall by introducing an extra atomic plane in the structure. Thus, two translational domains with the same polarization, such as $\beta-$ and $\alpha-$, can be connected as in Figure 2.4.3 b). This makes it seem like the vortex core is surrounded by only four domains, $\alpha+$, $\gamma-$, $\beta+$ and $(\alpha-/\beta-)$ making a four-state vortex. The opposite can also happen if the PEDs introduce an extra translational domain by splitting a domain in two, as in Figure 2.4.3 c), where the $\gamma+$ domain is split in two by an $\alpha-$ domain. When this occurs, an eight-state vortex is created [81].

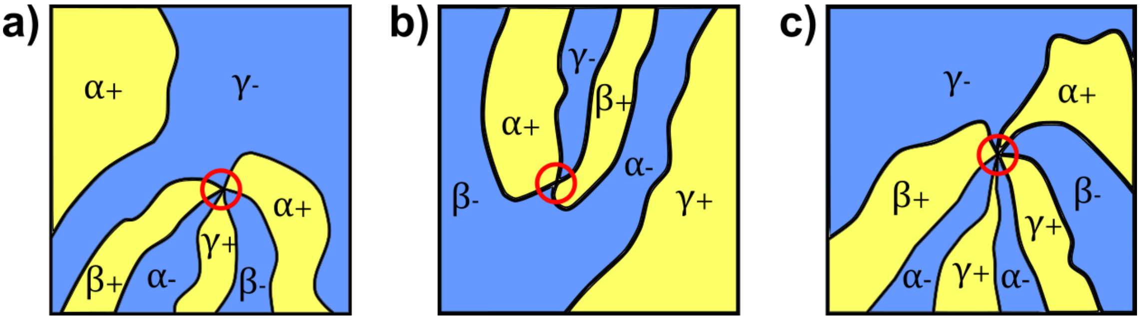

Figure 2.4.3: Schematic diagrams of vortex cores with with domains indexed. a) Normal six-state vortex, b) four-state vortex, and c) eight-state vortex. All vortices are indicated with red circles. Domain indices in a) and b) were determined through HAADF imaging by ref. [81]. Indices in c) are only correct with respect to polarization. Adapted from ref. [81].

Influence of strain on domain structure

The domain structure in hexagonal manganites can be engineered through cooling rate [24, 25, 33], annealing temperature [26, 33], electric fields [23], and elastic strain [34]. The latter was discovered in 2014 when Wang et al. [34] demonstrated vortex core movement in hexagonal manganites by inducing strain in single crystals at 1413 K. In their experiments, they put metal rods on single crystals of $\mathrm{ErMnO_3}$ with different geometries, triangular and rectangular, and cooled them across the transition temperature. Schematics of the experiments are shown in Figures 2.4.4

a) and b). The weight of the rod caused the single crystals to compress on the top surface and stretch at the bottom. In the rectangular crystals, the compression and stretching canceled each other out, as illustrated in Figure 2.4.4 c), and no striped domains were observed. In the triangular crystal, on the other hand, the tip was bent downward, resulting in an average normal strain along the x-axis with a large gradient along the y-axis, as seen in Figure 2.4.4 d). After the thermomechanical treatment, the researchers observed striped domains along the direction of the rod in the triangular sample. They hypothesized that the non-uniform strain induced a Magnus-type force, F_v, that pulled the vortex-antivortex pairs apart, thus morphing the vortex domains into striped domains. The simplified expression for the force acting on the vortices supports this notion. The expression is shown in equation 2.2:

$$F_v = Gh\frac{\pi}{3}\left[2\varepsilon_{xy}, (\varepsilon_{xx} - \varepsilon_{yy})\right] \tag{2.2}$$

where G is the coupling parameter, h is the thickness of the sample, ε_{ii} is the normal strain in the i-direction, and ε_{xy} is the shear strain in the xy-plane. Equation 2.2 has a x-direction and a y-direction part separated by a comma, and shows that the shear strain moves the vortices in the x-direction and that non-uniform normal strain, $\varepsilon_{xx} - \varepsilon_{yy} > 0$, moves the vortices along the y-direction [34]. In their evaluations of the strains and their influence on the vortices, only the in-plane strains were considered because the out-of-plane strains do not couple to the trimerization phase [34].

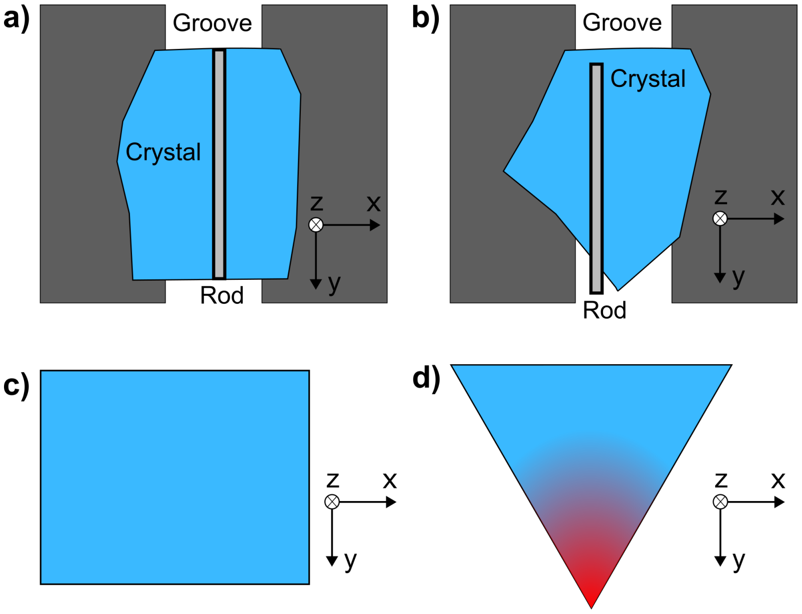

Figure 2.4.4: Schematic illustrations of the two experiments performed by Wang et al. [34] and the average strain distributions in the crystals. a) Bird-view of rectangular crystal with a centered metal rod, b) bird-view of triangular crystal with metal rod off-centered in both x- and y-direction, c) average strain distribution in the rectangular crystal, and d) average strain distribution in the triangular crystal. Redness indicates the magnitude of the strain. Adapted from ref. [34].

Further examination of the influence of strain on the domain structure was done through phase-field simulations, which have long been used to investigate the evolution of ferroelectric and ferromagnetic domain structures [82, 83]. Shi et al. and Xue et al. found that phase-field simulations corroborate the results from Wang et al. [34, 75, 84]. They also found that the magnitude of the strain affects the straightness and density of the striped domains [75, 84]. The simulated effect of increasing strains is illustrated in Figure 2.4.5, where the strain is increased from a) to c). The phase-field simulations also enabled the researchers to inspect the mechanism behind the formation of the striped domains up close. Figure 2.4.6 illustrates that when vortices and anti-vortices move away from each other, they collide with other oppositely topologically charged vortices and annihilate, creating striped domains. The simulations also show that the strains can create new vortex-antivortex pairs, which increases the density of the striped domains [75, 84]. In addition to this, the researchers also hypothesized that the simulated strains were greater than those induced experimentally, because the domain frequencies in the simulations were higher than what was observed by Wang et al. [75]. However, the frequency of the striped domains depends on both the temperature and the non-uniform strain. Increasing the latter results in higher domain frequency and reduces the size of the domains, while increasing the temperature enhances the effect of the non-uniform strain [75].

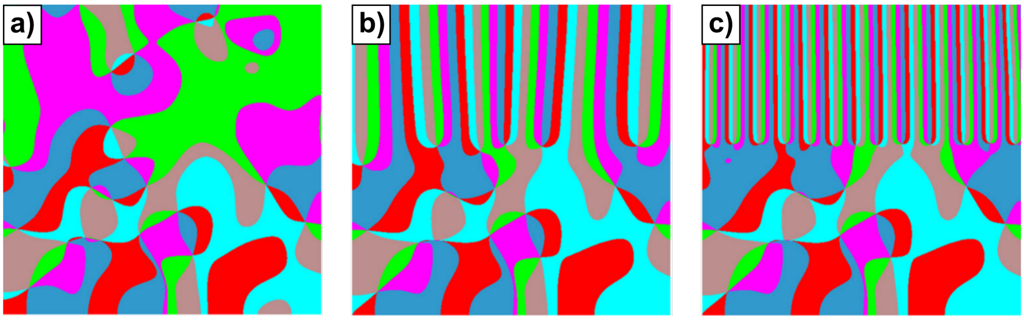

Figure 2.4.5: Simulated equilibrium domain structures at different strains in $YMnO_3$ at 1199 K. a) No strain, b) some strain, ε, in the upper half, and c) 2ε in the upper half. Adapted from ref. [75].

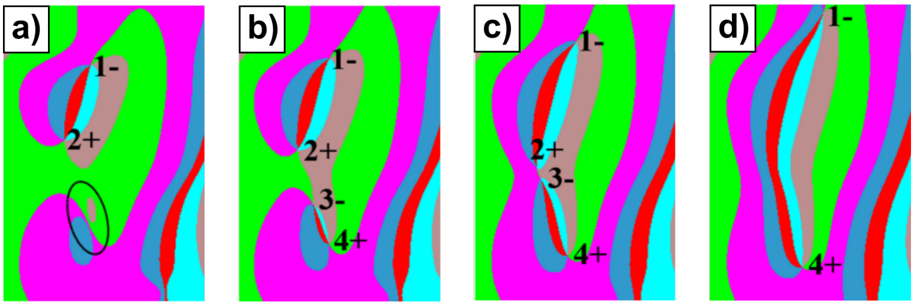

Figure 2.4.6: Simulated temporal evolution of striped domains through creation and annihilation of vortices in $YMnO_3$ at 1199 K. a) and b) show the creation of a new vortex-antivortex pair close to bubble-like domains, while c) and d) show movement, collision and annihilation of the vortices 2+ and 3−, and the formation of striped domains. Adapted from ref. [75].

2.5 Scanning probe microscopy

Scanning probe microscopy (SPM) is a technique in which a sharp tip is used to raster-scan samples and collect information about their surface [85]. The technique dates back to the early 1980s when Binning et al. successfully imaged the topography of gold with atomic resolution using scanning tunneling microscopy (STM), which relies on the tunneling of electrons [85, 86]. A few years later, in 1985, another SPM technique was invented. Very similar to STM, but using the local atomic and molecular forces, atomic force microscopy (AFM) proved to be one of the most important SPM techniques [87, 88]. One major advantage of AFM is its ability to scan almost any surface, unlike STM, which only works for conducting and semiconducting surfaces [88]. Several adaptations have been made from these two early techniques, and there now exists a wide range of SPM techniques. Examples of newer SPM techniques include: time-resolved STM, magnetic-field-sensitive SPM, electric field-sensitive SPM, liquid-phase SPM, electrical transport-compatible SPM and near-field SPM [88]. In this thesis, a form of electrical field-sensitive SPM, called PFM, has been utilized and will be discussed in more detail in the following subsection.

2.5.1 Piezoresponse force microscopy

PFM was first utilized by Güthner and Dransfield in 1992, when they locally poled and subsequently imaged ferroelectric domains in a ferroelectric polymer film using the tip of a SPM [89]. Since then, the technique has become the standard tool for imaging ferroelectric domains [5]. PFM measures the piezoelectric response of ferroelectric domains on the nanoscale, and can distinguish between domains based on this response. During a PFM scan, a conductive tip is held in contact with the sample surface while an oscillating voltage is applied to the tip. The local electric field, created by the voltage, induces a piezomechanical response from the material, causing it to deform slightly and the tip to move with the deformation. This movement is then measured by a laser reflecting off a mirror on the cantilever of the tip before hitting a photodetector, as illustrated in Figure 2.5.1 a). Finally, the signal is extracted from the photodetector by a lock-in amplifier (LIA) [5].

In- and out-of-plane response
The piezomechanical response of a ferroelectric material depends on the orientation of the polarization directly underneath the probe tip [5]. If the polarization is out-of-plane, the deformation of the material is also out-of-plane, and the tip is moved up and down, causing deflection of the cantilever as illustrated in Figure 2.5.1 b). If the polarization is in-plane, the deformation causes buckling or torsion of the cantilever, which is also illustrated in Figure 2.5.1 b). The different movements of the cantilever move the laser in certain directions on the photodetector as illustrated in Figure 2.5.1 c). Deflection and buckling result in a vertical signal, while torsion gives a lateral signal [5].

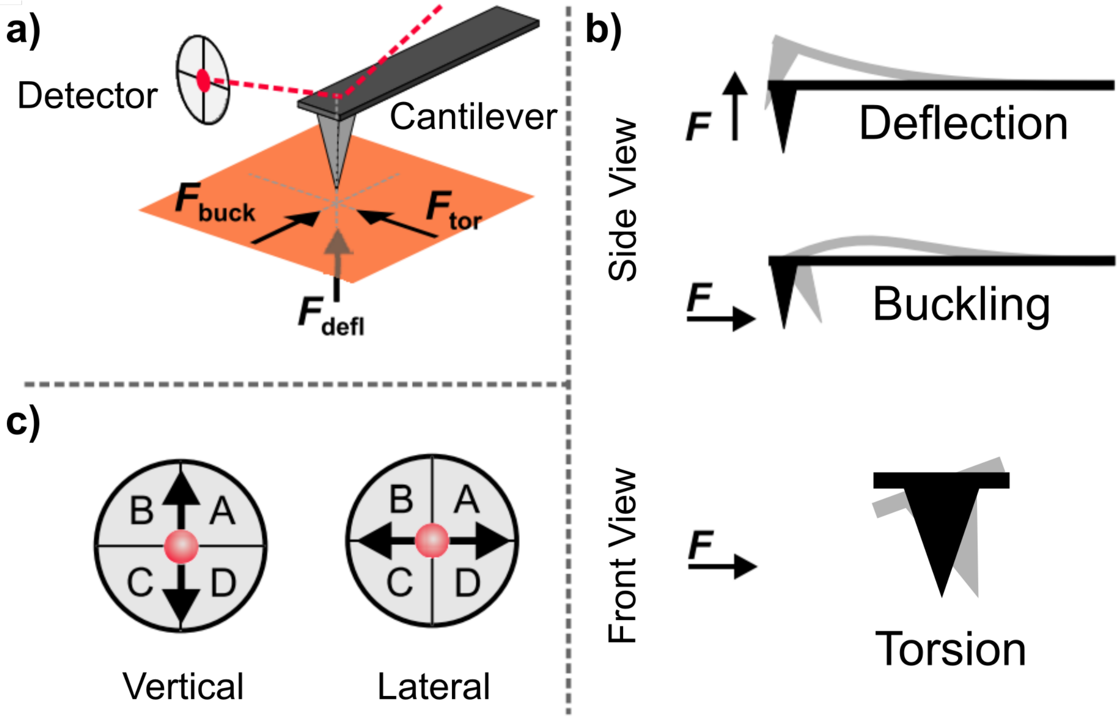

Figure 2.5.1: Schematic illustration of the forces acting on the PFM tip and their effect on the cantilever and the PFM signal. a) PFM setup with forces indicated, b) forces and the associated movement of the cantilever, and c) the possible movements of the laser on the photodetector. Adapted from refs. [5, 90].

Because buckling and deflection both give a vertical signal, in- and out-of-plane polarization is not easily distinguished. To describe the local deformation of the sample more accurately, the in- and out-of-plane deformation must be separated through a technique known as vector PFM. The technique works by scanning the area of interest three times with different rotations, 0°, 90°, and 180°. The 90° rotation allows for the separation of the in-plane deformations, while the 180° rotation enables the separation of buckling from deflection [5]. However, all scanning force microscope systems have a small degree of inherent crosstalk due to, for instance, a slight misalignment of the readout laser plane and the detector [5]. This means that, even when using vector PFM, it is challenging to accurately determine the orientation of the polarization.

Resolution

With PFM, ferroelectric domain patterns with a sub 10 nm lateral resolution can be obtained depending on the tip radius, and the elasticity and dielectric properties of the sample [5, 90, 91]. The tip's lateral resolution, W, can be determined by moving it across a 180° domain boundary. When the tip approaches the domain wall, the PFM signal becomes weaker as the volume fractions of the two measured domains become more equal and cancel each other out. After the measurement, the lateral resolution can be defined as the full width at half maximum (FWHM) of the PFM signal across the boundary. Soergel et al. found that the relation between tip radius, r, and lateral resolution was: $W \approx 1.2 \cdot r$ for tips with conductive coatings, and: $W \approx 3.3 \cdot r$ for un-coated n-doped silicon tips [5].

As described in section 2.4, the ferroelectric domain structure on the surface can be different from the one in the bulk. Therefore, it is important to keep in mind how deep the PFM is probing into the sample. For instance, if the surface domain is relatively shallow, the PFM signal can be influenced by domains lying underneath the surface domain [92]. Johann et al. reported a depth resolution of 1.7 µm when using a diamond coated tip with a nominal radius of 50−70 nm and 5 V. They also found that using a larger tip radius increases the depth resolution, while increasing the amplitude of the voltage does not [92].

Phase and amplitude

The LIA extracts and rectifies the periodic signal of the deformation from the noisy environment [5]. The results of the LIA measurement can be represented as either a phase, Θ, and a magnitude, M, or as two amplitudes, X and Y. The phase is the difference in phase between the measured signal and a reference signal, while the magnitude is the strength of the signal. The two representations are related like polar and Cartesian coordinates through: $X = M \cdot \sin\Theta$ and $Y = M \cdot \cos\Theta$. By using Θ and M, two PFM images can be constructed. However, by using X or Y, all the information can be contained in one image, which is why X or Y is usually referred to as the piezoresponse. Figure 2.5.2 shows the different values for Θ, M, and X corresponding to different polarization orientations.

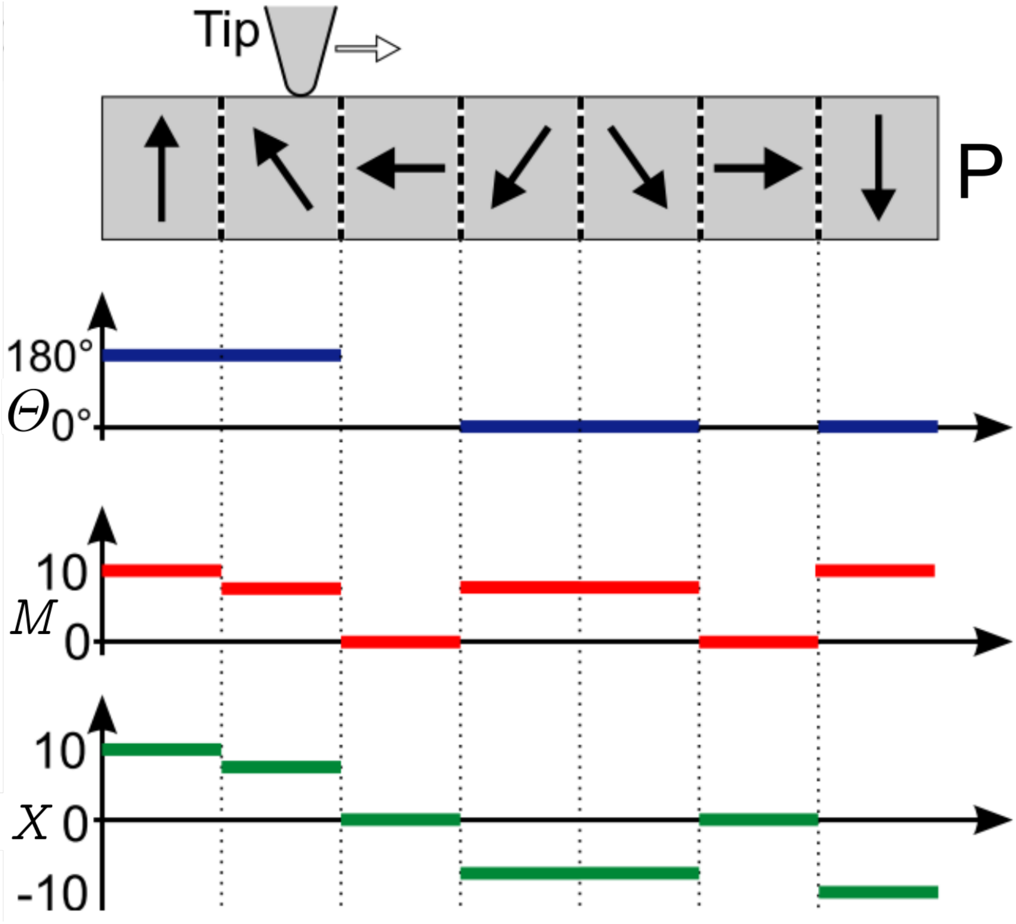

Figure 2.5.2: Schematic illustration of polarization orientations and associated phases, Θ, magnitudes, M, and amplitudes, X, in the vertical channel. Adapted from ref. [5].

Other AFM techniques

Resonance PFM is a technique where the alternating voltage resonance frequency is set approximately equal to the contact resonance, f_{cont}, of the cantilever, which is the cantilever's resonance frequency when the tip is in contact with the sample [5]. The contact resonance frequency depends on the stiffness of the sample and the resonance frequency, f_{free}, of the cantilever, which in turn depends on its stiffness. As an approximation one can say that $f_{cont} \approx 4 \cdot f_{free}$ [5, 93]. Resonance PFM improves the signal-to-noise ratio by utilizing resonance enhancement but also includes topographic information in the acquired signal [5, 94].

Another variant of PFM is SS-PFM [95]. SS-PFM works by measuring the piezoelectric response in a single point with voltage pulses that are increased and decreased stepwise, as illustrated in Figure 2.5.3. Then the same procedure is repeated for the rest of the area of interest until the voltage-dependent piezoelectric response in each point has been mapped. SS-PFM allows the user to connect work-of-switching, electromechanical activity, coercive bias, and imprint to distinct locations on the sample. This gives insight into how local structures, topographic or ferroelectric, affect the polarization switching; see the hysteresis loop in Figure 2.2.4 [90, 95].

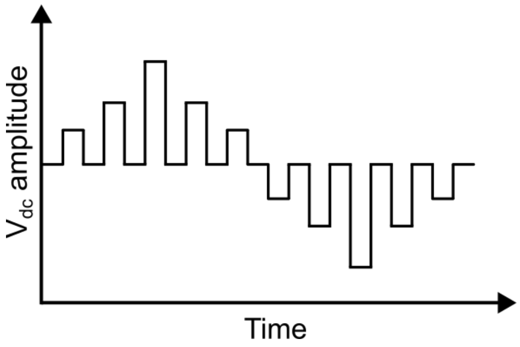

Figure 2.5.3: Schematic illustration of the voltage pulses applied during SS-PFM. Adapted from ref. [95].

Influence of electrostatic effects

Electrostatic effects are present in all the aforementioned techniques and can affect their results [5]. Coulomb forces between the tip and the sample surface arise because ferroelectric domains have surface charges, and the PFM tip is periodically charged. However, this force does not necessarily move the tip. For the tip to move, either the surface or tip must deform, or the tip-sample potential must change. The former is unlikely, as demonstrated by previous experiments, where researchers found that the deformation impact was insignificant. The researchers also found that the interaction between the charged tip and the polarization-induced surface charges can be neglected when using a stiff cantilever with a spring constant greater than $2\,\mathrm{N\,m^{-1}}$ [5, 96]. Coulomb forces can also act directly on the cantilever and bend it, but since the cantilever is quite big compared to the size of the imaged domains, the effect of the interaction on the PFM measurement is small [5, 97]. The instrument used also contributes to the electrostatic interactions. It has been found that there is a linear relationship between the applied dc voltage and the PFM signal. The cause of this contribution is imperfect electrical shielding [5].

Chapter 3

Experimental

3.1 Thermomechanical treatment of $ErMnO_3$

High-quality $ErMnO_3$ powder was synthesized through a solid-state reaction between Er_2O_3 (99.9% purity, Alfa Aesar, Haverhill, MA, USA) and Mn_2O_3 (99.0% purity, Sigma-Aldrich, St-Louis, MO, USA). The calcination was done stepwise at 1000 °C, 1050 °C, and 1100 °C for 12 hours. Then the powder was sintered at 1400 °C for four hours into cylinders with a diameter and height of 7.60 mm and 5.13 mm, respectively. More information about the processing of the samples can be found in ref. [8].

To investigate the impact of mechanical pressure applied during the ferroic phase transition on the domain structure of $ErMnO_3$, the cylinders were annealed under three different mechanical loads. For the annealing process, the samples were put into an Al_2O_3 die filled with coarse MgO powder to prevent the samples from reacting with the die. Then the samples were heated to an annealing temperature of 1220 °C at a rate of 5 $°C\,min^{-1}$. The annealing temperature was set above the Curie temperature of $ErMnO_3$, $T_C \approx 1156\,°C$, to reset the ferroelectric domain structure [24, 56]. A 30-minute dwell time was used to ensure that the samples, the MgO powder, and the pressing die were in thermal equilibrium. Then a uniaxial pressure of 0 MPa, 24 MPa or 47 MPa was applied to the samples while maintaining a temperature of 1220 °C for 10 more minutes as illustrated in Figure 3.1.1. Afterward, the samples were cooled with the applied pressure until room temperature was reached. A constant cooling rate of 5 $°C\,min^{-1}$ was used to prevent unwanted cooling-rate-dependent variations in the domain structure, as demonstrated in refs. [24, 33]. The temperature and pressure profiles for the annealing process are shown in Figure 3.1.2.

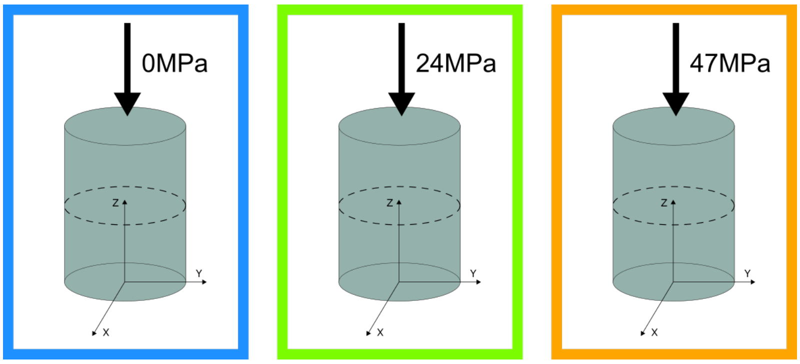

Figure 3.1.1: Schematic illustration of the samples under different pressures during annealing. The color coding of the frames emphasizes the pressure used on the samples, and is used throughout the thesis.

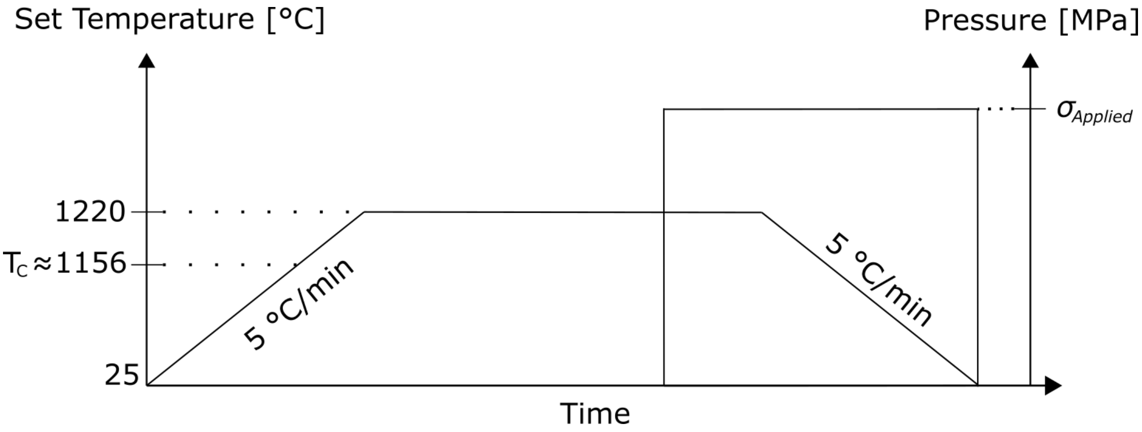

Figure 3.1.2: Temperature and pressure profiles of the thermomechanical treatment of the polycrystalline $ErMnO_3$ cylinders. First the temperature was increased to 1220 °C at a rate of 5 °C/min, and kept at this temperature for 30 minutes. Then a uniaxial pressure, $\sigma_{Applied}$, of either 0 MPa, 24 MPa or 47 MPa was applied to the cylinders for 10 minutes, followed by cooling to room temperature at a rate of 5 °C/min while still under pressure. T_C of $ErMnO_3$ is indicated as well [24, 56].

After annealing, the samples were cut, as shown in Figure 3.1.3, into half-discs using a diamond wire saw (SERIE 3000, Well, Germany). To gain insight into the micro- and nanostructure parallel and perpendicular to the applied mechanical pressure, 2 mm thick in-plane and out-of-plane samples were prepared. To characterize the microstructure, the samples were lapped with a 9 µm-grained Al_2O_3 water suspension (Logitech, Ltd, Glasgow, UK) and polished using a silica slurry (Ultra-Sol®2EX, Eminess Technologies, Scottsdale, AZ, USA) to produce a surface roughness with a root mean square (RMS) value of around 70 nm.

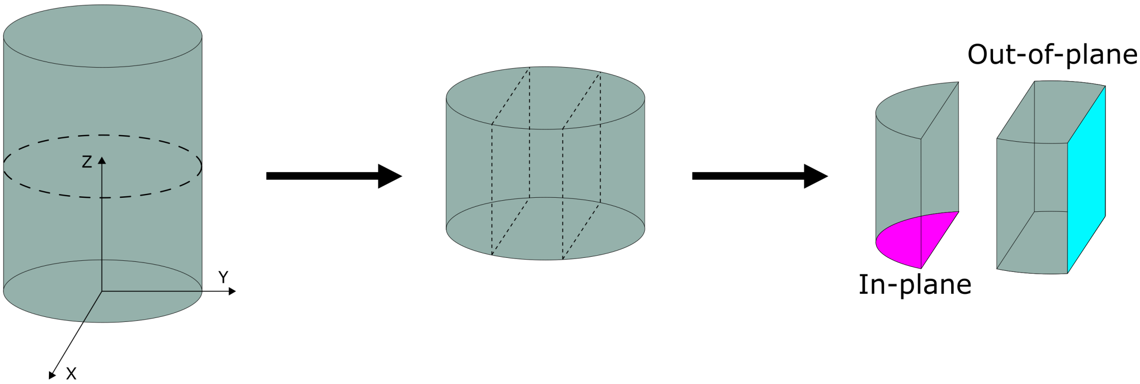

Figure 3.1.3: Schematic illustration of the sample preparation after the thermomechanical treatment. Dashed lines indicate the cuts made. Colored faces indicate in- and out-of-plane sample faces. The pressure was applied in the z-direction during annealing.

3.2 X-ray diffraction

To determine the crystal structure and phase purity of the samples, X-ray diffraction (XRD) was performed. A D8 Advance DaVinci with LynxEye super-speed detector and Cu K-alpha x-ray source (Bruker, Billerica, MA, USA) was used with a scan range of 10° to 75° 2θ.

3.3 Scanning electron microscopy

Micrographs of the polished samples were acquired by performing SEM with a Helios G4 UX (FEI, Lausanne, Switzerland). Parameters used for imaging are displayed in Table 3.3.1.

Table 3.3.1: Settings used for the acquisition of the SEM micrographs.

Setting	Value
Acceleration voltage	1.00 kV
Beam current	0.20 nA
Working distance	3.7-4.2 mm
Detectors	ICE, SE and TLD

3.4 Scanning probe microscopy

To map the domain structure of the samples, PFM measurements were performed. The initial images were taken using an NT-MDT Ntegra Prisma system (NT-MDT, Moscow, Russia) with an electrically conductive tip. An overview of tips used is provided in Table 3.4.1. During the measurements, the samples were excited using an alternating voltage with a frequency of 40.13 kHz, and an amplitude of 10 V applied to the bottom electrode. At the same time, the laser deflection was read out by two LIAs (SR830, Stanford Research Systems, Sunnyvale, CA, USA) to obtain the in- and out-of-plane piezoresponse. Prior to the measurements on the polycrystalline $ErMnO_3$, the PFM response was calibrated on a periodically out-of-plane poled $LiNbO_3$ sample (PFM03, NT-MDT, Moscow, Russia).

Table 3.4.1: Tips used for AFM measurements on $ErMnO_3$ samples.

Tip name and company	Tip radius	Cantilever stiffness
Spark 150 Pt (NuNano, Bristol, UK)	< 30 nm	$18\,\mathrm{N\,m^{-1}}$
ASYELEC-01-R2 (Asylum Research, Santa Barbara, CA, USA)	25 ± 10 nm	$2.8\,\mathrm{N\,m^{-1}}$
DEP01 (TipsNano, Tallinn, Estland)	<10 nm	$1.2\text{-}4.5\,\mathrm{N\,m^{-1}}$
DDESP10 (Bruker, Billerica, MA, USA)	100 nm	$80\,\mathrm{N\,m^{-1}}$
Multi75E-G (BudgetSensors, Sofia, Bulgaria)	25 nm	$1\text{-}7\,\mathrm{N\,m^{-1}}$

To further investigate some exciting domain features, a Cypher S AFM (Asylum Research, Santa Barbara, CA, USA) with an isolated environment and electrical shielding was used to perform resonance PFM and acquire high-resolution images. For the resonance PFM, the DEP01 tip was used with a lateral frequency of 7.1775×10^5 Hz, normal frequency of 3.0×10^5 Hz, lateral tip voltage of 3 V, and a normal tip voltage of 1 V.

In addition, SS-PFM was performed at Oak Ridge using a Cypher S AFM (Asylum Research, Santa Barbara, CA, USA) with a Multi75E-G tip. The measurement covered a grid of (128×128) points spread over an area of $(15.1 \times 15.1)\ \mu\mathrm{m}^2$. In each point, voltage pulses from 0 V to 15 V to -15 V were applied stepwise as illustrated in Figure 2.5.3. This was done twice. The sample investigated was synthesized similarly to the other samples but without the thermomechanical treatment and is called the Oak Ridge sample (OR-sample).

3.5 Electron backscatter diffraction

To map the orientation of the grains in the out-of-plane 47 MPa sample, EBSD was performed using an Ultra 55 FEG-SEM (Zeiss, Jena, Germany). The scan was performed with an acceleration voltage of 10 kV, a working distance of 20.4 mm and a sample rotation of 70°. Prior to the scan, the sample was carbon coated to enhance conductivity. A nominal area of $(235 \times 235)\ \mu\mathrm{m}^2$ was scanned, and Kikuchi diffraction patterns of (120×120) pixels were recorded with a nominal step size of 0.5 µm. The diffraction patterns were indexed utilizing the dictionary indexing method in

EMsoft (version 5) [98]. Then, orientations were sampled from the Rodrigues Fundamental Zone using Cubochoric sampling [99], and diffraction patterns for $ErMnO_3$ with the space group $P6_3cm$ were simulated [62]. Then, EMsoft was used to optimize the match between the simulated and recorded patterns. The quality of the match between the simulated and raw Kikuchi patterns is demonstrated in Figure 3.5.1. Finally, the orientation analysis was performed in Matlab [100] with MTEX (version 5.8) [101].

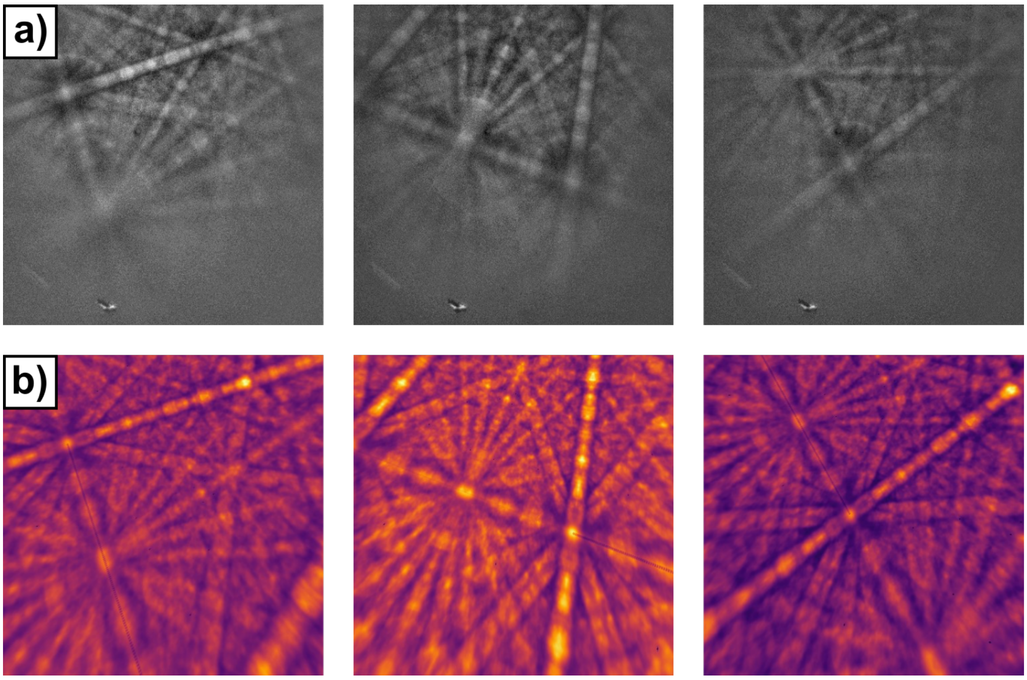

Figure 3.5.1: Examples of Kikutchi patterns for $ErMnO_3$. a) Raw Kikutchi patterns from EBSD scan, and b) simulated best matching patterns after refinement.

Chapter 4

Impact of mechanical pressure

4.1 Crystallographic analysis

X-ray diffractograms of the $ErMnO_3$ samples annealed under different mechanical pressures are presented in Figure 4.1.1. The X-ray diffractograms confirm the $P6_3cm$ space group, see Figure 2.3.1 b), as observed in $ErMnO_3$ single crystals [27] and shown in the inset of the figure. The XRD data indicates the absence of any secondary phases for the samples independent of applied mechanical pressure.

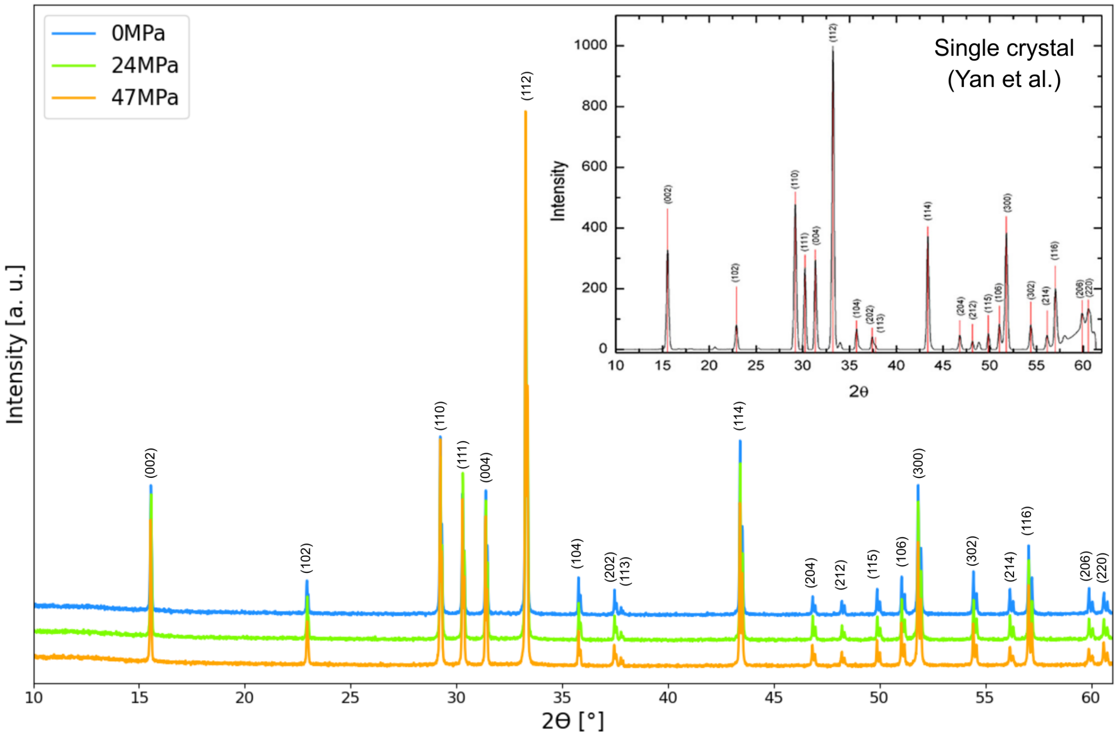

Figure 4.1.1: X-ray diffractogram of the $ErMnO_3$ samples annealed at different mechanical pressures with characteristic (hkl) peaks marked. The intensities have been shifted laterally to make the comparison easier. Inset is the crystallographic data for a $ErMnO_3$ single crystal from ref. [27] for comparison.

4.2 Microstructural analysis

SEM micrographs of the samples annealed under different pressures are shown in Figure 4.2.1. Overview images used to analyze the grain size are presented in the left column, while magnified images are presented in the right column. The microstructure features grains, grain boundaries, pores, and a mixture of inter- and intragranular microcracks. The microcracks likely originate from large thermal stresses induced during cooling, as discussed previously for polycrystalline $YMnO_3$ [102, 103]. In addition, ferroelectric domains and domain walls can be observed in the SEM images depending on the imaging conditions. The domain contrast originates from differences in electron emission yield, as explained elsewhere [16]. The magnified images indicate that the domain structure is affected by the applied pressure. By averaging over approximately 60 grains (20 for each pressure), their average size is determined to be 12.8±1.7 µm. This indicates that the grain size is independent of the applied mechanical pressure, which in turn indicates the absence of creep [104]. Thus, the changes in domain structure can be attributed solely to the applied pressure and not to a change in grain size as previously reported [8]. The impact of mechanical pressure on the domain structure is investigated further in the following section.

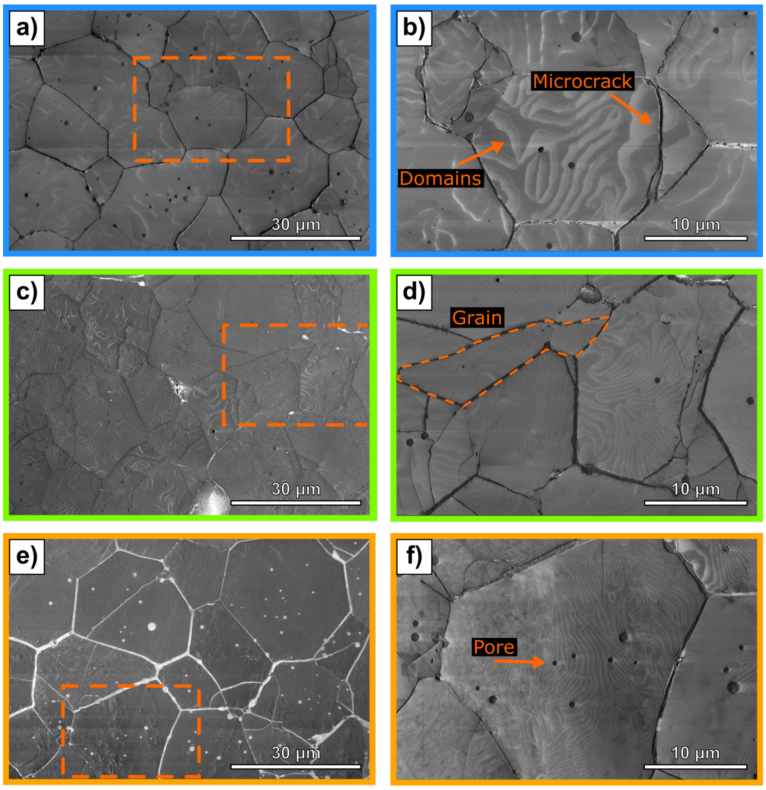

Figure 4.2.1: SEM micrographs of the in-plane samples annealed under different pressures: a), b) 0 MPa, c), d) 24 MPa, and e), f) 47 MPa. Domains, microcracks, and pores are indicated by arrows, while a grain boundary is indicated by a dashed line. The left column shows overview micrographs used for the grain size analysis with dashed squares indicating the position of the magnified images. The difference in contrast between the images is due to different imaging parameters. The right column shows the microstructure of the grains in more detail.

4.3 Nanoscale electromechanical analysis

4.3.1 Ferroelectric domain structures

To investigate the ferroelectric domain structure in more detail, PFM was performed. Lateral PFM images of the in-plane and out-of-plane samples are displayed in Figures 4.3.1 and 4.3.2, respectively. It is observed that the samples display the well-established ferroelectric domain structure of $ErMnO_3$, which consists of ferroelectric 180° domain walls coming together in characteristic six-fold meeting points known as vortices and anti-vortices [13, 23, 34, 67]. From this, it can be inferred that the domain structure consists of the well-known six translational domains, $\alpha\pm$, $\beta\pm$, and $\gamma\pm$, that originate from the trimerization discussed previously in section 2.3. Besides the isotropic domains visible in Figure 4.3.1 a), striped domains are also observed in Figure 4.3.1 b) and c). The domain contrast observed in the different grains varies depending on the orientation of the grains in the polycrystal, as explained in section 2.5.1. Complementary PFM images showing the vertical PFM contrast are presented in Appendix A, and some other interesting PFM images are shown in Appendix B.

From the PFM images of both the in-plane and out-of-plane samples in Figures 4.3.1 and 4.3.2, a clear correlation between the applied mechanical pressure and the size and frequency of the ferroelectric domains is observed. The 0 MPa sample, Figures 4.3.1 a) and 4.3.2 a), is characterized by large isotropic vortex domains with no preferred orientation within each grain, while the 47 MPa sample, Figures 4.3.1 c) and 4.3.2 c), is dominated by narrow striped domains that mostly align within each grain. The 24 MPa sample, Figures 4.3.1 b) and 4.3.2 b), shows an intermediate domain structure with some striped domains and some vortex domains. The striped domains observed are similar to those reported for single crystals under elastic strains, where the applied mechanical pressure transformed the vortex domain structure into the striped domain structure [34]. The formation of the striped domains is thought to originate from the movement of vortices, and anti-vortices in opposite directions under the influence of strain fields [8, 75, 84].

In addition to the vortex and striped domains previously reported in the literature, a thus far unreported domain structure is observed in the 47 MPa sample. This new domain structure resembles ripped fabric and is hypothesized to be induced by strain. Because of this, it has been named "ripped" domains. The ripped domains are only observed in the 47 MPa samples indicating that high strains are necessary for their formation. The three different domain structures, vortex domains, striped domains, and ripped domains, are compared in Figure 4.3.3. The figure illustrates the fundamental differences between the domain structures. The vortex domains displayed in Figure 4.3.3 a) have meandering domains that are all connected directly or indirectly by vortices. The striped domains, seen in Figure 4.3.3 b), are all oriented more or less in the same direction and are usually not connected. The ripped domains, shown in Figure 4.3.3 c), appear to be elongated in a general direction but do not form continuous stripes. In fact, the ripped domains do not appear to have any clear sub-unit domains like the vortex and striped domains have. Instead, the ripped domains are connected randomly and without vortices.

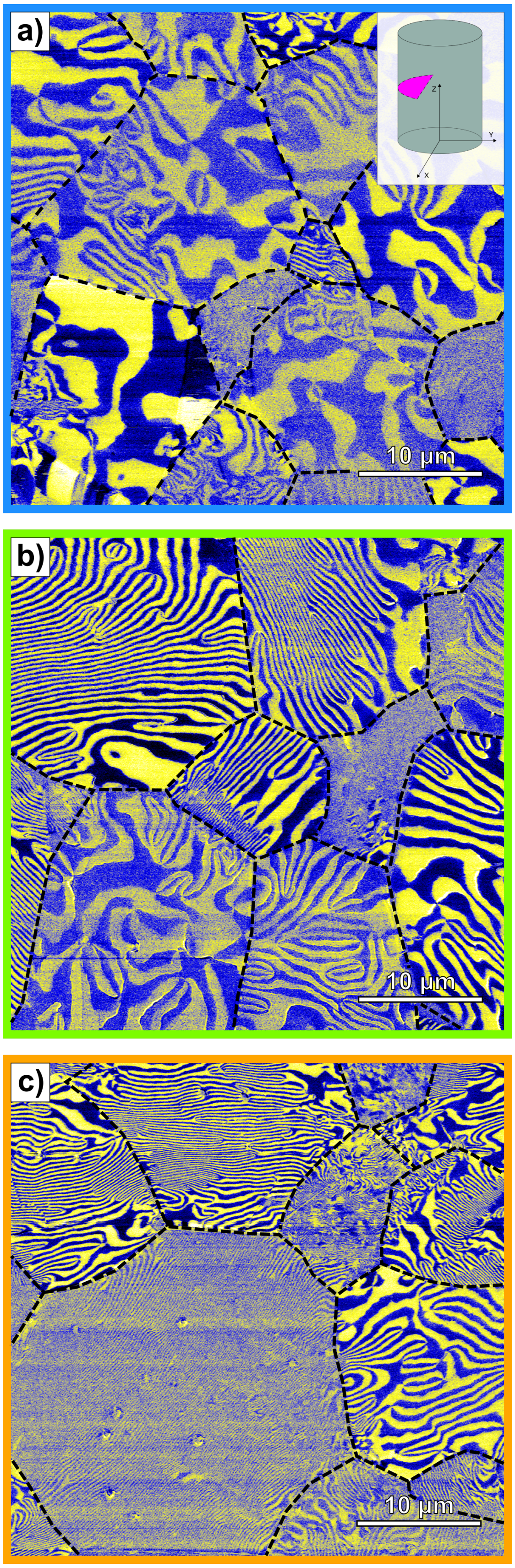

Figure 4.3.1: Lateral PFM images of the in-plane samples annealed under different pressures: a) 0 MPa, b) 24 MPa, and c) 47 MPa. The images show the lateral piezoresponse of the xy-plane indicated in the inset of a). Grain boundaries are indicated with dashed lines.

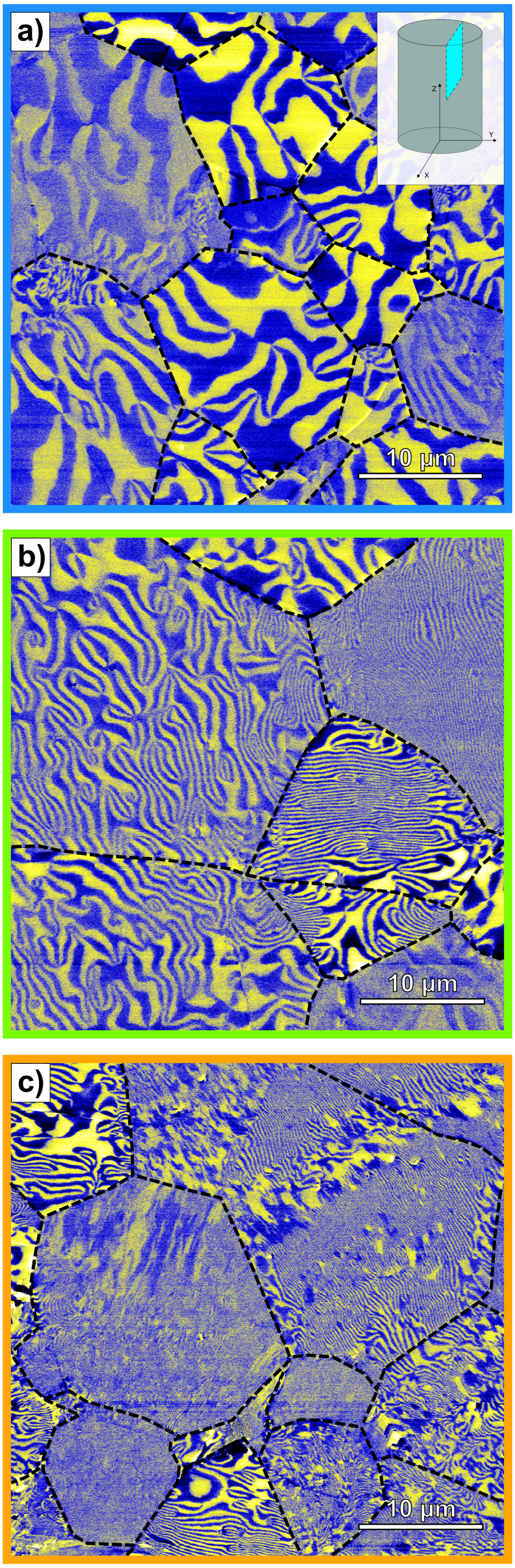

Figure 4.3.2: Lateral PFM images of the out-of-plane samples annealed under different pressures: a) 0 MPa, b) 24 MPa, and c) 47 MPa. The images show the lateral piezoresponse of the xz-plane indicated in the inset of a). Grain boundaries are indicated with dashed lines.

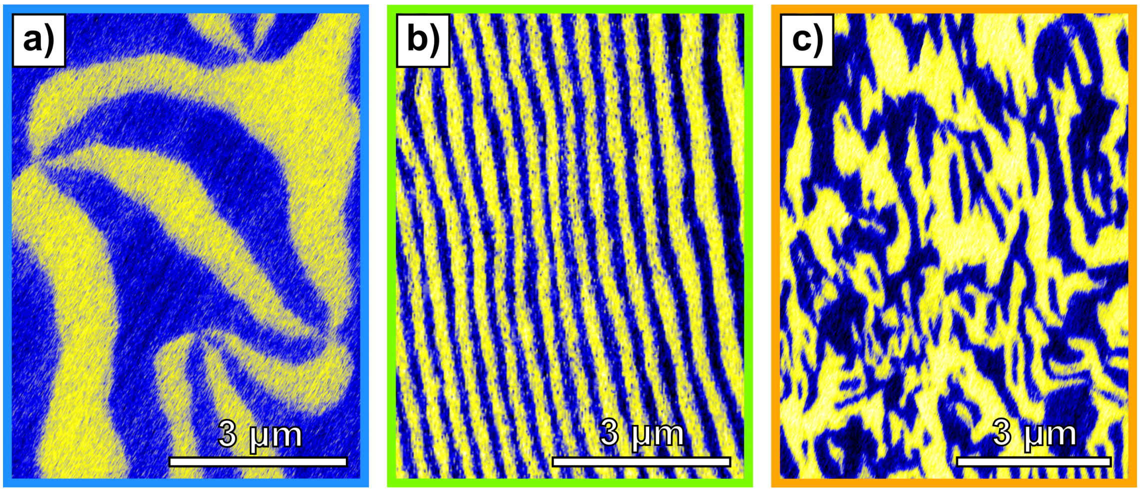

Figure 4.3.3: Comparison of observed domains structures: a) vortex domains, b) striped domains, and c) ripped domains.

4.3.2 Domain frequency and vortex density

As seen in Figures 4.3.1 and 4.3.2, the domains tend to decrease in size with increased applied mechanical pressure. To quantify this trend, the average domain frequency of each sample was calculated by averaging the domain frequency of each grain in that sample. The domain frequency of each grain was calculated by drawing a line across the grain and counting the number of domains intersected. The line was drawn in such a way as to best reflect the domain frequency in the grain, and around 20 grains were inspected for each sample. The average frequency of the ferroelectric domains was 0.55 μm^{-1} in the 0 MPa sample, 1.22 μm^{-1} in the 24 MPa sample, and 2.42 μm^{-1} in the 47 MPa sample. The highest frequency observed was in the 47 MPa sample and was 15.87 μm^{-1}. Representative images of the frequencies are shown in Figure 4.3.4 to illustrate the difference and give a visual representation of the different domain frequencies.

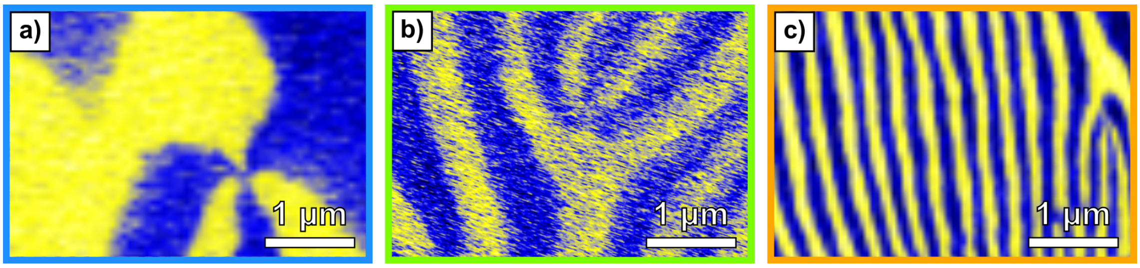

Figure 4.3.4: PFM images showing representative domain frequencies from the different samples. a) shows a frequency of 0.75 μm^{-1} in the 0 MPa sample, b) a frequency of 1.25 μm^{-1} in the 24 MPa sample, and c) a frequency of 3.75 μm^{-1} in the 47 MPa sample.

To further investigate the trend, the average frequency of the ferroelectric domains is plotted as a function of the applied mechanical pressure, and compared with the available literature value of single-crystalline materials with the same cooling rate. The plot in Figure 4.3.5 shows that the average domain frequency increases by 440% from 0 MPa to 47 MPa applied pressure. In addition, the plot demonstrates that the average domain frequency of the 0 MPa sample is similar to the single crystal value from literature, which only differs by 0.15 μm^{-1}. Furthermore, the plot shows little variation between the in- and out-of-plane samples compared to the difference between applied pressures. The plot also shows that the standard deviation, indicated by the error bars, increases with the applied pressure. This increase is connected to the anisotropy in domain structures primarily observed in the 24 MPa and 47 MPa samples, as seen in Figures 4.3.1 and 4.3.2. That is, the difference between the domains of different grains is greater in the 47 MPa sample than in the 0 MPa sample. In the 47 MPa sample, it is observed that some grains have very narrow striped domains, while some have larger vortex domains, in contrast to the 0 MPa sample, which mainly hosts vortex domains of approximately the same size.

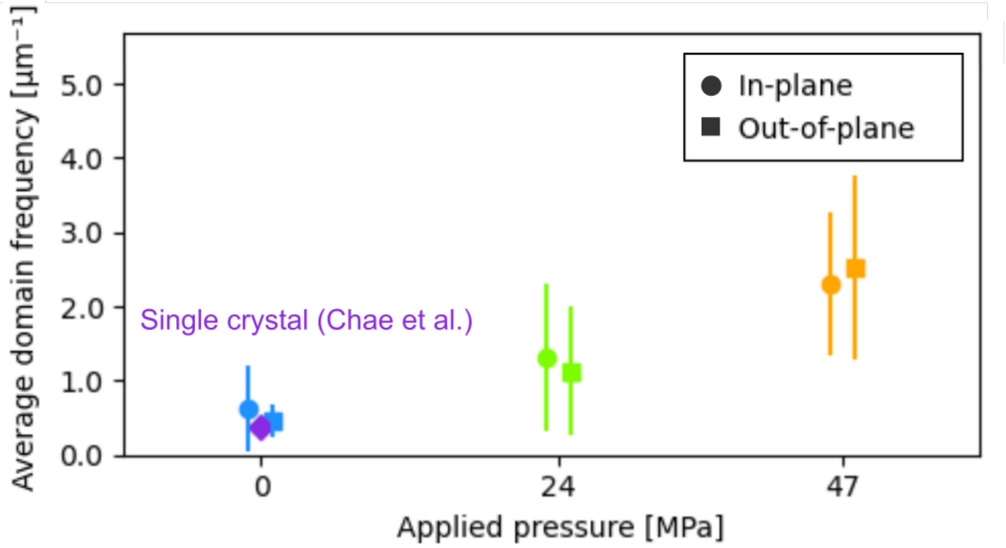

Figure 4.3.5: Average domain frequencies for the polycrystalline $ErMnO_3$ samples cooled under different pressures at a rate of 5 °C min^{-1}, compared to a single crystal cooled at the same cooling rate. Single crystal value from ref. [33].

In order to investigate the effect of the mechanical pressure on the vortex density of the $ErMnO_3$ samples, the vortices in each grain were counted manually, and the average vortex density for each sample was calculated. The plot of the vortex density as a function of pressure is displayed in Figure 4.3.6. The plot shows that the average vortex density for all the polycrystalline samples is 6-10 times lower than that of the single crystals from the literature. Furthermore, the plot shows a negligible change in vortex density with pressure. In addition, similarly to the frequency plot in Figure 4.3.5, the standard deviation of the vortex density increases with pressure due to an increase in domain anisotropy. The plot also shows a significant difference in the vortex density of the two single crystals.

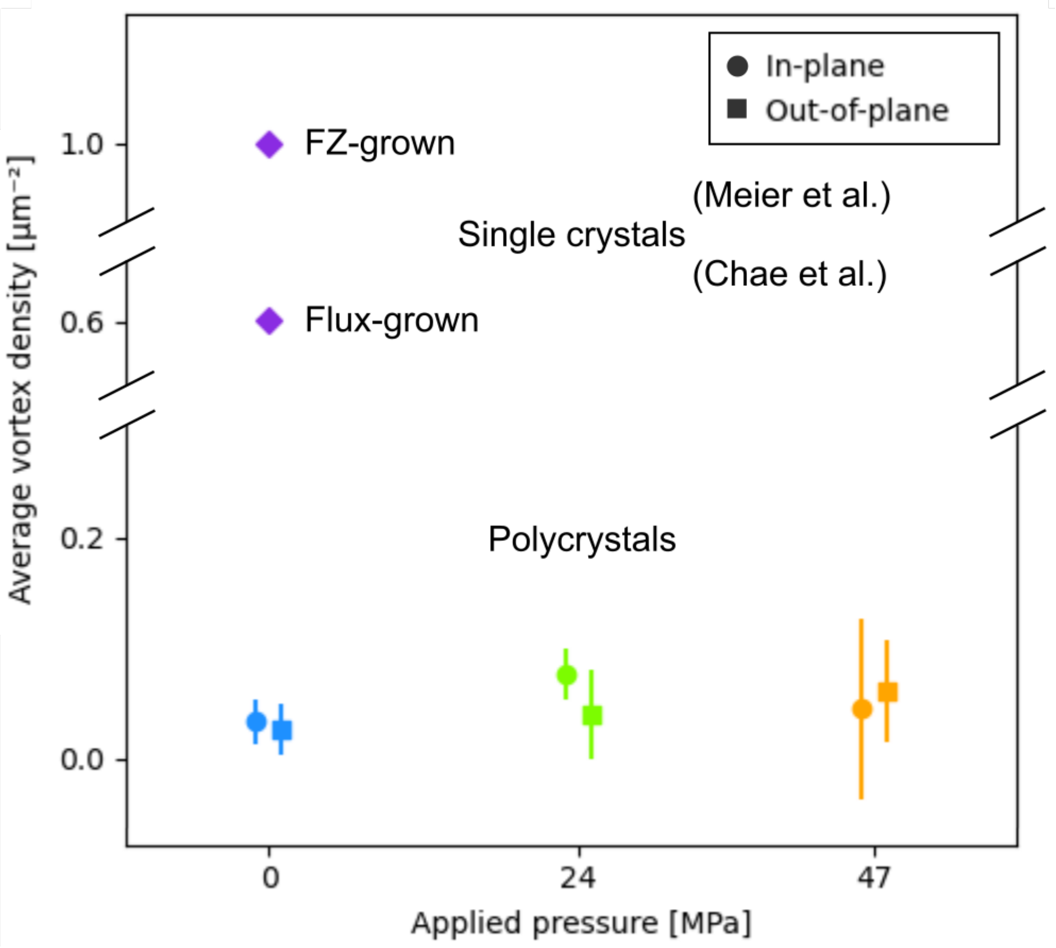

Figure 4.3.6: Average vortex density for the polycrystalline $ErMnO_3$ samples cooled under different pressures at a rate of $5\,^{\circ}\mathrm{C\,min^{-1}}$, compared to single crystals cooled at the same cooling rate. Single crystal values from refs. [24] and [33].

4.3.3 Ferroelectric domain transitions

Several of the grains investigated with PFM showed more than one type of domain structure; see Figure 4.3.3. This is not uncommon, and vortex and striped domains have been observed in the same grains before, as might be expected when there is a transition between the two [8]. Because of this, the grains hosting both striped and ripped domains are especially interesting as they indicate a transition between the two states. Interestingly, no mixed vortex and ripped domains have been observed. PFM images of different locations displaying mixed striped and ripped domains are shown in Figure 4.3.7. In Figures 4.3.7 a), b), and c), it appears that the striped domains merge into ripped domains as the stripes get narrower, while Figure 4.3.7 d) shows rather large stripes transitioning to ripped domains. In Figure 4.3.7 e), on the other hand, large blob-like domains (BLDs) appear at random locations within the striped domains. From Figure 4.3.7, it is also observed that most of the ripped domains are aligned within their grains, similar to the striped domains. The exception is the ripped domains in Figure 4.3.7 f), which show no particular alignment.

The BLDs within the striped domains, seen in Figure 4.3.7 e), were further investigated by the use of resonance PFM. High-resolution PFM images of BLDs are displayed in Figures 4.3.7 g) and h). The images show striped domains that appear to stop abruptly, resulting in BLDs. In Figure 4.3.7 g), two of the domains can be seen approaching one another and possibly forming a four-fold vortex. In Figure 4.3.7 h), a single domain penetrates the BLDs further than the rest but then appears to stop abruptly as well. The lateral resolution in these images is approximated as 12 nm from the tip radius and its relation to the resolution as described in section 2.5.1.

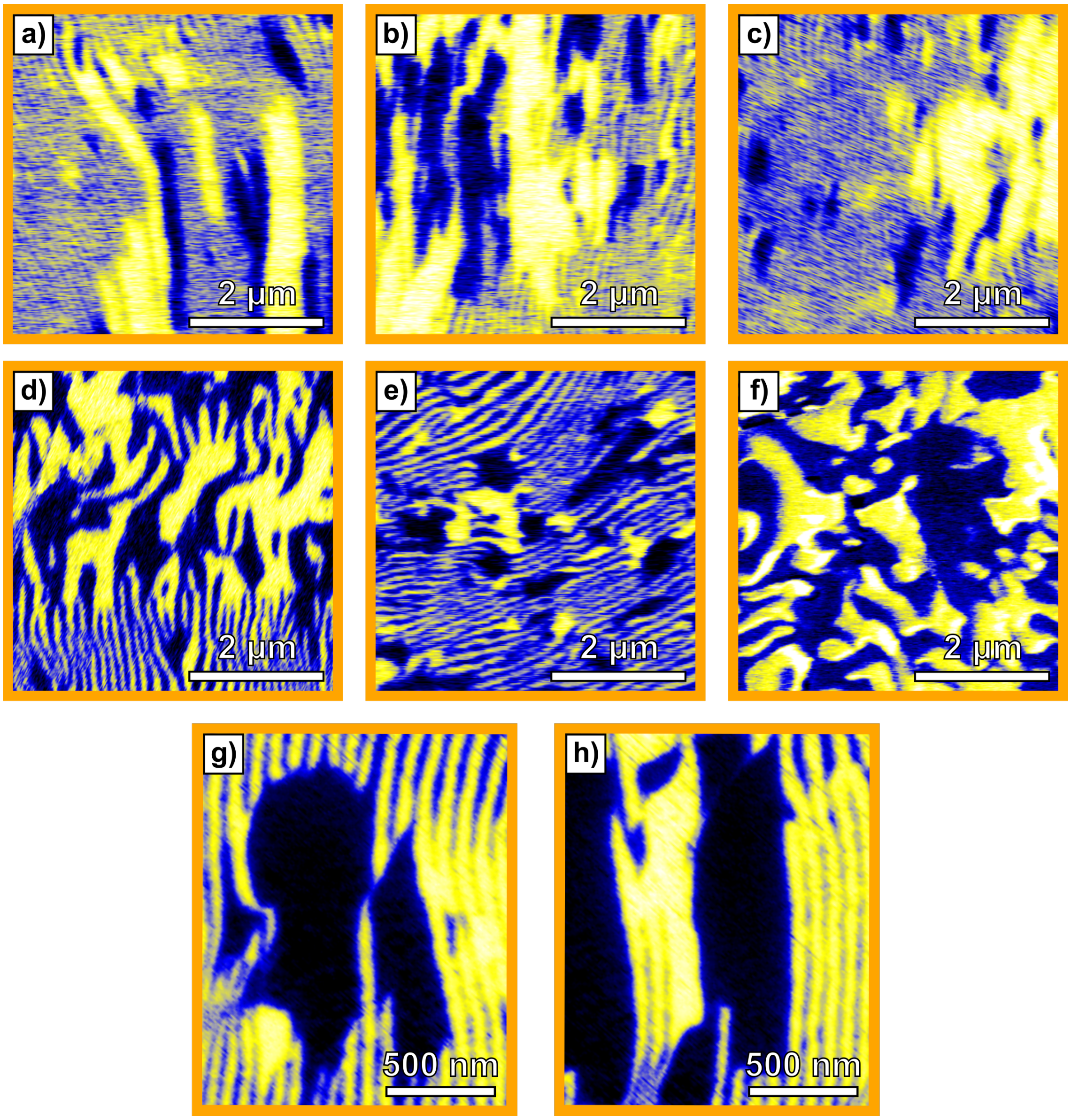

Figure 4.3.7: PFM images of domain transitions in the 47 MPa sample. a)-c) Smooth transitions from striped to ripped domains, d) more abrupt transition, e) BLDs in striped domains, f) non-directional ripped domain, and, g) and h) high-resolution images of BLDs.

4.4 Impact of grain orientation on the ferroelectric domain structure

4.4.1 Grain orientation analysis

Because the domain structure varied significantly from grain to grain in the 47 MPa sample, it was of interest to determine the effect of grain orientation on the domain structure. To obtain the orientations of the grains, EBSD was utilized to image an area previously imaged by PFM on the out-of-plane 47 MPa sample. The initial grain orientation analysis produced an orientation map of the scanned area, as seen in Figure 4.4.1. The area for which PFM scans were performed beforehand is highlighted in the middle of the orientation map. In the orientation map, the grains are colored based on their orientations, following the color key in the figure. White areas represent cavities and large cracks on the surface that could not be indexed. The orientation of the larger grains is further illustrated by small hexagonal unit cells, which more accurately depict their orientation. From the orientation map, no apparent preferential orientation for the grains is observed. Furthermore, a significant number of grains, approximately 400, was used to determine the texture of the sample.

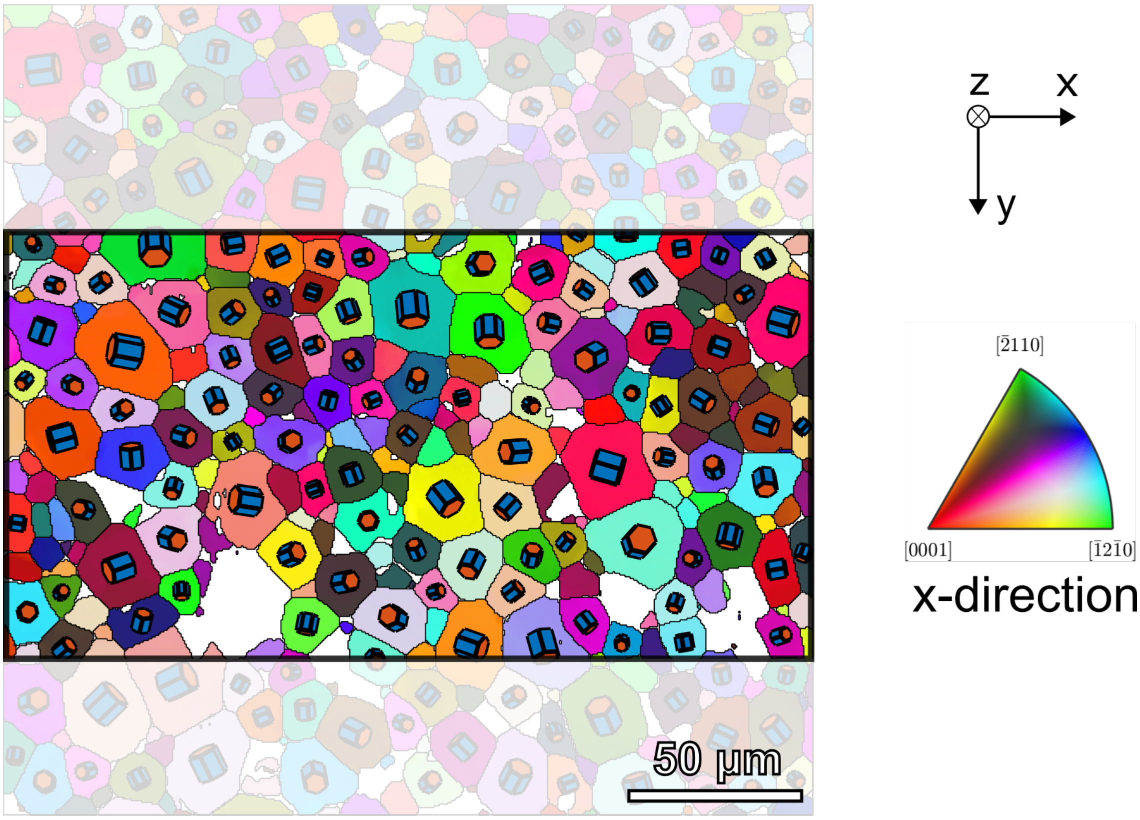

Figure 4.4.1: Orientation map of approximately 400 grains obtained from EBSD analysis. The hexagonal unit cells schematically display the orientation of the individual grains. PFM measurements are done in the highlighted region. The sample reference frame is illustrated by the coordinate system. The color key shows the grain color based on orientation with respect to the x-axis.

In addition to Figure 4.4.1, the pole figure and three inverse pole figures displayed in Figure 4.4.2 also suggest that the grains have no preferential orientation. The pole figure in Figure 4.4.2 a) shows the distribution of the {0001} plane normals (PNs) in the sample reference frame defined in Figure 4.4.1. From Figure 4.4.2 a), it is observed that the distribution of PNs is uniform. The inverse pole figures presented in Figures 4.4.2 b), c), and d) show the distribution of different crystal PNs for the x-, y-, and z-axis in the sample reference frame, respectively. To clarify, each point in an inverse pole figure corresponds to the PN of a grain. The different crystal planes are illustrated in Figure 4.4.2 e). The location of the point in the inverse pole figure describes the orientation of the grain PN with respect to the axis of the inverse pole figure. For example, if the inverse pole figure in Figure 4.4.2 d) had many points close to the [0001] corner, then many of the grains would have their [0001] PN close to parallel with the z-axis in the sample reference frame. However, the distributions of PNs in the inverse pole figures are also uniform, suggesting that the grains have no preferential orientation. The lack of a preferential orientation further supports the lack of creep during the thermomechanical treatment [105]. The MatLab code used to produce the different plots is presented in Appendix G.

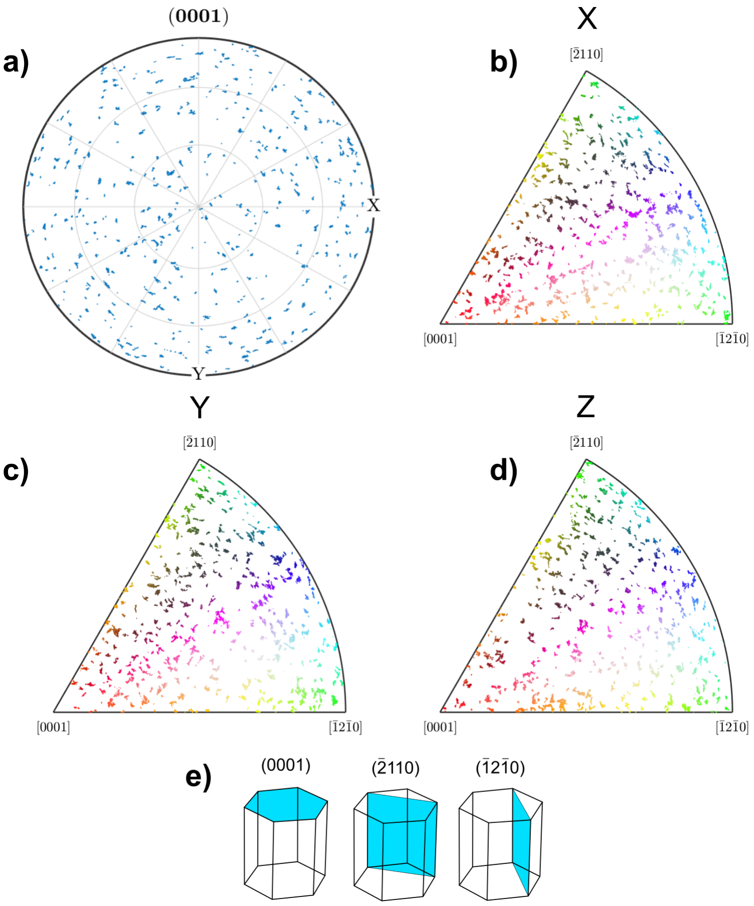

Figure 4.4.2: Uniform distribution of grain orientations in the 47 MPa sample illustrated by a) pole figure showing the distribution of {0001} plane normals in the sample reference frame, b), c), and d) inverse pole figures plotted for the sample directions X, Y, and Z. e) Illustrations of the different crystallographic planes represented in the pole and inverse pole figures. The sample directions refer to the different axes in the sample reference frame presented in Figure 4.4.1.

4.4.2 Grain orientation and ferroelectric domain structure

Figure 4.4.3 compares the domain structure of grains laying approximately in the xy-plane oriented at different angles with respect to the x-axis. The figure illustrates that the domain structure and contrast change as the grains are rotated around the z-axis. From the figure, it is observed that in the upmost row, where the grain is oriented at an angle of nearly 90° with respect to the x-axis, the vertical domain contrast dominates. The opposite is true for the lowest row, where the grain is oriented at nearly 0°, and the lateral domain contrast dominates. Figure 4.4.3 also shows that as the angle of the grain with respect to the x-axis increases from 0° to 90°, the ferroelectric domain structure transitions from striped to ripped. In addition, the figure also reveals that as the grain orientation changes, the direction of the domain walls changes accordingly such that they align with the c-axis of the unit cell. This is true for both the striped and ripped domains.

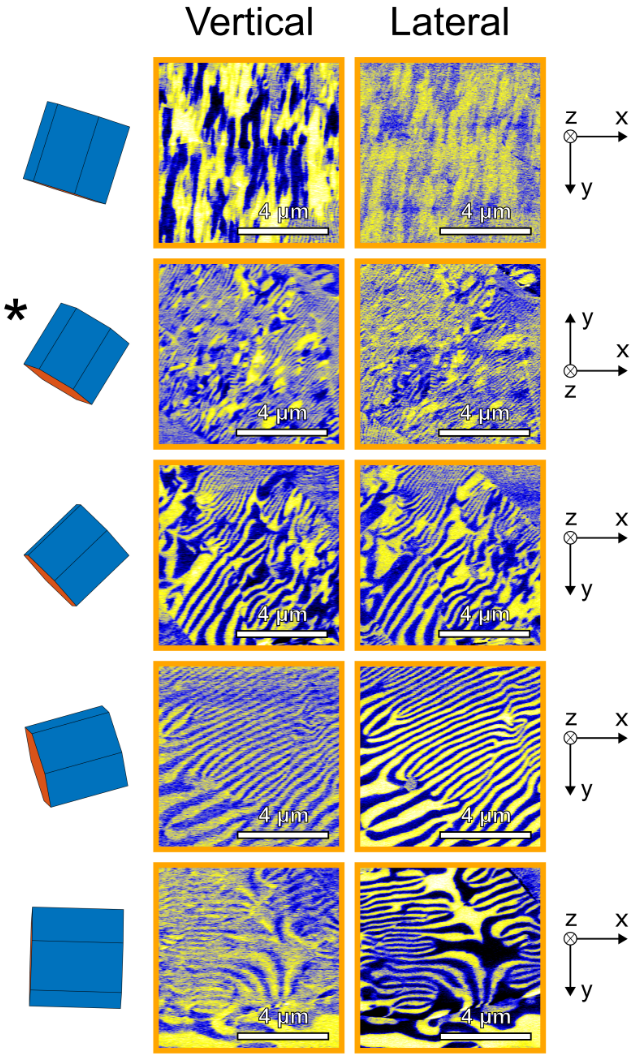

Figure 4.4.3: Grains lying approximately in the xy-plane rotated around the z-axis, illustrated by unit cells, compared with the change in PFM contrast and domain structure. The rotation means that the angle between the unit cells and the x-axis decreases downwards. The asterisk indicates that the unit cell and PFM images have been mirrored across a mirror plane along the x-axis.

As displayed in Figure 4.4.3, striped domains are observed when the grains are oriented at a low angle with respect to the x-axis, while ripped domains appear when the angle approaches 90°. This indicates a transition from striped to ripped domains, the angle of which was narrowed down to between 21.5° and 24.9° as shown in Figure 4.4.4. The figure shows the lowest angle at which ripped domains were observed, 24.9°, and the highest angle at which striped domains were observed, 21.5°. No ripped domains were found at a lower angle, and no striped domains were found at a higher angle, except for two grains, displayed in Figure 4.4.5. The two grains lying approximately in the xy-plane, with angles of 34.3° and 44.4° with respect to the x-axis, have vortex and striped domain structures, respectively. This indicates that they experienced a lower strain than their orientation would otherwise suggest. An explanation for this is found in the surroundings of the grains. Both grains were located adjacent to large cavities in the structure, which could have relieved some of the stress the grains experienced, similar to how pores reduce stress [106–108].

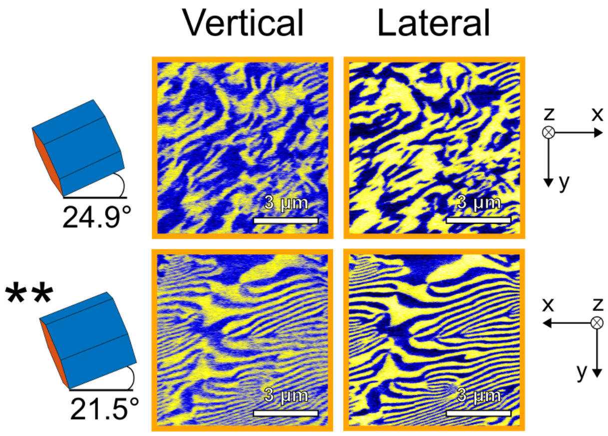

Figure 4.4.4: Orientation of grains, represented by unit cells, compared with a transition from striped to ripped domains. The double asterisk indicates that the unit cell and PFM images have been mirrored across a mirror plane along the y-axis.

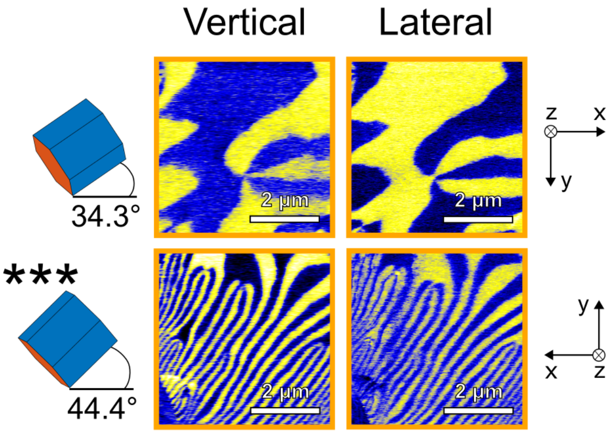

Figure 4.4.5: Two exceptions to the rotation of the unit cell and the formation of ripped domains. Both grains are adjacent to large cavities, which may have relieved the stress of the grains, allowing them to break the trend shown in Figure 4.4.4. The triple asterisk indicates that the unit cell and PFM images have been mirrored across mirror planes along the x-axis and y-axis.

After investigating how the domain structure and contrast of grains lying approximately in the xy-plane were affected by rotation around the z-axis, the effect of rotating around the y-axis was investigated as well. The result is shown in Figure 4.4.6 where the grain orientations with their respective ferroelectric domains are displayed. The rotation around the y-axis appears to affect the ferroelectric domain structure similarly to the rotation around the z-axis. That is, as the c-axis of the grains align more with the z-axis, the striped domains become narrower, and the domain structure changes from striped to ripped. In addition, the domain contrast changes from mostly lateral to primarily vertical. However, contrary to Figure 4.4.3, no alignment of the domain walls with the c-axis, and no transition angle for the appearance of ripped domains was observed. The code used to produce the unit cells in the plots is presented in Appendix H.

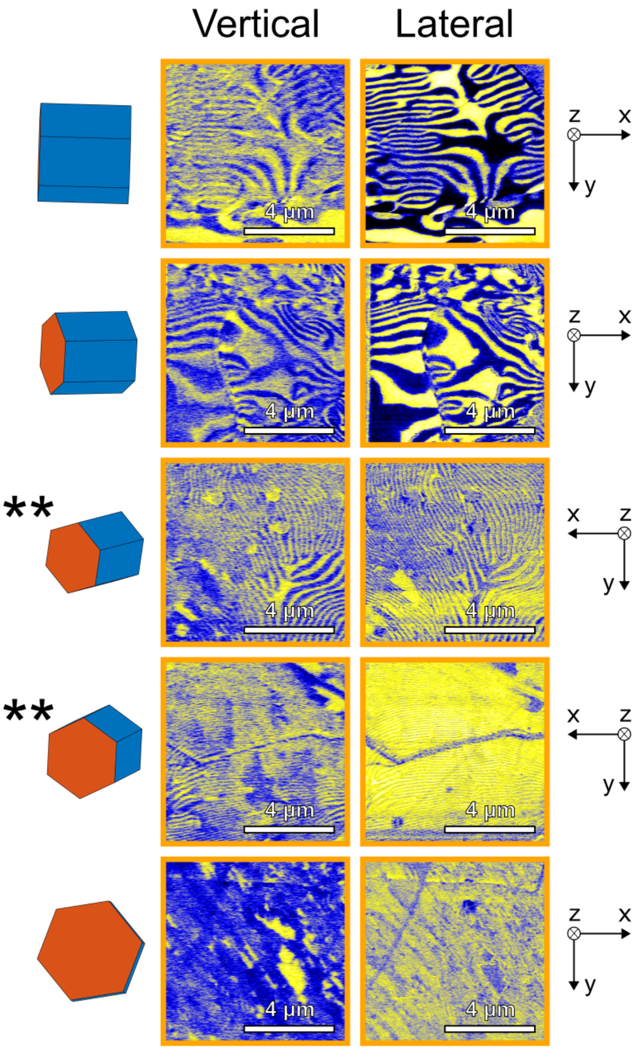

Figure 4.4.6: Representative grains lying approximately in the xy-plane rotated around the z-axis, illustrated by unit cells, compared with the change in PFM contrast and domain structure. The rotation means that the angle between the unit cells and the x-axis increases downwards. The double asterisk indicates that the unit cell and PFM images have been mirrored across a mirror plane along the y-axis.

Chapter 5

Impact of electric fields

After the study of the impact of mechanical pressure on the domain structure in chapter 4, this chapter will look into the impact of electric fields on the domain and domain wall dynamics in polycrystalline $ErMnO_3$. That is, this chapter will focus on the OR-sample introduced in section 3.4.

5.1 Piezoresponse force microscopy

Figure 5.1.1 shows both the vertical magnitude and phase from a PFM scan of the OR-sample. The analysis focuses on the central grain. The scanned area features both the vortex and striped domain structure as observed in other $ErMnO_3$ grains [8]. The vertical magnitude of the piezomechanical response is displayed in Figure 5.1.1 a). The figure shows that both domains have the same vertical magnitude as expected from the literature discussed in section 2.5.1. The vertical phase of the piezomechanical response is displayed in Figure 5.1.1 b), and illustrates that the domains have a phase difference of about 180°. Because the phase difference between the two domains is close to 180° in the vertical channel, the polarization of the central grain is probably mostly out-of-plane, although there might be in-plane contributions from buckling. Because of this, the rest of the analysis focuses on the vertical response of the sample.

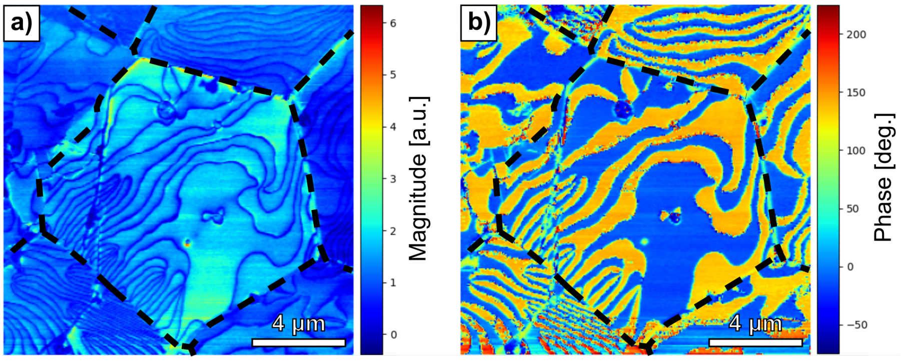

Figure 5.1.1: Vertical magnitude , a), and vertical phase, b), from PFM scan of the OR-sample. Grain boundaries are indicated by dashed black lines.

5.2 Switching spectroscopy PFM

To further probe the impact of electric fields on the ferroelectric domain structure of polycrystalline $ErMnO_3$, SS-PFM measurements were performed on the OR-sample. The piezoelectric response was measured at different applied voltages for each point in a 128×128 grid on the sample surface. Figure 5.2.1 displays the voltage-dependent vertical piezoelectric response of the OR-sample. The figure illustrates that the ferroelectric domain structure remains unaffected by the applied voltages. Additionally, in most regions, only a minor change in the piezoresponse is observed. However, a significant change in piezoresponse is observed in a few regions. One of these regions is indicated by a red dashed square. The origin of the piezoresponse change is investigated in the next paragraph. Finally, it is also noted that some change in the piezoresponse is observed at the grain boundaries, but this is not interesting because it correlates with the topography.

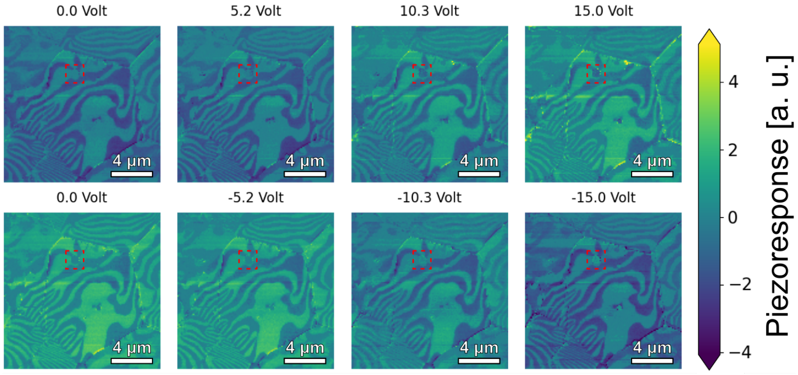

Figure 5.2.1: Piezoresponse of OR-sample as a function of applied voltage. The red dashed squares highlight the change in piezoelectric response.

To better visualize the areas where the piezoresponse was affected by the voltage, the difference between the piezoresponse at 15 V and -15 V was computed and is displayed visually in Figure 5.2.2 a). In the figure, the previously highlighted area from Figure 5.2.1 is clearly visible as a pore and again highlighted with a dashed red square. This area, along with other areas that show contrast in Figure 5.2.2 a) can be observed as topographic features in Figure 5.2.2 b). Interestingly, the pores in Figure 5.2.2 a) are dark, while the grain boundaries are bright. This reflects that their piezoresponse changed oppositely in response to the applied voltage.

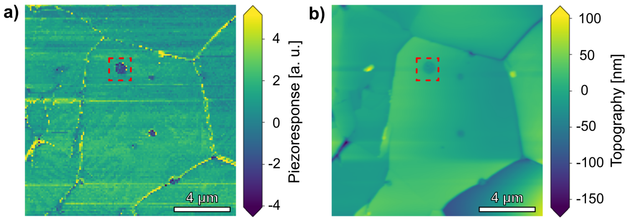

Figure 5.2.2: Comparison between difference in piezoresponse and topography of the OR-sample. Change in piezoresponse correlated to topography indicated by similarity between a) difference in piezoresponse at 15 V and −15 V, and b) topography of the OR-sample.

After having excluded the change in piezoresponse connected with the topographic features of the sample, the voltage-dependent piezoresponse of the domains and domain walls was investigated. Figure 5.2.3 shows the piezoresponse-voltage loops (PVLs) along several lines in the PFM image. The lines were drawn in the following way to explore the piezoresponse in and between different domains. First, the piezoresponse as a function of the applied voltage was investigated in a bright vortex domain, see Figure 5.2.3 a). The green PVLs show that the bright domain gives a positive piezoresponse regardless of the applied voltage and regardless of the position. When the positive voltage is applied, the piezoresponse remains constant at first and then suddenly increases at a critical voltage. Then when the negative voltage is applied, the piezoresponse again remains constant before suddenly returning to the low value at a critical negative voltage. The red line, displayed in figure 5.2.3 b), is drawn across a dark domain and connects two bright domains. The red PVLs illustrate that the same behavior is found in the dark domains, where the piezoresponse is negative regardless of the applied voltage. They also display a gradual change in the PVLs when transitioning from bright to dark vortex domains. The orange line, shown in Figure 5.2.3 c), is drawn across low-frequency striped domains. The orange PVLs illustrate that there are abrupt changes in piezoresponse between the dark and bright striped domains as well. Finally, the magenta line, displayed in Figure 5.2.3 d), is drawn to investigate striped domains with high frequency. The magenta PVLs show that the piezoresponse changes from positive to negative with the applied voltage, similar to hysteresis loops, see section 2.2. Because the magenta loops show a mixed positive and negative piezoresponse, it is difficult to discern which loop belongs to which domain type.

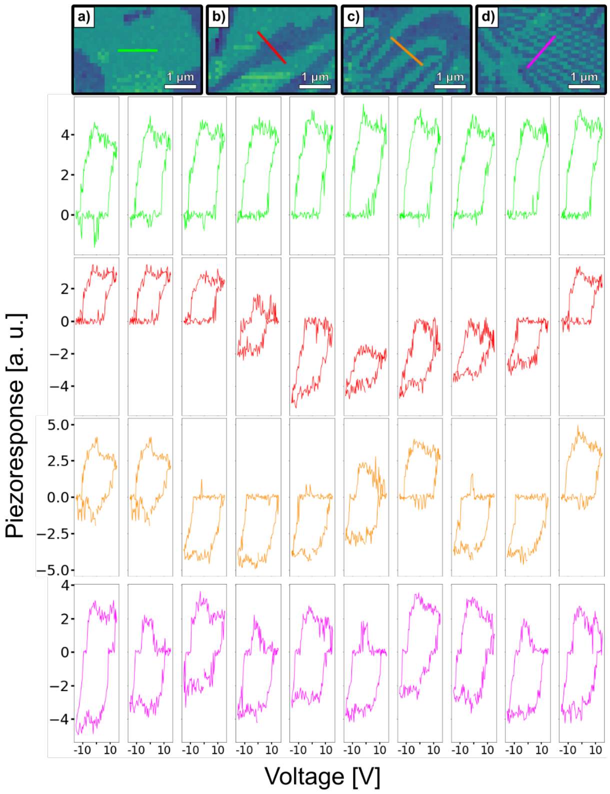

Figure 5.2.3: Piezoresponse-voltage loops along different lines in the vertical SS-PFM image. The top row displays the domains investigated with each line.

5.3 K-means clustering

In order to look for patterns in the piezoresponse of the sample, a k-means cluster analysis was performed. In short, the analysis uses machine learning to group locations from the SS-PFM based on how similar their voltage-dependent piezoresponse is. The result of the analysis for the region of interest, the central grain, is highlighted in Figure 5.3.1. The analysis was used to divide the grain into three clusters. Cluster 1 is blue, cluster 2 is orange, and cluster 3 is yellow. By comparing the cluster image in Figure 5.3.1 to the PFM images in Figure 5.2.1, it becomes clear that clusters 1 and 3 correspond to the bright and dark domains, respectively. The last cluster, cluster 2, corresponds to the domain walls separating the domains and the topographic features of the grain, such as the pore highlighted in Figure 5.2.2. However, not all of the domain walls are included in cluster 2.

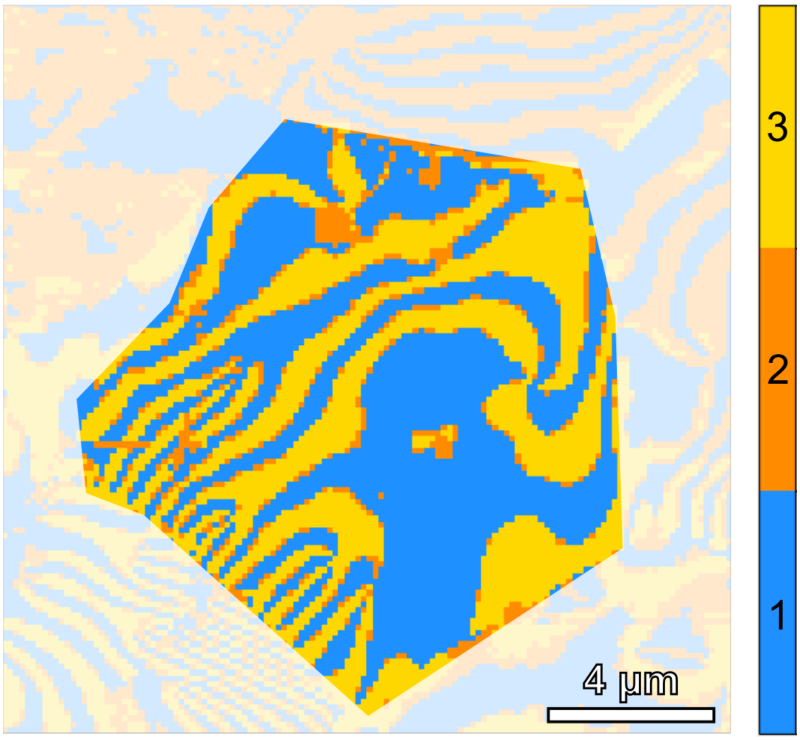

Figure 5.3.1: K-means cluster analysis of vertical SS-PFM data. The Python module used is presented in ref. [109].

Further inspection of the clusters was carried out by plotting the average piezoresponse of each cluster. The plots are displayed in Figure 5.3.2. The piezoresponse of cluster 1 initially decreases with the applied positive voltage before it quickly increases and reaches saturation at 15 V. Then when the voltage is decreased, the piezoresponse again increases until a critical voltage is reached around 0 V. As the voltage is decreased further, the piezoresponse rapidly decreases until saturation at −15 V is reached. Then finally, as the voltage again is increased, the piezoresponse starts to increase but then decreases until it reaches a minimum at 0 V. However, regardless of the applied voltage, the piezoresponse remains mainly positive. The same trend is observed for clusters 2 and 3. However, the piezoresponse of clusters

2 and 3 are shifted vertically downwards such that cluster 2 shows both negative and positive piezoresponse, and cluster 3 shows only a negative piezoresponse. It is observed that the piezoresponse of cluster 1 matches the piezoresponse observed for the bright domains in Figure 5.2.3, indicated by the green PVLs. Cluster 3, on the other hand, matches the dark domains with its continuously negative piezoresponse, while cluster 2 matches the piezoresponse observed at the domain walls, which transitions from positive to negative depending on the applied voltage.

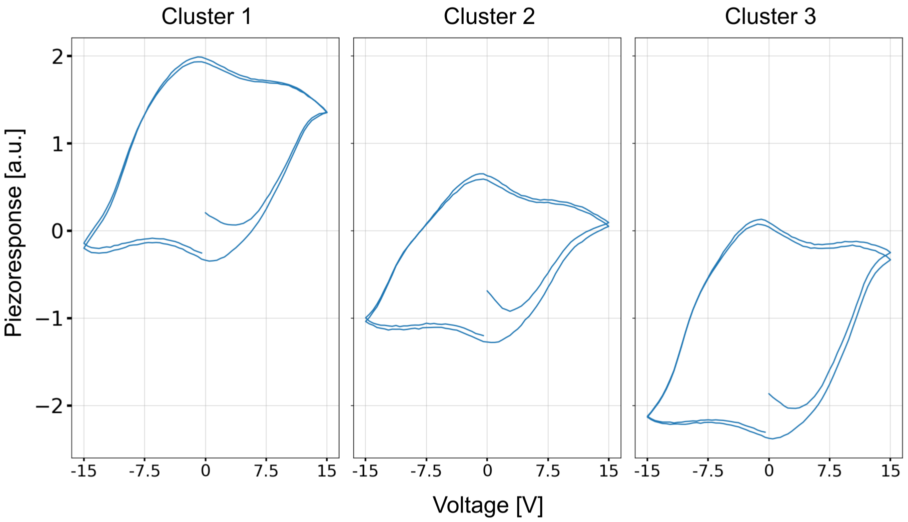

Figure 5.3.2: Mean piezoresponse of clusters from k-means cluster analysis.

An additional analysis of the impact of electrical fields, not included here, is presented in Appendix E. The Python code used to perform the different analyses of the electric fields on the domain structure is presented in Appendix F.

Chapter 6

Discussion

6.1 Structural and microstructural analysis

The initial characterization of the structure was done through XRD. The absence of secondary phases in the X-ray diffractogram, see Figure 4.1.1, indicates that the $ErMnO_3$ did not react with the MnO. From literature, it is established that high temperature and pressure can affect the grain size of ceramics [110]. Therefore, further characterization was carried out with SEM. The SEM micrographs in Figure 4.2.1 display an average grain size of $12.8 \pm 1.7\,\mu m$ regardless of the applied pressure, and indicate the minuscule effect of the applied pressure on the grain size. Considering this, it is likely that the changes observed in the ferroelectric domain structure originate from the strain induced by the applied pressure and not a change in grain size, as previously observed for grains varying between 1.5 µm and 19.0 µm in size [8]. Additional evidence of the structural rigidity of the samples was found when EBSD was performed. The pole and inverse pole figures presented in Figure 4.4.2, showed that the approximately 400 grains investigated had no preferential orientation, indicating the absence of creep in the 47 MPa sample [105].

Another observed feature of the microstructure is inter- and intragranular cracks. Cracks are present in all the samples, as observed in Figure 4.2.1. These cracks are likely due to significant thermal stresses induced during cooling [102, 103]. Cracks influence the formation of ferroelectric domains by releasing stress. Thus, cracks appearing during the annealing could reduce the stress experienced by the grains and affect the resulting domain structure. However, in most cases, the effect is negligible, and the domain walls continue across the cracks as in Figures 4.2.1 b) and c).

6.2 Global stress fields

The ferroelectric domain structure observed in the 0 MPa polycrystalline $ErMnO_3$ sample, displayed in Figure 4.3.1, is similar to the one described by Shultheiß et al.[8]. The similarities include the presence of both the vortex and striped domains, as well as the confinement of ferroelectric domains to their respective grains, and the tendency of domain walls to orient themselves with an angle of approximately 90° to the grain boundaries. The two domain structures observed, the vortex and striped domains, have also been thoroughly documented for hexagonal manganite single crystals previously [13, 27, 34, 56, 111]. However, in this thesis, the elastic strain has been included as an additional degree of freedom and given rise to new features not reported in the literature. These features include striped domains with domain walls oriented parallel to the c-axis of the grain, as in Figure 4.4.3, and a strong correlation between the domain frequency and the elastic strain illustrated in Figure 4.3.4. In addition to these new features, a novel domain structure called ripped domains, see Figure 4.3.3, has also been observed in the most strained sample. The different features will be discussed further in the following paragraphs.

As mentioned in the previous paragraph, the application of uniaxial pressure on the samples significantly impacted their domain structures. For instance, as shown in Figure 4.3.5, the higher the applied pressure, the higher the average domain frequency. The 0 MPa sample had an average domain frequency of $0.55\,\mu\mathrm{m}^{-1}$ while the 47 MPa sample had an average domain frequency of $2.42\,\mu\mathrm{m}^{-1}$. This correlation is thought to originate from the creation, annihilation, and expulsion of vortex pairs which divides the vortex domains into narrower striped domains as described in section 2.4. That strain can move vortices and cause vortex domains to evolve into striped domains have been shown experimentally and with phase-field simulations for single crystals [34, 75, 84]. However, this is the first experimental study of the effect in polycrystalline hexagonal manganites. The results of which, presented in Figures 4.3.1 and 4.3.2, show that the same trend holds for polycrystalline samples.

In contrast to the average domain frequency, the average vortex density did not change significantly with the applied pressure, as seen in Figure 4.3.6. There are two plausible contributions to this. The first contribution comes from the movement, creation, and annihilation of vortices. At higher applied pressures, many vortices are likely driven out of the grains, reducing the number of vortices [34]. However, at the same time, some grains will contain more vortices because vortices can also be created by strain [75]. If the two effects cancel each other out, the average vortex density will remain constant for the different pressures. The second contribution to the constant vortex density is how the vortices were counted. In the case of the 47 MPa sample, the ripped domains were not included in the count, as they presented a major uncertainty. If they had been included, the average vortex density of the 47 MPa sample would have been lower because no vortices were observed in the ripped domains.

The influence of the creation and expulsion of vortices with the applied pressure is clearly visible in the standard deviations of the average vortex densities, represented by the error bars in Figure 4.3.6. In the 0 MPa sample, the grains contain vortex domains that are mostly the same size and thus have nearly the same number of vortices per area. At the higher pressures, on the other hand, the grains are divided into two categories: type 1, with none or very few vortices, and type 2, with many vortices. This duality results in the large standard deviations apparent in the figure.

Another interesting feature of Figure 4.3.6 is the large difference in vortex density between the polycrystalline 0 MPa sample and the single crystals from the literature. The single crystals have average vortex densities more than 6 and 10 times larger than that observed in the 0 MPa sample, even though they were all cooled at the same rate. The origin of this discrepancy is likely the annihilation of vortex cores at the grain boundaries due to intergranular stresses present in all polycrystalline samples [8].

6.3 Local strain fields

Thus far, the discussion has focused on the average domain structure of the samples. This section, on the other hand, will focus on the effect of the grain orientation on the local domain structure. This was investigated by the use of PFM followed by EBSD at the same location on the 47 MPa sample. Figures 4.4.3 and 4.4.6 show the three trends observed. The first trend is that as the orientations of the grains change, the domain contrasts change too. This is expected as the polarization in $ErMnO_3$ lies parallel with the c-axis of the grain and thus changes with its orientation. For instance, in Figure 4.4.3, the upmost row displays good vertical contrast and poor lateral contrast. This is because the c-axis of the upmost grain points in the y-direction in the xy-plane, which causes the cantilever of the PFM to buckle since the scan is along the x-direction. This phenomenon is described in more detail in section 2.5.1. The lowest row in Figure 4.4.6 also shows a better vertical contrast than lateral because the c-axis points out of the xy-plane and thus causes deflection of the PFM cantilever. The opposite is seen in the lowest row in Figure 4.4.3, where the c-axis is aligned with the x-axis resulting in torsion of the PFM cantilever and a lateral signal.

The second trend observed in Figures 4.4.3 and 4.4.6 is that there is a change in the domain structure of the grains as their orientation changes. For example, in Figure 4.4.3, the two lower rows display grains with striped domains where the c-axes of the grains are close to parallel with the x-axis. However, in the upper rows, where the c-axis is closer to parallel with the y-axis, narrower striped domains and ripped domains are observed. This change in domain structure indicates that the grains experience different strains at different orientations as these are correlated [34, 75, 84]. Figure 4.4.6 also shows a gradual change in the domain structure where the striped domains get narrower and eventually ripped when moving downwards in the figure.

The third trend, observed in Figure 4.4.3, is that the domain walls in both the striped and ripped domains align parallel to the c-axis of the grain they are in. This could suggest that the vortex cores travel more easily along the c-axis of the crystal structure. The reason for this might be that there is less resistance along the c-axis for the vortex core or because this is the axis in which the Magnus-type force discussed in section 2.4 is pushing the vortex cores. However, the same trend is not seen in Figure 4.4.6. In this figure, the domain walls orient in the same direction within each grain, but the direction does not appear to correlate with the orientation of the grain. This could indicate that the strains in these grains are primarily induced by neighboring grains pressing on the grains instead of the orientation of the grains.

In order to further study the trends related to domain structure, a simple program was written to simulate a grain under uniaxial pressure at different orientations and calculate the associated experienced strains. The workings of the program are explained in detail in Appendix C, and the Python code for the program is included in Appendix **??**. Figure 6.3.1 displays a plot of the simulated strains experienced by a grain lying in the xy-plane rotated around the z-axis, similarly to the grains in Figure 4.4.3. The plot shows that the difference between ε_{xx} and ε_{yy} increases as the c-axis of the grain approaches parallel with the x-axis, or an angle of 90°. From literature, it is theorized that this should increase the movement of the vortices and lead to more and narrower striped domains [34, 75, 84]. However, this is the opposite of what was observed in Figure 4.4.3, where the striped domains are narrower in the grains with a c-axis close to parallel with the y-axis or 0°.

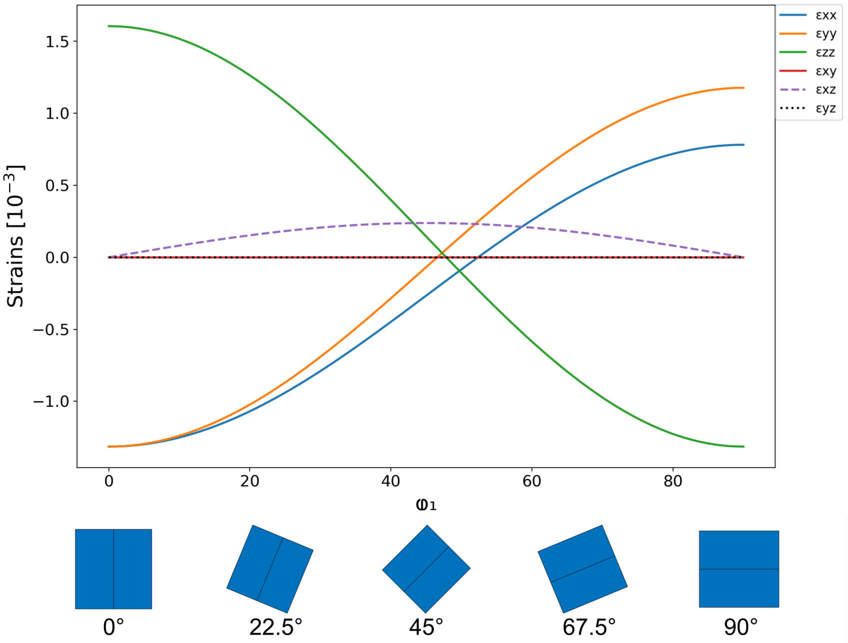

Figure 6.3.1: Simulated strains with the application of 47 MPa along the y-axis as a function of rotating the unit cell around the z-axis.

To investigate the trend observed in Figure 4.4.6, the same program was used to simulate an orientation around the y-axis. Because the uniaxial pressure is applied parallel to the y-axis, a grain rotation around the y-axis should not change the experienced strain in the grain, as the plot shows. However, Figure 4.4.6 demonstrates that the ferroelectric domains do change when the grain is rotated around the y-axis. An explanation for this is found when one considers that the simple program does not take strains from intergranular interactions into account. Thus, the change in domain structure observed in Figure 4.4.6 suggests that the influence of intergranular stresses from neighboring grains on the domain structure is significant.

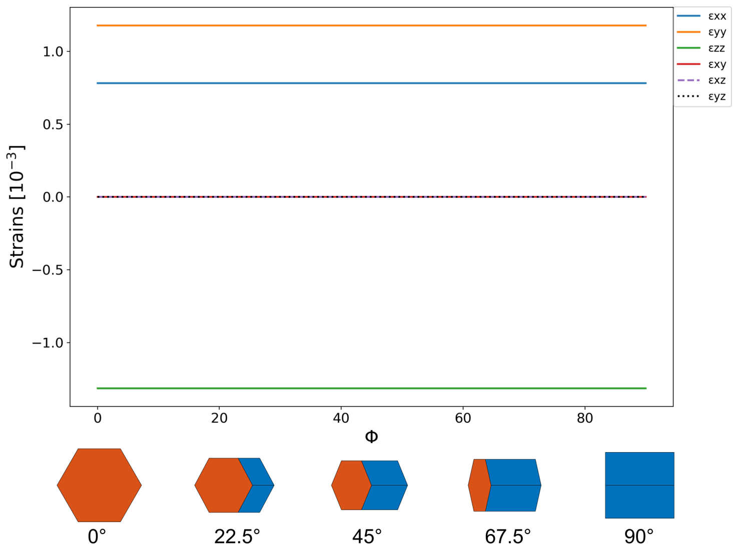

Figure 6.3.2: Simulated strains with the application of 47 MPa along the y-axis as a function of rotating the unit cell around the y-axis.

6.4 Ripped domains

Thus far, two types of domain structures have been reported in the literature, vortex domains and striped domains, presented in Figures 4.3.3 a) and b), respectively [27, 34, 56, 111]. Interestingly, this study has discovered a potentially new type of domain structure called ripped domains, displayed in Figure 4.3.3 c). As seen in the figure, the ripped domains are fundamentally different from the vortex and striped domains. In addition to the ripped domains, another domain structure was found in some of the striped domains, where the striped domains appear to stop abruptly, forming a BLD. These BLDs are presented in Figure 4.3.7 e). The ripped domains and the BLDs are only found in the 47 MPa sample and are therefore thought to be the result of strains exceeding what is required for the formation of striped domains. Furthermore, because both phenomena appear to break the normal ordering of the domains observed in the vortex and striped domains, and because it is difficult to distinguish between mixed striped and ripped domains and striped domains with BLDs, the two phenomena are likely connected. One possibility is that the BLDs are the precursor for the ripped domains. With this in mind, the origins of the two phenomena will be discussed together in the following paragraphs.

The first hypothesis is that the phenomena are directly caused by increased strains, similar to how increased strains transform vortex domains into striped domains as discussed in section 2.4. The first evidence supporting this hypothesis is the fact that ripped domains have only been observed in the 47 MPa sample, indicating that the strains in the 0 MPa and 24 MPa samples are not adequate. The second piece of evidence is that, as discussed in the previous section, there is a strong correlation between the orientations of the grains and the strains they experience. This is further evidence because the ripped domains are only found at specific orientations within the 47 MPa sample. To be more specific, as Figure 4.4.4 shows, the ripped domains in grains lying in the xy-plane are only observed when the grains have an angle of more than or equal to 24.9° with respect to the x-axis. The figure also shows that vortex and striped domains in these grains are only observed at angles equal to or below 21.5° with respect to the x-axis. The two exceptions to this, shown in Figure 4.4.5, are likely a result of the large neighboring cavities, which can relieve the stress these grains experienced, similar to pores discussed in literature [106–108]. Further support for the hypothesis that ripped domains are a result of great strains comes from Figure 4.3.7. The figure displays several examples of mixed striped and ripped domains in the 47 MPa sample, similar to the mixed vortex and striped domains found in the 24 MPa sample as shown in Figure 4.3.2 b). Especially interesting are Figures 4.3.7 a), b), and c), where there is a smooth transition from striped domains to ripped domains as the striped domains get narrower. This gradual constriction of the domains suggests the presence of a strain gradient and that the ripped domains occur at the highest strain. This would be equivalent to the transition from vortex domains to striped domains.

The second hypothesis for the formation of the ripped domains is that the strain is an indirect cause and that the direct cause of the ripped domains is PEDs, discussed in section 2.4. These PEDs can allow the formation of AP and FE domain walls which breaks the typical domain sequence. Furthermore, it has been found that PEDs can be introduced in $BaTiO_3$ when a uniaxial pressure of 20-50 MPa is applied [32]. It is therefore not unreasonable to assume that some PEDs might have formed in the polycrystalline $ErMnO_3$ sample, which was exposed to a uniaxial pressure of 47 MPa, even though there are no indications of creep in the sample. Because the BLDs in Figure 4.3.7 e) appear to break the typical domain sequence, they were investigated further with high-resolution resonance PFM. The idea was to try and observe very thin domains passing through the BLDs. The images from the investigation are shown in Figures 4.3.7 g), and h), and have an approximate resolution of 12 nm. No thin domains were observed to pass through the BLDs in the images, suggesting that the striped domains do not shrink. However, even with the high resolution, it is possible that the domains have become too narrow to be resolved from the surrounding domains, as they can become as narrow as a few unit cells in theory [78]. A plausible cause for such an anisotropic shrinkage of one domain type is self-poling, as observed for vortex domains by Chae et al. [77]. This self-poling was thought to be caused by a difference in the oxygen content on the surface and in the bulk, making the negatively charged domains more energetically favorable on the surface and leading to the shrinkage of the positively charged surface domains. A similar effect may be the cause of the observed BLDs if the high strains experienced by the grains affect the density of oxygen or other elements on the surface of the grains. Further investigation of, for instance, defect densities is required to resolve the question of the origin of blob-like and ripped domains.

6.5 Domain dynamics in polycrystalline $ErMnO_3$

The electrical probing of the domain dynamics in the OR-sample bore several interesting results. For instance, Figure 5.2.1 which displays the vertical piezoresponse as a function of the applied voltage, shows that the piezoresponse in most areas remained unchanged by the applied voltages. Only in a few areas was a noticeable change in the piezoresponse observed. However, the change in piezoresponse in these areas was found to be correlated with the topographic features of the grain, as shown in Figure 5.2.2, and thus not considered ferroelectric switching. Furthermore, no change in the domain structure was observed. This might be due to domain wall pinning by defects, or a higher coercive field due to the small grain size [22, 112].

Further analysis of the domain dynamics was done by analyzing the change in piezoresponse at different voltages along lines in different domain structures, as shown in Figure 5.2.3. The line analysis showed that the piezoresponse remained positive in the bright domains and negative in the dark domains regardless of the applied voltage. This could indicate that there is no ferroelectric switching in the domains. The line analysis also showed that the transition across domains could be both gradual and abrupt, which might be influenced by domain wall movement. That is, if a domain wall moves towards the tip in response to the applied voltage, it is expected that the piezoresponse would change more gradually than if there was no domain wall movement [5]. This is because, as the tip moves from one domain to another, it picks up a mixed piezoresponse of the two adjacent domains. The area where it picks up this mixed response is increased if the domain wall moves with the tip. The line analysis also found that for high-frequency striped domains, the loops remained almost constantly in a mixed positive and negative state, similar to what was observed at the transition between domains in Figure 5.2.3. This result could stem from an average piezoresponse of the adjacent domains, as mentioned in ref. [5], but domain wall movement could also be involved.

The results from the line analysis discussed in the previous paragraph were further investigated through k-means clustering. The k-means clustering analysis grouped regions of the sample into three different clusters based on how similar the piezoresponse was at the different applied voltages. The resulting clusters, displayed in Figure 5.3.1, are easily explained by comparing the figure with Figure 5.2.1. Cluster 1 corresponds to the bright domains seen in Figure 5.2.1, while cluster 3 corresponds to the dark domains. The last cluster, cluster 2, corresponds to the domain walls and the topographic features of the grain. These observations are further supported by the similarities between the PVLs from the line analysis and the average PVLs of the clusters shown in Figure 5.3.2. The average PVLs, shown in Figure 5.2.1, better illustrate the voltage-dependent piezoresponse of the different domains by reducing the noise that is seen in the line analysis figure. The loops show that cluster 1 and cluster 3 remain positive and negative, respectively, regardless of the applied voltage. Figure 5.2.1, also shows that the loops, although they resemble the hysteresis loop in Figure 2.2.4, are different. The biggest difference being the increase in piezoresponse when the positive voltage is reduced back to zero. From the different analyses of the voltage-dependent piezoresponse, it is not possible to conclude whether there is ferroelectric switching in the sample or not. The change in piezoresponse can stem from ferroelectric switching, but alternate candidates include Maxwell stress [113], joule heating [114] and charge injection [115].

Chapter 7

Conclusion and outlook

The aim of this thesis was to investigate the impact of mechanical pressure and electric fields on the ferroelectric domain structure in polycrystalline $ErMnO_3$, which is of special interest due to its robust domain structure and relatively easy synthesis. This was primarily done using EBSD, PFM, and SS-PFM. The main conclusion from the experiments is that the domain structure of hexagonal $ErMnO_3$ can be engineered with non-uniform strain, while no apparent change was observed when electric fields were applied. The latter is possibly a result of domain wall pinning due to defects or the enhancement of the coercive field due to grain size. When influenced by strain, the domain structure gradually changes from vortex domains to striped domains, and the striped domains become narrower with higher strain. The engineering of the ferroelectric domains relies on the movement of the topologically protected vortex cores, which are not found in common ferroelectrics such as $BaTiO_3$ and $Pb[ZrTi]O_3$. In these ferroelectrics, the strain moves the ferroelectric domain walls resulting in a preferential orientation of the ferroelectric domains. The findings in this thesis show that the interaction between elastic strains and the topologically protected vortex cores supplies domain engineering with an additional tool applicable to materials that host topologically protected vortex cores. This includes other hexagonal manganites, hexagonal gallates, hexagonal tungsten bronzes, and hexagonal ferrites.

While a correlation between the orientation of the grains and the ferroelectric domain structure was found, future work should focus on improving the understanding of the strain fields in the polycrystalline material by utilizing finite element simulations. Such simulations could give insight into the relative importance of the grain orientation, geometry, and neighboring grains on the ferroelectric domain structure. It would also increase the understanding of the formation of striped and ripped domains. Further investigation of the ripped domains could include the use of HAADF imaging to get a better understanding of the mechanisms on the unit cell scale. It would also be interesting to probe deeper into the samples to see how the ripped domains penetrate into the bulk. Lastly, temperature- and frequency-dependent dielectric spectroscopy measurements are of importance to evaluate the collective piezo- and dielectric response of the domain walls in the material for future applications in actuators, capacitors, and more.

Bibliography

[1] J. Valasek. ‘Piezo-electric and allied phenomena in Rochelle salt’. In: *Physical Review* 17.4 (1921), pp. 475–481. DOI: 10.1103/PhysRev.17.475.

[2] G. H. Haertling. ‘Ferroelectric Ceramics: History and Technology’. In: *Journal of the American Ceramic Society* 82.4 (1999), pp. 797–818. DOI: 10.1002/9783527618002.ch6.

[3] J. F. Scott. ‘Applications of modern ferroelectrics’. In: *Science* 315.5814 (2007), pp. 954–959. DOI: 10.1126/science.1129564.

[4] R. J. D. Tilley. *Understanding Solids*. 2nd. John Wiley & Sons, Ltd., 2013. ISBN: 9781118423288.

[5] E. Soergel. ‘Piezoresponse force microscopy (PFM)’. In: *Journal of Physics D: Applied Physics* 44.46 (2011). DOI: 10.1088/0022-3727/44/46/464003.

[6] C. Tan et al. ‘Engineering polar vortex from topologically trivial domain architecture’. In: *Nature Communications* 12 (2021), pp. 1–8. DOI: 10.1038/s41467-021-24922-y.

[7] D. Meier and S. M. Selbach. ‘Ferroelectric domain walls for nanotechnology’. In: *Nature Reviews Materials* 7 (2021), pp. 157–173. DOI: 10.1038/s41578-021-00375-z.

[8] J. Schultheiß et al. ‘Confinement-driven inverse domain scaling in polycrystalline $ErMnO_3$’. In: *ArXiv* (2022). DOI: 10.48550/arXiv.2204.07979.

[9] J. L. Jones et al. ‘Direct measurement of the domain switching contribution to the dynamic piezoelectric response in ferroelectric ceramics’. In: *Applied Physics Letters* 89.9 (2006), pp. 1–4. DOI: 10.1063/1.2338756.

[10] Q. M. Zhang et al. ‘Direct evaluation of domain-wall and intrinsic contributions to the dielectric and piezoelectric response and their temperature dependence on lead zirconate-titanate ceramics’. In: *Journal of Applied Physics* 75.1 (1994), pp. 454–459. DOI: 10.1063/1.355874.

[11] R. Xu et al. ‘Stationary domain wall contribution to enhanced ferroelectric susceptibility’. In: *Nature Communications* 5 (2014), pp. 1–7. DOI: 10.1038/ncomms4120.

[12] D. Meier et al. ‘Observation and coupling of domains in a spin-spiral multiferroic’. In: *Physical Review Letters* 102.10 (2009), pp. 1–4. DOI: 10.1103/PhysRevLett.102.107202.

[13] D. Meier et al. ‘Anisotropic conductance at improper ferroelectric domain walls’. In: *Nature Materials* 11.4 (2012), pp. 284–288. DOI: 10.1038/nmat3249.

[14] L. Puntigam et al. ‘Insulating improper ferroelectric domain walls as robust barrier layer capacitors’. In: *Journal of Applied Physics* 129.7 (2021). DOI: 10.1063/5.0038300.

[15] M. E. Holtz et al. ‘Topological Defects in Hexagonal Manganites: Inner Structure and Emergent Electrostatics’. In: *Nano Letters* 17.10 (2017), pp. 5883–5890. DOI: 10.1021/acs.nanolett.7b01288.

[16] E. D. Roede et al. ‘Contact-free reversible switching of improper ferroelectric domains by electron and ion irradiation’. In: *APL Materials* 9 (2021). DOI: 10.1063/5.0038909.

[17] J. A. Mundy et al. ‘Functional electronic inversion layers at ferroelectric domain walls’. In: *Nature Materials* 16.6 (2017), pp. 622–627. DOI: 10.1038/nmat4878.

[18] Q. Zhang et al. ‘Direct observation of multiferroic vortex domains in $YMnO_3$’. In: *Scientific Reports* 3 (2013), pp. 1–5. DOI: 10.1038/srep02741.

[19] S. Cheng et al. ‘Topologically Allowed Nonsixfold Vortices in a Sixfold Multiferroic Material: Observation and Classification’. In: *Physical Review Letters* 118.14 (2017). DOI: 10.1103/PhysRevLett.118.145501.

[20] J. A. McNulty et al. ‘An Electronically Driven Improper Ferroelectric: Tungsten Bronzes as Microstructural Analogs for the Hexagonal Manganites’. In: *Advanced Materials* 31.40 (2019). DOI: 10.1002/adma.201903620.

[21] K. Du et al. ‘Vortex ferroelectric domains, large-loop weak ferromagnetic domains, and their decoupling in hexagonal (Lu, Sc)FeO_3’. In: *npj Quantum Materials* 3.1 (2018), pp. 1–7. DOI: 10.1038/s41535-018-0106-3.

[22] C. M. Fernandez-Posada et al. ‘Magnetoelastic properties of multiferroic hexagonal $ErMnO_3$’. In: *Journal of Magnetism and Magnetic Materials* 554 (2022). DOI: 10.1016/j.jmmm.2022.169277.

[23] T. Choi et al. ‘Insulating interlocked ferroelectric and structural antiphase domain walls in multiferroic $YMnO_3$’. In: *Nature Materials* 9.3 (2010), pp. 253–258. DOI: 10.1038/nmat2632.

[24] Q. N. Meier et al. ‘Global formation of topological defects in the multiferroic hexagonal manganites’. In: *Physical Review X* 7.4 (2017), pp. 1–10. DOI: 10.1103/PhysRevX.7.041014.

[25] S. M. Griffin et al. ‘Scaling behavior and beyond equilibrium in the hexagonal manganites’. In: *Physical Review X* 2.4 (2012), pp. 1–10. DOI: 10.1103/PhysRevX.2.041022.

[26] S. Z. Lin et al. ‘Topological defects as relics of emergent continuous symmetry and Higgs condensation of disorder in ferroelectrics’. In: *Nature Physics* 10.12 (2014), pp. 970–977. DOI: 10.1038/nphys3142.

[27] Z. Yan et al. ‘Growth of high-quality hexagonal $ErMnO_3$ single crystals by the pressurized floating-zone method’. In: *Journal of Crystal Growth* 409 (2015), pp. 75–79. DOI: 10.1016/j.jcrysgro.2014.10.006.

[28] H. Lu et al. ‘Nanodomain Engineering in Ferroelectric Capacitors with Graphene Electrodes’. In: *Nano Letters* 16.10 (2016), pp. 6460–6466. DOI: 10.1021/acs.nanolett.6b02963.

[29] G. Catalan et al. 'Fractal dimension and size scaling of domains in thin films of multiferroic $BiFeO_3$'. In: *Physical Review Letters* 100.2 (2008), pp. 35–38. DOI: 10.1103/PhysRevLett.100.027602.

[30] E. Hassanpour et al. 'Robustness of magnetic and electric domains against charge carrier doping in multiferroic hexagonal $ErMnO_3$'. In: *New Journal of Physics* 18.4 (2016). DOI: 10.1088/1367-2630/18/4/043015.

[31] Y. L. Li et al. 'Effect of electrical boundary conditions on ferroelectric domain structures in thin films'. In: *Applied Physics Letters* 81.3 (2002), pp. 427–429. DOI: 10.1063/1.1492025.

[32] M. Höfling et al. 'Control of polarization in bulk ferroelectrics by Mechanical Dislocation Imprint'. In: *Science* 372 (2021), pp. 961–964. DOI: 10.1126/science.abe3810.

[33] S. C. Chae et al. 'Direct observation of the proliferation of ferroelectric loop domains and vortex-antivortex pairs'. In: *Physical Review Letters* 108.16 (2012), pp. 1–5. DOI: 10.1103/PhysRevLett.108.167603.

[34] X. Wang et al. 'Unfolding of vortices into topological stripes in a multiferroic material'. In: *Physical Review Letters* 112.24 (2014), pp. 1–5. DOI: 10.1103/PhysRevLett.112.247601.

[35] B. D. Cullity and C. D. Graham. *Introduction to Magnetic Materials*. 2nd. John Wiley & Sons, Inc., 2009. ISBN: 978-0-471-47741-9.

[36] R. E. Newham and L. E. Cross. 'Symmetry of secondary ferroics. I'. In: *Materials Research Bulletin* 9.7 (1974), pp. 927–933. DOI: https://doi.org/10.1016/0025-5408(74)90172-X.

[37] A. K. Tagantsev, L. E. Cross and J. Fousek. *Domains in Ferroic Crystals and Thin Films*. 1st ed. New York: Springer Science + Business Media, LLC, 2010. ISBN: 978-1-4419-1417-0. DOI: 10.1007/978-1-4419-1417-0.

[38] V. K. Wadhawan. *Introduction to Ferroic Materials*. 1st. London: CRC Press, 2000. ISBN: 9780429180385.

[39] R. E. Newnham. *Properties of Materials: Anisotropy, Symmetry, Structure*. New York: Oxford University Press, 2005. ISBN: 0-19-852076-x.

[40] B. B. Van Aken et al. 'Observation of ferrotoroidic domains'. In: *Nature* 449 (2007), pp. 702–705. DOI: 10.1038/nature06139.

[41] S. Gnewuch and E. E. Rodriguez. 'The fourth ferroic order : Current status on ferrotoroidic materials'. In: *Journal of Solid State Chemistry* 271 (2019), pp. 175–190. DOI: 10.1016/j.jssc.2018.12.035.

[42] H. Schmid. 'Multi-ferroic magnetoelectrics'. In: *Ferroelectrics* 162.1 (1994), pp. 317–338. DOI: 10.1080/00150199408245120.

[43] T. Lottermoser and D. Meier. 'A short history of multiferroics'. In: *Physical Sciences Reviews* 6.2 (2020). DOI: https://doi.org/10.1515/psr-2020-0032.

[44] M. Fiebig et al. 'The evolution of multiferroics'. In: *Nature Reviews Materials* 1.8 (2016). DOI: 10.1038/natrevmats.2016.46.

[45] A. Bauer and C. Pfleiderer. *Topological Structures in Ferroic Materials: Domain Walls, Vortices and Skyrmions*. Springer International Publishing, 2016. ISBN: 978-3-319-25299-5. DOI: 10.1007/978-3-319-25301-5.

[46] T. Brandvik. 'Ferroelectric Transitions in $Sr_xBa_{1-x}Nb_2O_6$'. Norwegian University of Science and Technology, Trondheim, 2015.

[47] J. Seidel et al. 'Nanoscale probing of high photovoltages at 109° domain walls'. In: *Ferroelectrics* 433.1 (2012), pp. 123–126. DOI: 10.1080/00150193.2012.678156.

[48] D. R. Småbråten et al. 'Charged domain walls in improper ferroelectric hexagonal manganites and gallates'. In: *Physical Review Materials* 2.11 (2018), pp. 1–9. DOI: 10.1103/PhysRevMaterials.2.114405.

[49] S. Choudhury et al. 'The influence of 180° ferroelectric domain wall width on the threshold field for wall motion'. In: *Journal of Applied Physics* 104.8 (2008). DOI: 10.1063/1.3000459.

[50] J. Schultheiß, T. Rojac and D. Meier. 'Unveiling Alternating Current Electronic Properties at Ferroelectric Domain Walls'. In: *Advanced Electronic Materials* (2021). DOI: 10.1002/aelm.202100996.

[51] V. Y. Shur. 'Fast Polarization Reversal Process: Evolution of Ferroelectric Domain Structure in Thin Films'. In: *Ferroelectric Thin Films: Synthesis and Basic Properties*. 1996. Chap. 6, pp. 154–192.

[52] M. Fiebig et al. 'Observation of coupled magnetic and electric domains'. In: *Nature* 419 (2002), pp. 818–820. DOI: 10.1038/nature01077.

[53] M. Lilienblum. 'Ferroelectric Order in Multiferroic Hexagonal'. PhD thesis. University of Bonn, 2016.

[54] B. Lorenz. 'Hexagonal Manganites—($RMnO_3$): Class (I) Multiferroics with Strong Coupling of Magnetism and Ferroelectricity'. In: *ISRN Condensed Matter Physics* 2013 (2013), pp. 1–43. DOI: 10.1155/2013/497073.

[55] B. B. Van Aken et al. 'The origin of ferroelectricity in magnetoelectric $YMnO_3$'. In: *Nature Materials* 3 (2004), pp. 164–170. DOI: 10.1038/nmat1080.

[56] M. Lilienblum et al. 'Ferroelectricity in the multiferroic hexagonal manganites'. In: *Nature Physics* 11.12 (2015), pp. 1070–1073. DOI: 10.1038/nphys3468.

[57] J. Shieh et al. 'Hysteresis behaviors of barium titanate single crystals based on the operation of multiple 90° switching systems'. In: *Materials Science and Engineering B: Solid-State Materials for Advanced Technology* 161.1-3 (2009), pp. 50–54. DOI: 10.1016/j.mseb.2008.11.046.

[58] J. R. Barkley and W. Jeitschko. 'Antiphase boundaries and their interactions with domain walls in ferroelastic-ferroelectric $Gd_2(MoO_4)_3$'. In: *Journal of Applied Physics* 44.3 (1973), pp. 938–944. DOI: 10.1063/1.1662376.

[59] K. Aizu. 'Possible Species of "Ferroelastic" Crystals and of Simultaneously Ferroelectric and Ferroelastic Crystals'. In: *Journal of the Physical Society of Japan* 27.2 (1969), pp. 387–396. DOI: https://doi.org/10.1143/JPSJ.27.387.

[60] C. Himcinschi et al. 'Ferroelastic domain identification in $BiFeO_3$ crystals using Raman spectroscopy'. In: *Scientific Reports* 9.1 (2019), pp. 1–9. DOI: 10.1038/s41598-018-36462-5.

[61] C. Wang et al. 'Ferroelastic switching in a layered-perovskite thin film'. In: *Nature Communications* 7 (2016). DOI: 10.1038/ncomms10636.

[62] A. S. Gibbs, K. S. Knight and P. Lightfoot. 'High-temperature phase transitions of hexagonal $YMnO_3$'. In: *Physical Review B - Condensed Matter and Materials Physics* 83.9 (2011), pp. 1–9. DOI: 10.1103/PhysRevB.83.094111.

[63] K. Momma and F. Izumi. 'VESTA 3 for three-dimensional visualization of crystal, volumetric and morphology data'. In: *Journal of Applied Crystallography* 44 (2011), pp. 1272–1276. DOI: https://doi.org/10.1107/S0021889811038970.

[64] I.-K. Jeong, N. Hur and T. Proffen. 'High-temperature structural evolution of hexagonal multiferroic $YMnO_3$ and $YbMnO_3$'. In: *Journal of Applied Crystallography* 40 (2007), pp. 730–734. DOI: https://doi.org/10.1107/S0021889807025101.

[65] K. Persson. *Materials Data on $ErMnO_3$ (SG:185) by Materials Project.* United States, 2015. DOI: 10.17188/1194080.

[66] S. Artyukhin et al. 'Landau theory of topological defects in multiferroic hexagonal manganites'. In: *Nature Materials* 13.1 (2013), pp. 42–49. DOI: 10.1038/nmat3786.

[67] T. Jungk et al. 'Electrostatic topology of ferroelectric domains in $YMnO_3$'. In: *Applied Physics Letters* 97.1 (2010), pp. 1–4. DOI: 10.1063/1.3460286.

[68] I. G. Ismailzade and S. A. Kizhaev. 'Determination of the Curie Point of the ferroelectrics $YMnO_3$ and $YbMnO_3$'. In: *Soviet Physics-Solid State* 7.1 (1965), pp. 236–238.

[69] K. Lukaszewicz and J. Karut-Kalicinska. 'X-Ray Investigations of the Crystal Structure and Phase Transitions of $YMnO_3$'. In: *Ferroelectrics* 7.1 (1974), pp. 81–82. DOI: 10.1080/00150197408237954.

[70] C. J. Fennie and K. M. Rabe. 'Ferroelectric transition in $YMnO_3$ from first principles'. In: *Physical Review B - Condensed Matter and Materials Physics* 72.10 (2005), pp. 1–4. DOI: 10.1103/PhysRevB.72.100103.

[71] T. S. Holstad. 'Emergent nanoscale functionality in uniaxial ferroelectrics'. PhD thesis. Norwegian Univeristy of Science and Technology, 2020.

[72] J. Schaab. 'Electronic transport and correlation phenomena at improper ferroelectric domain walls'. PhD thesis. University of Stuttgart, 2017.

[73] A. Umantsev. 'Landau Theory of Phase Transitions'. In: *Field Theoretic Method in Phase Transformations.* New York: Springer, 2012. Chap. 2, pp. 7–35. ISBN: 978-1-4614-1487-2. DOI: https://doi.org/10.1007/978-1-4614-1487-2{_}2.

[74] D. Karpov et al. 'Nanoscale topological defects and improper ferroelectric domains in multiferroic barium hexaferrite nanocrystals'. In: *Physical Review B* 100.5 (2019). DOI: 10.1103/PhysRevB.100.054432.

[75] F. Xue et al. ‘Strain-induced incommensurate phases in hexagonal manganites’. In: *Physical Review B* 96.10 (2017). DOI: 10.1103/PhysRevB.96.104109.

[76] Y. Kumagai and N. A. Spaldin. ‘Structural domain walls in polar hexagonal manganites’. In: *Nature Communications* 4 (2013), pp. 1–8. DOI: 10.1038/ncomms2545.

[77] S. C. Chae et al. ‘Evolution of the domain topology in a ferroelectric’. In: *Physical Review Letters* 110.16 (2013), pp. 1–5. DOI: 10.1103/PhysRevLett.110.167601.

[78] Y. Yu et al. ‘Atomic-scale study of topological vortex-like domain pattern in multiferroic hexagonal manganites’. In: *Applied Physics Letters* 103.3 (2013). DOI: 10.1063/1.4813755.

[79] S. C. Chae et al. ‘Self-organization, condensation, and annihilation of topological vortices and antivortices in a multiferroic’. In: *Proceedings of the National Academy of Sciences of the United States of America* 107.50 (2010), pp. 21366–21370. DOI: 10.1073/pnas.1011380107.

[80] M. G. Han et al. ‘Ferroelectric switching dynamics of topological vortex domains in a hexagonal manganite’. In: *Advanced Materials* 25.17 (2013), pp. 2415–2421. DOI: 10.1002/adma.201204766.

[81] Q. H. Zhang et al. ‘Topology breaking of the vortex in multiferroic $\mathrm{Y_0 \cdot 67\, Lu_0 \cdot 33\, MnO_3}$’. In: *Applied Physics Letters* 105.1 (2014). DOI: 10.1063/1.4887057.

[82] Y. L. Li et al. ‘Effect of electrical boundary conditions on ferroelectric domain structures in thin films’. In: *Applied Physics Letters* 81.3 (2002), pp. 427–429. DOI: 10.1063/1.1492025.

[83] J. X. Zhang and L. Q. Chen. ‘Phase-field model for ferromagnetic shape-memory alloys’. In: *Philosophical Magazine Letters* 85.10 (2005), pp. 533–541. DOI: 10.1080/09500830500385527.

[84] X. Shi, H. Huang and X. Wang. ‘Phase-field simulation of strain-induced ferroelectric domain evolution in hexagonal manganites’. In: *Journal of Alloys and Compounds* 719 (2017), pp. 455–459. DOI: 10.1016/j.jallcom.2017.05.212.

[85] J. Y. Park et al. ‘Sensing current and forces with SPM’. In: *Materials Today* 13.10 (2010), pp. 38–45. DOI: 10.1016/S1369-7021(10)70185-1.

[86] G. Binning et al. ‘Surface Studies by Scanning Tunneling Microscopy’. In: *Search of Excellence* 49.1 (1982), pp. 57–61. DOI: 10.1103/PhysRevLett.49.57.

[87] G. Binning, C. F. Quate and C. Gerber. ‘Atomic Force Microscope’. In: *Physical Review Letters* 56.9 (1986). DOI: https://doi.org/10.1103/PhysRevLett.56.930.

[88] K. Bian et al. ‘Scanning probe microscopes’. In: *Nature Reviews Methods Primers* 148.1 (2021), pp. 33–34. DOI: https://doi.org/10.1038/s43586-021-00033-2.

[89] P. Güthner and K. Dransfeld. ‘Local poling of ferroelectric polymers by scanning force microscopy’. In: *Applied Physics Letters* 61.9 (1992), pp. 1137–1139. DOI: 10.1063/1.107693.

[90] D. Denning, J. Guyonnet and B. J. Rodriguez. ‘Applications of piezoresponse force microscopy in materials research: From inorganic ferroelectrics to biopiezoelectrics and beyond’. In: *International Materials Reviews* 61.1 (2016), pp. 46–70. DOI: 10.1179/1743280415Y.0000000013.

[91] A. Gruverman, M. Alexe and D. Meier. ‘Piezoresponse force microscopy and nanoferroic phenomena’. In: *Nature Communications* 10.1 (2019), pp. 1–9. DOI: 10.1038/s41467-019-09650-8.

[92] F. Johann et al. ‘Depth resolution of piezoresponse force microscopy’. In: *Applied Physics Letters* 94.17 (2009). DOI: 10.1063/1.3126490.

[93] K. Yamanaka and S. Nakano. ‘Quantitative elasticity evaluation by contact resonance in an atomic force microscope’. In: *Applied Physics A: Materials Science and Processing* 66 (1998), pp. 313–317. DOI: 10.1007/s003390051153.

[94] S. Jesse, B. Mirman and S. V. Kalinin. ‘Resonance enhancement in piezoresponse force microscopy: Mapping electromechanical activity, contact stiffness, and Q factor’. In: *Applied Physics Letters* 89.2 (2006). DOI: 10.1063/1.2221496.

[95] S. Jesse, A. P. Baddorf and S. V. Kalinin. ‘Switching spectroscopy piezoresponse force microscopy of ferroelectric materials’. In: *Applied Physics Letters* 88.6 (2006), pp. 1–4. DOI: 10.1063/1.2172216.

[96] F. Johann, Á. Hoffmann and E. Soergel. ‘Impact of electrostatic forces in contact-mode scanning force microscopy’. In: *Physical Review B - Condensed Matter and Materials Physics* 81.9 (2010), pp. 1–8. DOI: 10.1103/PhysRevB.81.094109.

[97] S. Hong et al. ‘Principle of ferroelectric domain imaging using atomic force microscope’. In: *Journal of Applied Physics* 89.2 (2001), pp. 1377–1386. DOI: 10.1063/1.1331654.

[98] Y. H. Chen et al. ‘A Dictionary Approach to Electron Backscatter Diffraction Indexing’. In: *Microscopy and Microanalysis* 21.3 (2015), pp. 739–752. DOI: 10.1017/S1431927615000756.

[99] A. D. Herron et al. ‘Simulation of kinematic Kikuchi diffraction patterns from atomistic structures’. In: *MethodsX* 5 (2018), pp. 1187–1203. DOI: 10.1016/j.mex.2018.09.001.

[100] *MATLAB version 9.10.0.1613233 (R2021a)*. The Mathworks, Inc. Natick, Massachusetts, 2021.

[101] F. Bachmann, R. Hielscher and H. Schaeben. ‘Grain detection from 2d and 3d EBSD data-Specification of the MTEX algorithm’. In: *Ultramicroscopy* 111.12 (2011), pp. 1720–1733. DOI: 10.1016/j.ultramic.2011.08.002.

[102] B. Fu and W. Huebner. ‘Synthesis and properties of strontium-doped yttrium manganite’. In: *Journal of Materials Research* 9.10 (1994), pp. 2645–2653. DOI: https://doi.org/10.1557/JMR.1994.2645.

[103] C. Moure et al. ‘Non-Ohmic Behaviour and Switching Phenomena in $YMnO_3$ -Based Ceramic Materials’. In: *Journal of the European Ceramic Society* 19.1 (1999), pp. 131–137. DOI: https://doi.org/10.1016/S0955-2219(98)00180-0.

[104] J. Pelleg. *Creep in ceramics*. Vol. 241. Cham: Springer Nature, 2017, pp. 3–432. ISBN: 978-3-319-50825-2. DOI: 10.1007/978-3-319-50826-9.

[105] H. J. Bunge. 'Textures in ceramics'. In: *Glass and Ceramics* 24 (1995), pp. 1–12. DOI: 10.1155/TSM.24.1.

[106] J. I. Roscow, Y. Li and D. A. Hall. 'Residual stress and domain switching in freeze cast porous barium titanate'. In: *Journal of the European Ceramic Society* 42.4 (2022), pp. 1434–1444. DOI: 10.1016/j.jeurceramsoc.2021.11.046.

[107] R. C. Pohanka, R. W. Rice and B. E. Walker. 'Effect of Internal Stress on the Strength of $BaTiO_3$'. In: *Journal of The American Ceramic Society* 59 (1976), pp. 71–74. DOI: https://doi.org/10.1111/j.1151-2916.1976.tb09394.x.

[108] J. Schultheiß, J. I. Roscow and J. Koruza. 'Orienting anisometric pores in ferroelectrics: Piezoelectric property engineering through local electric field distributions'. In: *Physical Review Materials* 3.8 (2019), pp. 1–13. DOI: 10.1103/PhysRevMaterials.3.084408.

[109] F. Pedregosa et al. 'Scikit-learn: Machine Learning in Python'. In: *Journal of Machine Learning Research* 12 (2011), pp. 2825–2830.

[110] E. G. Fesenko et al. 'Some specific features of hot-pressed ferroelectric piezoelectric ceramics'. In: *Ferroelectrics* 41.1 (1982), pp. 133–136. DOI: 10.1080/00150198208210615.

[111] A. Ruff et al. 'Frequency dependent polarisation switching in h-$ErMnO_3$'. In: *Applied Physics Letters* 112.18 (2018). DOI: 10.1063/1.5026732.

[112] Clive A. Randall et al. 'Intrinsic and extrinsic size effects in fine-grained morphotropic-phase-boundary lead zirconate titanate ceramics'. In: *Journal of the American Ceramic Society* 81.3 (1998), pp. 677–688. ISSN: 00027820. DOI: 10.1111/j.1151-2916.1998.tb02389.x.

[113] H. Miao et al. 'More ferroelectrics discovered by switching spectroscopy piezoresponse force microscopy?' In: *Epl* 108.2 (2014). DOI: 10.1209/0295-5075/108/27010.

[114] Y. Kim et al. 'Nonlinear phenomena in multiferroic nanocapacitors: Joule heating and electromechanical effects'. In: *ACS Nano* 5.11 (2011), pp. 9104–9112. DOI: 10.1021/nn203342v.

[115] H. Qiao et al. 'Electrostatic contribution to hysteresis loop in piezoresponse force microscopy'. In: *Applied Physics Letters* 114.15 (2019). DOI: 10.1063/1.5090591.

[116] MTEX. *Defining Rotations*. URL: https://mtex-toolbox.github.io/RotationDefinition.html.

[117] M. Poirier and F. Laliberté. 'Magnetoelastic coupling in hexagonal multiferroic $YMnO_3$ using ultrasound measurements'. In: *Physical Review B - Condensed Matter and Materials Physics* 76.17 (2007), pp. 1–6. DOI: 10.1103/PhysRevB.76.174426.

[118] X. Zeng et al. 'Pressure effect on elastic constants and related properties of Ti_3Al intermetallic compound: A first-principles study'. In: *Materials* 11.10 (2018). DOI: 10.3390/ma11102015.

[119] M. C. Sekhar et al. ‘Elastic behavior of $YMnO_3$ and $ErMnO_3$ manganites’. In: *Modern Physics Letters B* 17.20-21 (2003), pp. 1119–1125. DOI: 10.1142/s0217984903006025.

Appendices

Appendix A

Vertical piezoresponse PFM images

The PFM scan obtains information on the lateral and vertical piezoresponse. These images are similar, but the contrast of different domains can vary greatly. The vertical piezoresponse PFM images of the in-plane face are shown in Figure A.0.1, while the images of the vertical face are shown in Figure A.0.2.

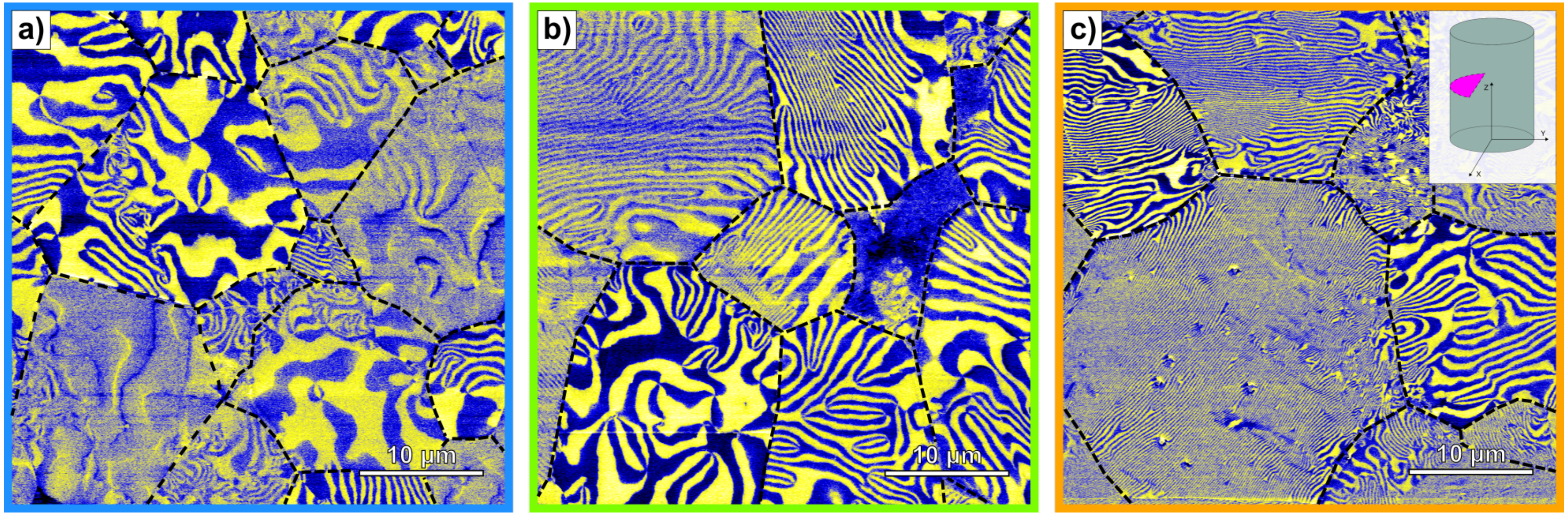

Figure A.0.1: Vertical PFM images of the in-plane samples annealed under different pressures: a) 0 MPa, b) 24 MPa, and c) 47 MPa. The images show the out-of-plane/vertical piezoresponse of the xy-plane. The imaged plane is indicated in the inset of c). Grains are indicated with dashed lines.

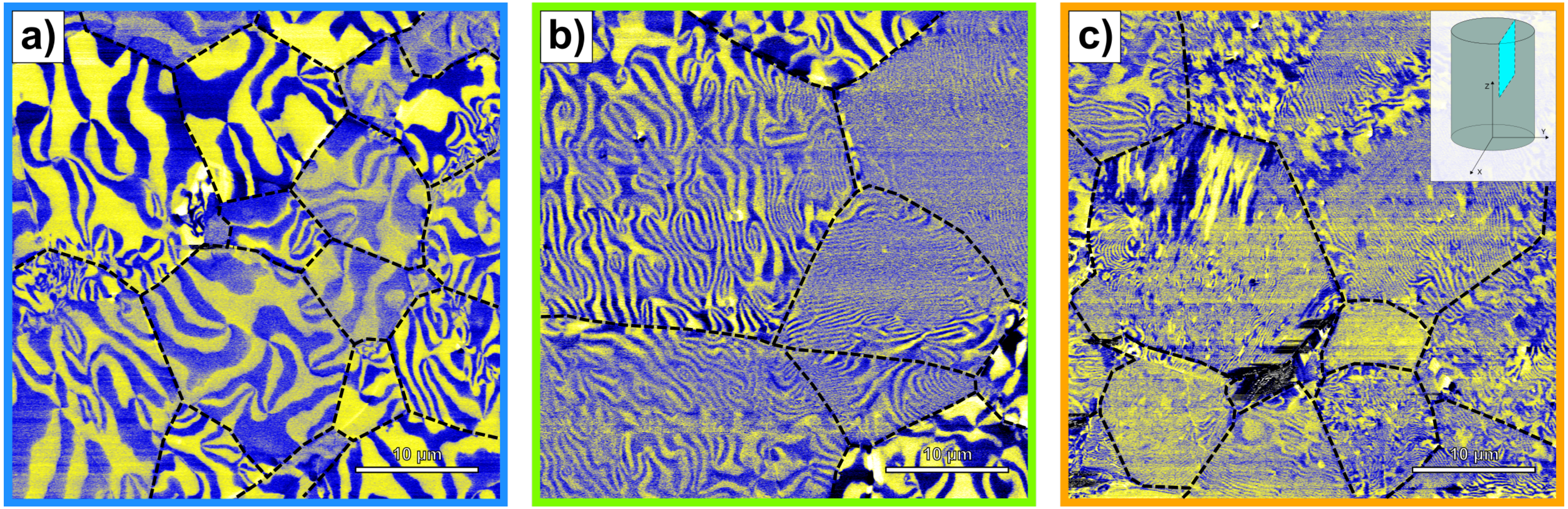

Figure A.0.2: Vertical PFM images of the out-of-plane samples annealed under different pressures: a) 0 MPa, b) 24 MPa, and c) 47 MPa. The images show the out-of-plane/vertical piezoresponse of the xz-plane. The imaged plane is indicated in the inset of c). Grains are indicated with dashed lines.

Appendix B

Interesting PFM images

This appendix shows some interesting PFM images that were not included in the results chapter of the thesis. Figure B.0.1 shows two candidates for 4-state and 8-state vortices discussed in section 2.4.

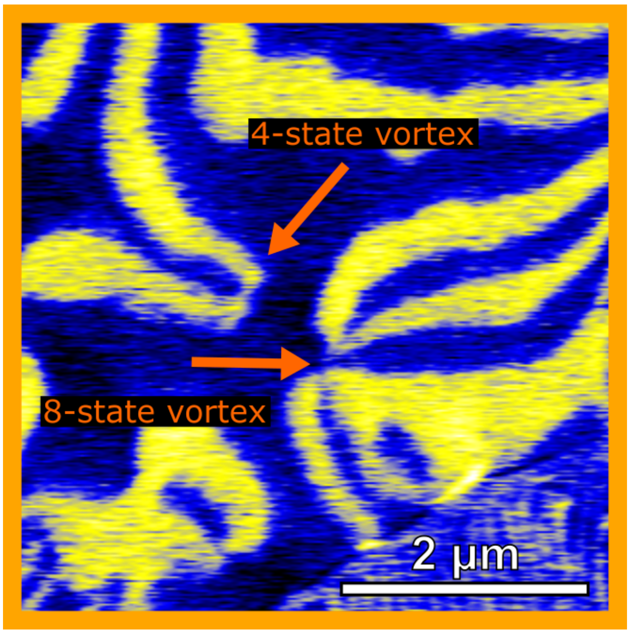

Figure B.0.1: Examples of 4-state and 8-state vortices observed in the 47 MPa sample.

Some other interesting domain structures are presented in the following figures. Figure B.0.2 shows what is sometimes referred to as a bubble domain, while Figure B.0.3 shows a ferroelectric swirl in the different channels.

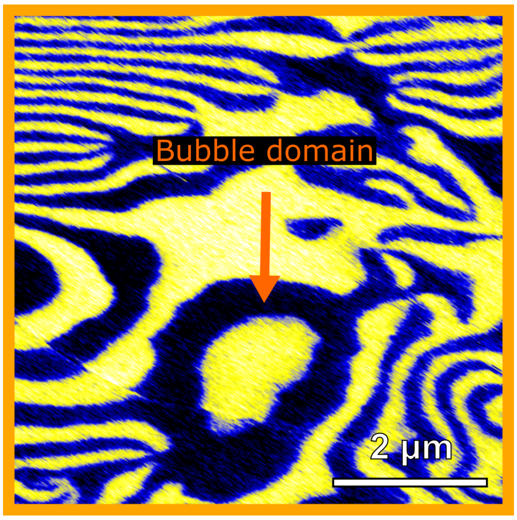

Figure B.0.2: Bubble domain seen in the 47 MPa sample.

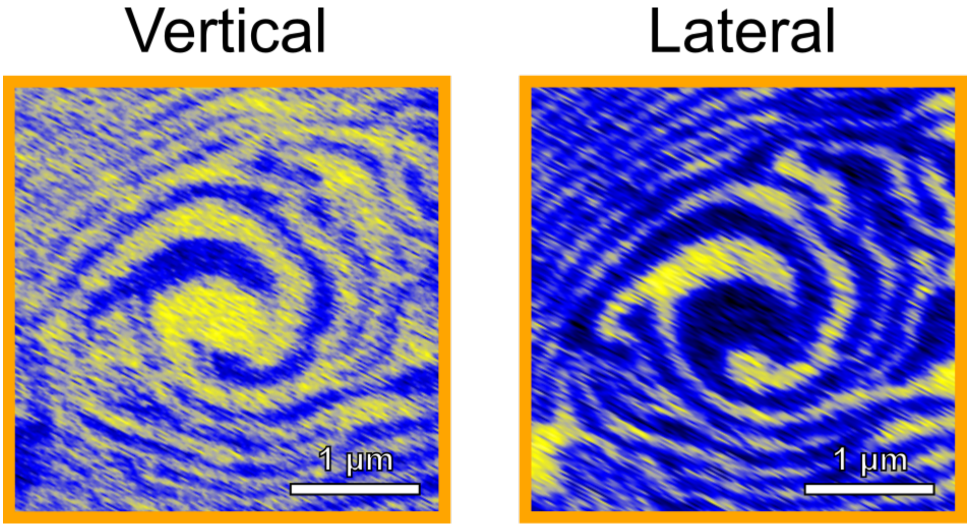

Figure B.0.3: Piezoresponse difference in swirling domains in the 47 MPa sample.

Appendix C

Grain orientation and strain program

The orientations of the grains calculated in the EBSD are given by intrinsic Bunge Euler angles [116]. That is, the orientation of a grain is given by the three angles ϕ_1, ψ, and ϕ_2. The first angle ϕ_1 is the angle of rotation around the original z-axis of the grain. As the grain rotates, the local coordinate system of the grain changes from the global x, y, z system to x', y', z'. The second angle, ψ, is then the angle of rotation around the new x-axis, x'. Again, the local coordinate system changes and becomes x'', y'', z''. The third angle, ϕ_2, is the rotation angle around the new local z-axis, z''.

The program takes in the three orientation angles of the grain, ϕ_1, ψ, and ϕ_2 and stores them. Then three rotation matrices are defined:

$$\boldsymbol{a} = \begin{bmatrix} \cos\phi_1 & -\sin\phi_1 & 0 \\ \sin\phi_1 & \cos\phi_1 & 0 \\ 0 & 0 & 1 \end{bmatrix} \tag{C.1}$$

$$\boldsymbol{b} = \begin{bmatrix} 1 & 0 & 0 \\ 0 & \cos\psi & -\sin\psi \\ 0 & \sin\psi & \cos\psi \end{bmatrix} \tag{C.2}$$

$$\boldsymbol{c} = \begin{bmatrix} \cos\phi_2 & -\sin\phi_2 & 0 \\ \sin\phi_2 & \cos\phi_2 & 0 \\ 0 & 0 & 1 \end{bmatrix} \tag{C.3}$$

Then a full rotation matrix for extrinsic rotation of the grain is made, by multiplying the matrices together in reverse. This enables the conversion from intrinsic to extrinsic rotation due to the following relationship:

$$\boldsymbol{a'} \times \boldsymbol{b'} \times \boldsymbol{c'} = \boldsymbol{c} \times \boldsymbol{b} \times \boldsymbol{a} \tag{C.4}$$

where, the left-hand side matrices represent intrinsic rotation and the right-hand side matrices extrinsic rotations. Thus the complete extrinsic rotation matrix is defined thus:

$$\boldsymbol{X} = \boldsymbol{c} \times \boldsymbol{b} \times \boldsymbol{a} \tag{C.5}$$

Then the applied stresses are inserted into the stress matrix. In our case, the only value inserted was the σ_y corresponding to the uniaxially applied pressure in the y-direction of the out-of-plane face. The stress matrix is shown below:

$$\boldsymbol{\sigma} = \begin{bmatrix} \sigma_x & \tau_{xy} & \tau_{xz} \\ \tau_{xy} & \sigma_y & \tau_{yz} \\ \tau_{xy} & \tau_{yz} & \sigma_z \end{bmatrix} \tag{C.6}$$

Then the local stress experienced by the rotated crystal is calculated by multiplying the stress applied in the global coordinate system with the rotation matrix:

$$\boldsymbol{\sigma'} = \boldsymbol{X} \times \boldsymbol{\sigma} \times \boldsymbol{X^T} \tag{C.7}$$

Then the elastic constant matrix is defined as follows:

$$\boldsymbol{C} = \begin{bmatrix} C_1 & C_2 & C_3 & 0 & 0 & 0 \\ C_2 & C_1 & C_3 & 0 & 0 & 0 \\ C_3 & C_3 & C_4 & 0 & 0 & 0 \\ 0 & 0 & 0 & C_5 & 0 & 0 \\ 0 & 0 & 0 & 0 & C_5 & 0 \\ 0 & 0 & 0 & 0 & 0 & C_6 \end{bmatrix} \tag{C.8}$$

The constants were acquired as described in section C.1.

Using the local stress matrix, $\boldsymbol{\sigma'}$, a tensor is made:

$$\boldsymbol{\sigma} = \begin{bmatrix} \sigma_x \\ \sigma_y \\ \sigma_z \\ \tau_{xy} \\ \tau_{xz} \\ \tau_{yz} \end{bmatrix} \tag{C.9}$$

Then the local strain in the crystal with the given orientation is calculated by multiplying the inverse constants matrix with the stress tensor:

$$\boldsymbol{\varepsilon} = \boldsymbol{C^{-1}} \times \boldsymbol{\sigma} \tag{C.10}$$

C.1 Acquisition of constants

From the article by Poirier et al. [117] four of the constants, C_1 =185 GPa, C_4 =298 GPa, C_5 =98.6 GPa and C_6 =59.4 GPa for $YMnO_3$ at 4 K were acquired. The remaining constants were found with certain assumptions. The first assumption was that interatomic forces are central if ions are at centers of symmetry, and the crystal is stress free. With this assumption the following relation holds:

$$C_2 = C_1 - 2 \cdot C_6 \tag{C.11}$$

This gave the result C_2 =6.62 GPa.

To find the last constant, C_3, the Voigt-Reuss-Hill approximation[118] was used. By using the elastic modulus, E =10.89 GPa [119] and the shear modulus, G =4.67 GPa [119], the bulk modulus, B, of polycrystalline $YMnO_3$ could be approximated by the following expression by solving for B:

$$E = \frac{9BG}{3B + G} \tag{C.12}$$

Then the three following expressions were combined and solved for C_3:

$$B = \frac{B_V + B_R}{2} \tag{C.13}$$

$$B_V = \frac{2C_1 + 2C_2 + 4C_3 + C_4}{9} \tag{C.14}$$

$$B_R = \frac{(C_1 + C_2)C_4 - 2C_3^2}{C_1 + C_2 - 4C_3 + 2C_4} \tag{C.15}$$

The result of the lengthy calculation was that C_3 could be approximated as 19.99 GPa.

Appendix D

Python code for strain calculations

This appendix presents the Python code used to simulate the strains experienced by the grains at different orientations.

```
#### Script for plotting the strains as the orientation of the
↪  grains change
import numpy as np
from numpy import cos, sin
import matplotlib.pyplot as plt


def Calc_and_plot_strains(sX, sY, sZ, tXY, tXZ, tYZ, phi1, Phi,
↪  phi2, iAng, degrees):
    super_strain = [[], [], [], [], [], []]
    for i in range(degrees + 1):
        [phi1_0, Phi_0, phi2_0] = [phi1, Phi, phi2]
        if iAng == 'phi1':
            phi1_0 += i
        elif iAng == 'Phi':
            Phi_0 += i
        else:
            phi2_0 += i
        # Turn angle into radians
        rphi1 = np.deg2rad(phi1_0)    # Rotation around  the z-axis
        rPhi = np.deg2rad(Phi_0)    # Rotation around  the x'-axis
        rphi2 = np.deg2rad(phi2_0)   # Rotation around  the z''-axis
        # z-axis
        a = np.array([[cos(rphi1), -sin(rphi1), 0], [sin(rphi1),
        ↪  cos(rphi1), 0], [0, 0, 1]])
        # x'-axis
        b = np.array([[1, 0, 0], [0, cos(rPhi), -sin(rPhi)], [0,
        ↪  sin(rPhi), cos(rPhi)]])
        # z''-axis
```

```
        c = np.array([[cos(rphi2), -sin(rphi2), 0], [sin(rphi2), cos(rphi2), 0], [0, 0, 1]])

        x = (c @ b) @ a   # The complete rotation matrix
        stress = np.array([[sX, tXY, tXZ], [tXY, sY, tYZ], [tXZ, tYZ, sZ]])    # Stress matrix in global coordinates
        # Calculate the stress matrix for local coordinates
        stress_prime = x @ stress @ np.transpose(x)
        # Make the stress tensor
        stress_tens = np.array([stress_prime[0][0], stress_prime[1][1], stress_prime[2][2],
                       stress_prime[0][1], stress_prime[0][2], stress_prime[1][2]])

        # Calculate the strains from the elastic constants and the stress
        c = [181500, 62700, 199900, 298000, 98600]  # Using MPa
        # Make the elastic constants matrix
        constants = np.array([[c[0], c[1], c[2], 0, 0, 0],
                              [c[1], c[0], c[2], 0, 0, 0],
                              [c[2], c[2], c[3], 0, 0, 0],
                              [0, 0, 0, c[4], 0, 0],
                              [0, 0, 0, 0, c[4], 0],
                              [0, 0, 0, 0, 0, 0.5 * (c[0] - c[1])]])
        # Invert constants matrix
        constants_inv = np.linalg.inv(constants)
        # Multiply inverse matrix and stresses to get strains
        strain = constants_inv @ stress_tens
        # Put the strains for each orientation into the super strain used to plot all the strains
        for i in range(len(strain)):
            super_strain[i].append(strain[i])
    ## Make the data easier to look at by scaling it by 1000
    for i in range(len(super_strain)):
        super_strain[i] = [element * 1000 for element in super_strain[i]]

    ## Make plot
    plt.figure(figsize=(12, 8))
    plt.rc('axes', labelsize=20)  # fontsize of the x and y labels

    # decide what angle to use fo the x-axis of the plot
    subscript = str.maketrans("0123456789", "₀₁₂₃₄₅₆₇₈₉")
    if iAng == 'phi1':
        angle = '\u03C6' + '1'.translate(subscript)
        extra_x = phi1
    elif iAng == 'Phi':
        angle = '\u03A6'
```

```
        extra_x = Phi
    else:
        angle = '\u03C6' + '2'.translate(subscript)
        extra_x = phi2
    dist = degrees + 1
    x = np.array(np.linspace(0, dist - 1, dist))
    for i in range(len(x)):
        x[i] += extra_x
    plt.xlabel(angle)
    y1 = []
    y2 = []
    y3 = []
    y4 = []
    y5 = []
    y6 = []
    # Put the different strains into their own lists
    for j in range(len(super_strain[0])):
        y1.append(super_strain[0][j])
        y2.append(super_strain[1][j])
        y3.append(super_strain[2][j])
        y4.append(super_strain[3][j])
        y5.append(super_strain[4][j])
        y6.append(super_strain[5][j])
    plt.ylabel('strains scaled by 1000')
    L = 2
    plt.plot(x, y1, label='\u03B5xx', lw=L)
    plt.plot(x, y2, label='\u03B5yy', lw=L)
    plt.plot(x, y3, label='\u03B5zz', lw=L)
    plt.plot(x, y4, label='\u03B5xy', lw=L)
    plt.plot(x, y5, ls='--', label='\u03B5xz', lw=L)
    plt.plot(x, y6, ls =':', label='\u03B5yz', lw=L)
    title = 'From: ' + 'phi1:' +  str(phi1) + ' Phi:' + str(Phi) + '
    ↪  phi2:' + str(phi2)
    plt.title(title, fontdict=None, loc='center', pad=None)  # Title
    ↪  of graph
    plt.legend(bbox_to_anchor=(1.085, 1.0), prop={'size': 9})

    name = str(phi1) + '-' + str(Phi) + '-' + str(phi2) + '_' +
    ↪  str(iAng) + '_plot'
    plt.savefig('C:/Users/Olav Sandvik/OneDrive -
    ↪  NTNU/10.semester/Figures/EBSD/Simulations/NewPlots/' + name
    ↪  + '.png', dpi=100,
                pad_inches=1)


def Calc_and_plot_strains_global(sX, sY, sZ, tXY, tXZ, tYZ, phi1,
↪  Phi, phi2, iAng, degrees):
    super_strain = [[], [], [], [], [], []]
```

```
    for i in range(degrees + 1):
        [phi1_0, Phi_0, phi2_0] = [phi1, Phi, phi2]
        if iAng == 'phi1':
            phi1_0 += i
        elif iAng == 'Phi':
            Phi_0 += i
        else:
            phi2_0 += i
        # Turn angle into radians
        rphi1 = np.deg2rad(phi1_0)    # Rotation around  the z-axis
        rPhi = np.deg2rad(Phi_0)    # Rotation around  the x'-axis
        rphi2 = np.deg2rad(phi2_0)   # Rotation around  the z''-axis
        # z-axis
        a = np.array([[cos(rphi1), -sin(rphi1), 0], [sin(rphi1),
        ↪   cos(rphi1), 0], [0, 0, 1]])
        # x'-axis
        b = np.array([[1, 0, 0], [0, cos(rPhi), -sin(rPhi)], [0,
        ↪   sin(rPhi), cos(rPhi)]])
        # z''-axis
        c = np.array([[cos(rphi2), -sin(rphi2), 0], [sin(rphi2),
        ↪   cos(rphi2), 0], [0, 0, 1]])

        x = (c @ b) @ a   # The complete rotation matrix
        stress = np.array([[sX, tXY, tXZ], [tXY, sY, tYZ], [tXZ,
        ↪   tYZ, sZ]])    # Stress matrix in global coordinates
        # Calculate the stress matrix for local coordinates
        stress_prime = x @ stress @ np.transpose(x)
        # Make the stress tensor
        stress_tens = np.array([stress_prime[0][0],
        ↪   stress_prime[1][1], stress_prime[2][2],
                       stress_prime[0][1], stress_prime[0][2],
                        ↪   stress_prime[1][2]])

        # Calculate the strains from the elastic constants and the
        ↪   stress
        c = [181500, 62700, 199900, 298000, 98600]  # Using MPa
        # Make the elastic constants matrix
        constants = np.array([[c[0], c[1], c[2], 0, 0, 0],
                              [c[1], c[0], c[2], 0, 0, 0],
                              [c[2], c[2], c[3], 0, 0, 0],
                              [0, 0, 0, c[4], 0, 0],
                              [0, 0, 0, 0, c[4], 0],
                              [0, 0, 0, 0, 0, 0.5 * (c[0] - c[1])]])
        # Invert constants matrix
        constants_inv = np.linalg.inv(constants)
        # Multiply inverse matrix and stresses to get local strains
        strain = constants_inv @ stress_tens
```

```
    ### Convert the local strain back to global coordinates
    y = np.linalg.inv(x)  # Inverse of x
    # Make a strain matrix of the local strain tensor
    strain_prime_mat = np.array([[strain[0], strain[3],
     ↪  strain[4]], [strain[3], strain[1], strain[5]],
                                 [strain[4], strain[5],
                                  ↪  strain[2]]])  # Local
                                  ↪  strain matrstrain[5
    # Rotate local strain matrix back to global
    global_strain = y @ strain_prime_mat @ np.transpose(y)
    # Make global strain tensor
    global_strain_tens = np.array([global_strain[0][0],
     ↪  global_strain[1][1], global_strain[2][2],
                   global_strain[0][1], global_strain[0][2],
                    ↪  global_strain[1][2]])
    # Put the strains for each orientation into the super strain
     ↪  used to plot all the strains
    for i in range(len(global_strain_tens)):
        super_strain[i].append(global_strain_tens[i])
## Make the data easier to look at by scaling it by 1000
for i in range(len(super_strain)):
    super_strain[i] = [element * 1000 for element in
     ↪  super_strain[i]]
## Make plot
plt.figure(figsize=(12, 8))
plt.rc('axes', labelsize=20)  # fontsize of the x and y labels

# decide what angle to use fo the x-axis of the plot
subscript = str.maketrans("0123456789", "")
if iAng == 'phi1':
    angle = '\u03C6' + '1'.translate(subscript)
    extra_x = phi1
elif iAng == 'Phi':
    angle = '\u03A6'
    extra_x = Phi
else:
    angle = '\u03C6' + '2'.translate(subscript)
    extra_x = phi2
dist = degrees + 1
x = np.array(np.linspace(0, dist - 1, dist))
for i in range(len(x)):
    x[i] += extra_x
plt.xlabel(angle)
y1 = []
y2 = []
y3 = []
y4 = []
```

```
    y5 = []
    y6 = []
    # Put the different strains into their own lists
    for j in range(len(super_strain[0])):
        y1.append(super_strain[0][j])
        y2.append(super_strain[1][j])
        y3.append(super_strain[2][j])
        y4.append(super_strain[3][j])
        y5.append(super_strain[4][j])
        y6.append(super_strain[5][j])
    plt.ylabel('strains scaled by 1000')
    L = 2
    plt.plot(x, y1, label='\u03B5xx', lw=L)
    plt.plot(x, y2, label='\u03B5yy', lw=L)
    plt.plot(x, y3, label='\u03B5zz', lw=L)
    plt.plot(x, y4, label='\u03B5xy', lw=L)
    plt.plot(x, y5, ls='--', label='\u03B5xz', lw=L)
    plt.plot(x, y6, ls =':', label='\u03B5yz', lw=L)
    title = 'Global strains, From: ' + 'phi1:' +  str(phi1) + '
     ↪  Phi:' + str(Phi) + ' phi2:' + str(phi2)
    plt.title(title, fontdict=None, loc='center', pad=None)  #
     ↪  Tittel på graf
    plt.legend(bbox_to_anchor=(1.085, 1.0), prop={'size': 9})

    name = 'Global strains  ' + str(phi1) + '-' + str(Phi) + '-' +
     ↪  str(phi2) + '_' + str(iAng) + '_plot'
    plt.savefig('C:/Users/Olav Sandvik/OneDrive -
     ↪  NTNU/10.semester/Figures/EBSD/Simulations/NewPlots/' + name
     ↪  + '.png', dpi=100,
                pad_inches=1)


def Calc_and_plot_strainsX(sX, sY, sZ, tXY, tXZ, tYZ, phi1, Phi,
 ↪  phi2, iAng, degrees):
    super_strain = [[], [], [], [], [], []]
    for i in range(degrees + 1):
        [phi1_0, Phi_0, phi2_0] = [phi1, Phi, phi2]
        if iAng == 'phi1':
            phi1_0 += i
        elif iAng == 'Phi':
            Phi_0 += i
        else:
            phi2_0 += i
        # Turn angle into radians
        rphi1 = np.deg2rad(phi1_0)    # Rotation around  the z-axis
        rPhi = np.deg2rad(Phi_0)    # Rotation around  the x'-axis
        rphi2 = np.deg2rad(phi2_0)   # Rotation around  the z''-axis
        # z-axis
```

```
    a = np.array([[cos(rphi1), -sin(rphi1), 0], [sin(rphi1),
     ↪  cos(rphi1), 0], [0, 0, 1]])
    # x'-axis
    b = np.array([[1, 0, 0], [0, cos(rPhi), -sin(rPhi)], [0,
     ↪  sin(rPhi), cos(rPhi)]])
    # z''-axis
    c = np.array([[cos(rphi2), -sin(rphi2), 0], [sin(rphi2),
     ↪  cos(rphi2), 0], [0, 0, 1]])

    x = (c @ b) @ a   # The complete rotation matrix
    stress = np.array([[sX, tXY, tXZ], [tXY, sY, tYZ], [tXZ,
     ↪  tYZ, sZ]])    # Stress matrix in global coordinates
    # Calculate the stress matrix for local coordinates
    stress_prime = x @ stress @ np.transpose(x)
    # Make the stress tensor
    stress_tens = np.array([stress_prime[0][0],
     ↪  stress_prime[1][1], stress_prime[2][2],
                   stress_prime[0][1], stress_prime[0][2],
                    ↪  stress_prime[1][2]])

    # Calculate the strains from the elastic constants and the
     ↪  stress
    c = [185000, 66200, 199900, 298000, 98600]  # Using MPa
    # Make the elastic constants matrix
    constants = np.array([[c[0], c[1], c[2], 0, 0, 0],
                          [c[1], c[0], c[2], 0, 0, 0],
                          [c[2], c[2], c[3], 0, 0, 0],
                          [0, 0, 0, c[4], 0, 0],
                          [0, 0, 0, 0, c[4], 0],
                          [0, 0, 0, 0, 0, 0.5 * (c[0] - c[1])]])
    # Invert constants matrix
    constants_inv = np.linalg.inv(constants)
    # Multiply inverse matrix and stresses to get strains
    strain = constants_inv @ stress_tens
    # Put the strains for each orientation into the super strain
     ↪  used to plot all the strains
    for i in range(len(strain)):
        super_strain[i].append(strain[i])
## Make the data easier to look at by scaling it by 1000
for i in range(len(super_strain)):
    super_strain[i] = [element * 1000 for element in
     ↪  super_strain[i]]

## Make plot
plt.figure(figsize=(12, 8))
plt.rc('axes', labelsize=20)  # fontsize of the x and y labels

# decide what angle to use fo the x-axis of the plot
```

```
subscript = str.maketrans("0123456789", "U+2080")
if iAng == 'phi1':
    angle = '\u03C6' + '1'.translate(subscript)
    extra_x = phi1
elif iAng == 'Phi':
    angle = '\u03A6'
    extra_x = Phi
else:
    angle = '\u03C6' + '2'.translate(subscript)
    extra_x = phi2
dist = degrees + 1
x = np.array(np.linspace(0, dist - 1, dist))
for i in range(len(x)):
    x[i] += extra_x
plt.xlabel(angle)
y1 = []
y2 = []
y3 = []
y4 = []
y5 = []
y6 = []
# Put the different strains into their own lists
for j in range(len(super_strain[0])):
    y1.append(super_strain[0][j])
    y2.append(super_strain[1][j])
    y3.append(super_strain[2][j])
    y4.append(super_strain[3][j])
    y5.append(super_strain[4][j])
    y6.append(super_strain[5][j])
plt.ylabel('strains scaled by 1000')
L = 2
plt.plot(x, y1, label='\u03B5xx', lw=L)
plt.plot(x, y2, label='\u03B5yy', lw=L)
plt.plot(x, y3, label='\u03B5zz', lw=L)
plt.plot(x, y4, label='\u03B5xy', lw=L)
plt.plot(x, y5, ls='--', label='\u03B5xz', lw=L)
plt.plot(x, y6, ls =':', label='\u03B5yz', lw=L)
title = 'From: ' + 'phi1:' +  str(phi1) + ' Phi:' + str(Phi) + '
↪   phi2:' + str(phi2)
plt.title(title, fontdict=None, loc='center', pad=None)
#plt.legend(loc='upper left')
plt.legend(bbox_to_anchor=(1.085, 1.0), prop={'size': 9})

name = str(phi1) + '-' + str(Phi) + '-' + str(phi2) + '_' +
↪   str(iAng) + '_plot'

# Calculating the difference between exx and eyy and the
↪   magnitude of exy
```

```
    diff1 = abs(y1[0] - y2[0])
    diff2 = abs(y1[45] - y2[45])
    diff3 = abs(y1[90] - y2[90])
    exy1 = abs(max(y4))
    exy2 = abs(min(y4))
    # If one of the strains is high enough, write the name of the
    ↪   plot and the strains to the text file.
    if diff1 > 0.35 or diff2 > 0.35 or diff3 > 0.35 or exy1 > 0.25
    ↪   or exy2 > 0.25:
    textfile_name = 'All_orientations_with_high_strains.txt'
    with open(textfile_name, 'a') as f:
        f.write(name + 'strains: diff1=' + str(round(diff1,3)) + '
        ↪   diff2=' + str(round(diff2,3)) + '  diff3=' +
        str(round(diff3,3)) + '  maxExy=' + str(round(exy1, 3)) + '
        ↪   minExy=' + str(round(min(y4), 3)) + '\n')
    f.close()
    # If the strains are high, also make the plot and send it to the
    ↪   high strains folder
    plt.savefig(
        'C:/Users/Olav Sandvik/OneDrive -
        ↪   NTNU/10.semester/Figures/EBSD/Simulations/AllSims/' +
        ↪   name + '.png',
        dpi=100, pad_inches=1)
    plt.close()  # Close th figure


def all_calc():
    # This function iterates through all the possible orientations
    ↪   and plots them. It also calculates the exx and eyy
    # and marks the ones with a high difference between exx and eyy.
    angles = ['phi1', 'Phi', 'phi2']
    for angle in angles:
        for i in range(2):
            for j in range(2):
                for k in range(2):
                    Calc_and_plot_strainsX(0, -47, 0, 0, 0, 0,
                    ↪   phi1=90*i, Phi=90*j, phi2=90*k, iAng=angle,
                    ↪   degrees=90)


#### Calculate all possible orientations and find the ones with a
↪   high difference between exx and eyy and a high exy.
all_calc()

# phi1 0.0 - Phi 90.0 - phi2 0.0 (in-plane)
Calc_and_plot_strains(0, -47, 0, 0, 0, 0, phi1=0.0, Phi=90.0,
↪   phi2=0.0, iAng='phi2', degrees=90)
```

```
Calc_and_plot_strains(0, -47, 0, 0, 0, 0, phi1=0.0, Phi=90.0,
↪   phi2=0.0, iAng='Phi', degrees=90)
Calc_and_plot_strains(0, -47, 0, 0, 0, 0, phi1=0.0, Phi=90.0,
↪   phi2=0.0, iAng='phi1', degrees=90)

# phi1 90.0 - Phi 0.0 - phi2 0.0 (out-of-plane)
Calc_and_plot_strains(0, -47, 0, 0, 0, 0, phi1=90.0, Phi=0.0,
↪   phi2=0.0, iAng='phi2', degrees=90)
Calc_and_plot_strains(0, -47, 0, 0, 0, 0, phi1=90.0, Phi=0.0,
↪   phi2=0.0, iAng='Phi', degrees=90)
Calc_and_plot_strains(0, -47, 0, 0, 0, 0, phi1=90.0, Phi=0.0,
↪   phi2=0.0, iAng='phi1', degrees=90)

# phi1 0.0 - Phi 0.0 - phi2 0.0 (out-of-plane)
Calc_and_plot_strains(0, -47, 0, 0, 0, 0, phi1=0.0, Phi=0.0,
↪   phi2=0.0, iAng='phi1', degrees=60)


# phi1 0.0 - Phi 90.0 - phi2 0.0 (in-plane and out-of-plane)
Calc_and_plot_strains(0, -47, 0, 0, 0, 0, phi1=0.0, Phi=135.0,
↪   phi2=0.0, iAng='phi1', degrees=90)


### Compare Global strains and Local strains
Calc_and_plot_strains_global(0, -47, 0, 0, 0, 0, phi1=0.0, Phi=90.0,
↪   phi2=0.0, iAng='phi1', degrees=90)
Calc_and_plot_strains_global(0, -47, 0, 0, 0, 0, phi1=90.0, Phi=0.0,
↪   phi2=0.0, iAng='Phi', degrees=90)
```

Appendix E

Principle component analysis

In order to look for contributions to the behavior observed in the electrical analysis, a principal component analysis with six components was performed. Figure E.0.1 shows the principal components as images. The two first principle components appear to relate to the piezoelectric response due to the ferroelectric domains and the topography, respectively. The other principle components most likely correspond to other things such as noise and dirt.

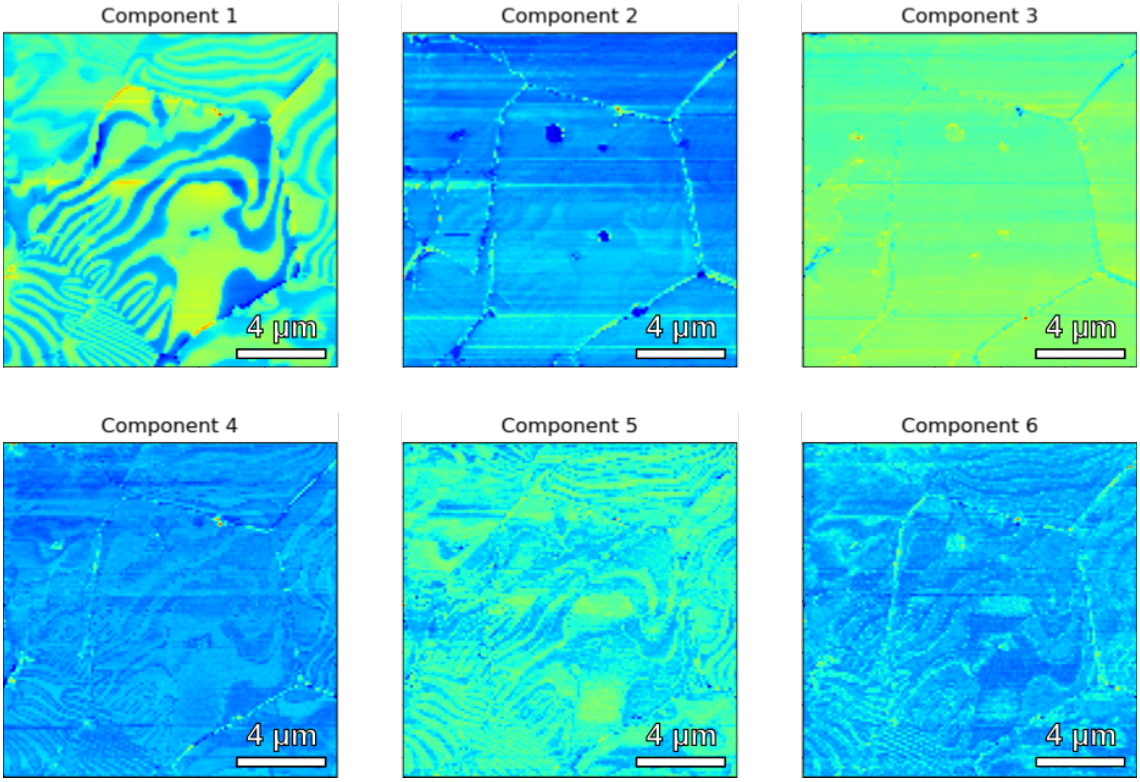

Figure E.0.1: Principle components of the PCA illustrated as images.

Figure E.0.2 shows the piezoresponse of the different components plotted as functions of voltage. The plot of the first component does not resemble anything, and neither does the third to sixth. The second component plot, however, almost looks like a hysteresis curve. This also explains the switching behavior observed previously, and if the interpretation of the components is accurate, then this further supports the lack of switching in the ferroelectric domains.

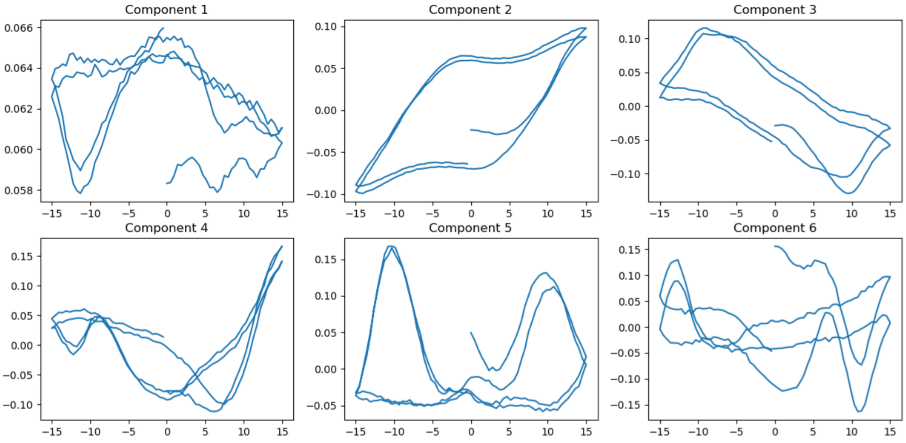

Figure E.0.2: Piezoresponse of principle components from the PCA plotted as functions of voltage.

Figure E.0.3 shows a cumulative and bar plot of the explained variance for the principal components. The bars show the variance in piezoresponse explained by each individual principal component, while the plot shows the cumulative variance explained by the components. The figure shows that the two first components explain about 88% of the variance. The plot also shows that using more than two principal components does not add much to the explained variance. In fact, the returns are quickly diminishing, which means that the other components likely are redundant.

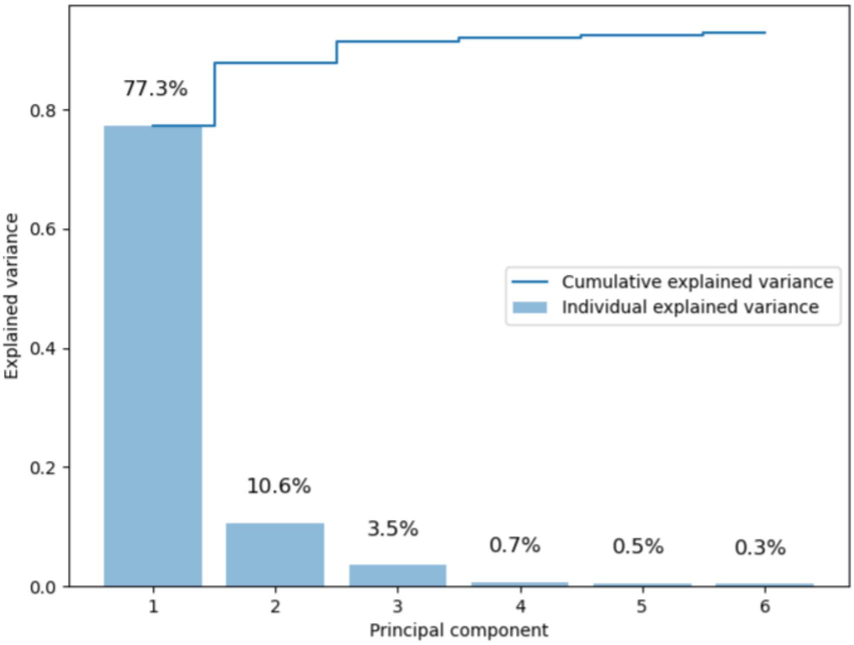

Figure E.0.3: Individual and cumulative variance explained by the principle components from the PCA [109].

Appendix F

Python code used for analysis of electrical measurements

This appendix shows the Python code used to plot and calculate different things regarding the impact of electric fields on the polycrystalline $ErMnO_3$ sample.

```
### Most of this code was heavily inspired by code written by Kyle Kelly, Oak Ridge National Laboratory in Tennessee, United States of America.
import numpy as np
import matplotlib.pyplot as plt
import sidpy as sid
import h5py
import os
from matplotlib.animation import FuncAnimation
import tensorly as tl
from tensorly.decomposition import parafac
from mpl_toolkits.axes_grid1 import make_axes_locatable
from tensorly.decomposition import non_negative_parafac
from tensorly.decomposition import non_negative_tucker
from tensorly.decomposition import robust_pca
from tensorly.decomposition import parafac
from sklearn.decomposition import NMF
from pylab import *
from scipy.optimize import curve_fit
from matplotlib import colors
from scipy.cluster.vq import whiten, kmeans, vq
import scipy
from tensorly import metrics
import torch
from scipy.ndimage.interpolation import rotate
import pycroscopy as px
import gdown
import sklearn as sk
```

```
import matplotlib.gridspec as gridspec
from BGlib import be as belib
from mpl_toolkits.axes_grid1 import AxesGrid
import pickle
import matplotlib.colors


def correct_phase_wrapping(plot_data):
    min_ = np.min(data['Phase'])
    max_ = np.max(data['Phase'])
    data2_phacor = np.where(data['Phase'] > 1.5, data['Phase'] +
     ↪  (min_ - max_), data['Phase'])
    data2_phacor = data2_phacor + np.pi + 0.22

    if plot_data == 'yes':
        plt.figure()
        plt.hist(data['Phase'].ravel(), bins=100)
        plt.figure()
        plt.hist(data2_phacor.ravel(),bins = 100)
        plt.axvline(np.pi, color ='red')
        plt.axvline(0, color ='red')
        plt.show()
    return data2_phacor


def reshape_n_average_off_field_data(data):
    data = data[:, 1::2]  # Focusing on the off-field data
    data = data.reshape(128, 128, 2, 128)  # Reshape the data
    data = data.mean(axis=2)  # Take average of the two measurements
    return data


def reshape_n_average_on_field_data(data):
    data = data[:, 0::2]  # Focusing on the on-field data
    data = data.reshape(128, 128, 2, 128)  # Reshape the data
    data = data.mean(axis=2)  # Take average of the two measurements
    return data

# Downloading data
 gdown.download("https://drive.google.com/uc?export=download&confirm⌋
 ↪  =01Ff&id=1ZzvfYf4i7-dZuIjiJ7DrbTsCbCUy7huT")
 gdown.download("https://drive.google.com/uc?export=download&confirm⌋
 ↪  =01Ff&id=1Wk77f2Waq2eklbU4fzI_Oz5npLdNnO_q")
 gdown.download("https://drive.google.com/uc?export=download&confirm⌋
 ↪  =01Ff&id=1Dt3o1c_3FZ5OqhVn5XMMUpZxXYFPPVkq")
 gdown.download("https://drive.google.com/uc?export=download&confirm⌋
 ↪  =01Ff&id=1EuhUYTvcZIfJpRioayTCXbSePJDKM_rl")
```

```
 gdown.download("https://drive.google.com/uc?export=download&confirm⌋
  ↪  =0lFf&id=1obVNDuG2ASOCZ8iTSRXpabc5eqSpzdGc")
 gdown.download("https://drive.google.com/uc?export=download&confirm⌋
  ↪  =0lFf&id=1E3qS1M1knFnpvcQC_LYHscoW1SZetfTR")
 gdown.download("https://drive.google.com/uc?export=download&confirm⌋
  ↪  =0lFf&id=1ntHtxnZEZQYgC7ia2_MOTSEOzKtW3Lqg")


### Extract data from file and then pickle relevant data ###
 data = extract_BEPS_data('EMO_15um_HighDensityGrid_0043.h5',
  ↪  phase_offset = 0, DeflInvOLS = 1)
 datadict = {'Amplitude' : data['Amplitude'], 'Phase' :
  ↪  data['Phase'], 'BEPS_Voltage' : np.array(data['BEPS_Voltage'])}
 pickle.dump(datadict, open('extracted_data.pck', 'wb'))

data = pickle.load(open('extracted_data.pck', 'rb'))


### Phase wrapping corrected ###
data2_phacor = correct_phase_wrapping('no plot')

### Focus on relevant data ###
pr_off_avg = reshape_n_average_off_field_data(data['Amplitude']*np.c⌋
 ↪  os(data2_phacor))  # Average of off-field data for
 ↪  piezoresponse
pr_on_avg = reshape_n_average_on_field_data(data['Amplitude']*np.cos⌋
 ↪  (data2_phacor))     # On-field
 ↪  data
amp_data = reshape_n_average_off_field_data(data['Amplitude'])  #
 ↪  Average of off-field data for amplitude
amp_data2 = reshape_n_average_on_field_data(data['Amplitude'])  #
 ↪  Average of on-field data for amplitude
phase_data = reshape_n_average_off_field_data(data2_phacor)  #
 ↪  Average of off-field data for phase
phase_data2 = reshape_n_average_off_field_data(data2_phacor)  #
 ↪  Average of on-field data for phase
data2_pr = data['Amplitude']*np.cos(data2_phacor)  # Piezoresponse
 ↪  array
data2_pr_off = data2_pr[:, 1::2]    # Off-field data of
 ↪  piezoresponse array


def plot_voltage_as_a_function_of_indices(plott):
    indices = linspace(0, 127, 128)
    for i in range(len(indices)):
        indices[i] = int(indices[i])
    voltages = data['BEPS_Voltage'][0, 1:256:2]
    volt = []
```

```
    for i in range(len(voltages)):
        volt.append(voltages[i])
    voltages = volt
    if plott == 'yes':
        plot(indices, voltages, 'index', 'voltage', 'Voltage as a
         ↪  function of indices')
    return voltages


def plot_difference_between_images(data,  cut, im_indices):
    voltages = plot_voltage_as_a_function_of_indices('no')
    fig = plt.figure(figsize=(8, 6))
    gs = gridspec.GridSpec(10, 10 + 5, wspace=0.01, hspace=0.1)
    minMax= []
    factor = 100000
    for j in range(2):
        minMax.append(factor * min(np.array(data[:, :,
         ↪  im_indices[j]]).flatten()))
        minMax.append(factor * max(np.array(data[:, :,
         ↪  im_indices[j]]).flatten()))
    norm = Normalize(vmin=cut[0]*min(minMax),
     ↪  vmax=cut[1]*max(minMax))

    # Image showing the difference
    ax = fig.add_subplot(gs[:, :10])
    ax.set_axis_off()
    difference = (factor * data[:, :, im_indices[0]]) - (factor *
     ↪  data[:, :, im_indices[1]])
    im = ax.imshow(difference, norm = norm, cmap='viridis')
    axx = plt.subplot(gs[:, -1:])  # The axis for the color bar
    cbar_ax = fig.add_axes(axx)
    fig.colorbar(cm.ScalarMappable(norm=norm, cmap='viridis'),
     ↪  cax=cbar_ax, extend='both')
    fig.savefig('C:/Users/Olav Sandvik/OneDrive -
     ↪  NTNU/10.semester/Figures/OakRidge/Difference3', dpi=100,
                pad_inches=1)


def avg_cluster_resp(clusters, clx, data1_, pr_cluster, color, name):
    clusters_list = []
    for j in range(clusters):   # Make a list for each cluster
        clusters_list.append([])
    for j in range(clx.shape[0]):   # Add data to lists
        if clx[j] == 0:
            clusters_list[0].append(data1_[j, :])
        elif clx[j] == 1:
            clusters_list[1].append(data1_[j, :])
        elif clx[j] == 2:
```

```
            clusters_list[2].append(data1_[j, :])
        elif clx[j] == 3:
            clusters_list[3].append(data1_[j, :])
        elif clx[j] == 4:
            clusters_list[4].append(data1_[j, :])
        elif clx[j] == 5:
            clusters_list[5].append(data1_[j, :])
        elif clx[j] == 6:
            clusters_list[6].append(data1_[j, :])
        elif clx[j] == 7:
            clusters_list[7].append(data1_[j, :])
    mean_clust = []
    for j in range(clusters):
        mean_clust.append([])
    for j in range(clusters):
        mean_clust[j] = np.mean(clusters_list[j], axis=0)

    cols = clusters
    rows = 1
    plt.rc('xtick', labelsize=20)  # fontsize of the tick labels
    plt.rc('ytick', labelsize=25)  # fontsize of the tick labels
    fig, ax = plt.subplots(rows, cols, figsize=(5*(clusters), 8),
     ↪  sharey = True)
    for j in range(clusters):
        ax[j].plot(data['BEPS_Voltage'][0, ::2], mean_clust[j])
        ax[j].set_xticks([-15, -7.5, 0, 7.5, 15], ['-15', '-7.5',
         ↪  '0', '7.5', '15'])
        ax[j].xaxis.set_tick_params(width=2, length=4)  # Makes the
         ↪  ticks on the x-axis bigger
        ax[j].grid(alpha=0.5)
        ax[j].set_title('Cluster ' + str(j+1))

    plt.tight_layout()
    ax[0].yaxis.set_tick_params(width=3, length=6)
    fig.savefig('C:/Users/Olav Sandvik/OneDrive -
     ↪  NTNU/10.semester/Figures/OakRidge/Clusters/' + str(name) +
     ↪  'means', dpi=150,
                pad_inches=1)


def cluster_analysis(clusters, data, color, name, norm):
    fig, ax = plt.subplots()
    data1_ = tl.tensor(data)
    data1_ = scipy.cluster.vq.whiten(data1_)
    centroids, _ = scipy.cluster.vq.kmeans(data1_, clusters,
     ↪  iter=20, seed=123456)
    clx, _ = vq(data1_, centroids)
    pr_cluster = np.reshape(clx, (128, 128))
```

```
    plt.imshow(pr_cluster, cmap=color, norm=norm)
    plt.colorbar()
    fig.set_size_inches(8, 6)
    plt.tight_layout()
    fig.savefig('C:/Users/Olav Sandvik/OneDrive -
    ↪  NTNU/10.semester/Figures/OakRidge/Clusters/' + str(name),
    ↪  dpi=100,
                pad_inches=1)
    avg_cluster_resp(clusters, clx, data1_, pr_cluster, color, name)


def cluster_analysis_normal(clusters, data, colormap, name, sd):
    fig, ax = plt.subplots()
    data1_ = tl.tensor(data)
    data1_ = scipy.cluster.vq.whiten(data1_)
    centroids, _ = scipy.cluster.vq.kmeans(data1_, clusters,
    ↪  iter=20, seed=sd)
    clx, _ = vq(data1_, centroids)
    pr_cluster = np.reshape(clx, (128, 128))
    plt.imshow(pr_cluster, cmap=colormap)
    plt.colorbar()
    fig.set_size_inches(8, 6)
    plt.tight_layout()
    fig.savefig('C:/Users/Olav Sandvik/OneDrive -
    ↪  NTNU/10.semester/Figures/OakRidge/Clusters/Normal' +
    ↪  str(name) + 'seed_' + str(sd) + '.png', dpi=100,
                pad_inches=1)
    plt.close()
    avg_cluster_resp(clusters, clx, data1_, pr_cluster, color, name)


def hysteresis_of_area(x0, y0, x1, y1, image_data, voltage_data,
↪  name):
    def plot_piezoresponse(dist, color, linex, liney):
        linescan_pr = []
        for u in range(dist):
            linescan_pr.append(pr_off_avg[int(liney[u]),
            ↪  int(linex[u]), :])
        linescan_pr = np.asarray(linescan_pr)
        fig, ax = plt.subplots(1, dist, figsize=(6, 10))
        for v in range(dist):
            # The voltage is the same, but the piezoresponse is
            ↪  different for the different pixels.
            ax[v].plot(data['BEPS_Voltage'][0, 1:256:2],
            ↪  linescan_pr[v, :] * 2E5, color)

    # Get all the point within the square area defined by x0,y0 and
    ↪  x1,y1
```

```
x_dist = x1 - x0
y_dist = y1 - y0
horizontal_lines = []
piz_lines = []  # Piezoresponses of all lines
for j in range(y_dist):
    linex = np.linspace(x0, x1, x_dist)  # Make equally spaced
     ↪  point from x0 to x1
    liney = np.zeros(y_dist)+(y0 + j)    # Make a list of the
     ↪  same y-value for the line
    horizontal_lines.append([linex, liney])
    # Get the piezoresponse for the line
    linescan_pr = []    # The piezoresponse for each pixel of a
     ↪  line
    for u in range(x_dist):
        linescan_pr.append(pr_off_avg[int(liney[u]),
         ↪  int(linex[u]), :])  # Piezoresponse for a pixel at
         ↪  all voltages
    # Get the average piezoresponse for the line
    avg_linescan_pr = np.zeros(128)
    for pixel in range(x_dist):
        for pr in range(128):
            avg_linescan_pr[pr] += linescan_pr[pixel][pr]
    for q in range(128):
        avg_linescan_pr[q] = avg_linescan_pr[q]/x_dist
    piz_lines.append(avg_linescan_pr)  # Add the average
     ↪  responses from each line to the greater list

# Average the response from all the lines
avg_resp = np.zeros(128)
for line in range(y_dist):
    for val in range(128):
        avg_resp[val] += piz_lines[line][val]
for t in range(128):
    avg_resp[t] = avg_resp[t]/y_dist

data = voltage_data
plt.rc('axes', labelsize=20)  # fontsize of the x and y labels
plt.rc('xtick', labelsize=25)  # fontsize of the tick labels
plt.rc('ytick', labelsize=25)  # fontsize of the tick labels
fig, ax = plt.subplots(1, 2, figsize=(14, 6))
ax[0].imshow(image_data.reshape(128, 128, 512)[:, :, 0])
#plt.colorbar()
LW = 5
for i in range(len(horizontal_lines)):
    ax[0].plot(horizontal_lines[i][0], horizontal_lines[i][1],
     ↪  color='red', linewidth= LW)
# Plot the average piezoresponse for the area
ax[1].plot(data['BEPS_Voltage'][0, 1:256:2], avg_resp * 2E5)
```

```
    fig.tight_layout()
    fig.savefig('C:/Users/Olav Sandvik/OneDrive -
     ↪  NTNU/10.semester/Figures/OakRidge/PiezoArea' + str(name),
     ↪  dpi=100,
                pad_inches=1)
    return avg_resp


def hysteresis_of_2_area(x0, y0, x1, y1, x2, y2, x3, y3, image_data,
 ↪  voltage_data, name):
    def plot_piezoresponse(dist, color, linex, liney):
        linescan_pr = []
        for u in range(dist):
            linescan_pr.append(pr_off_avg[int(liney[u]),
             ↪  int(linex[u]), :])
        linescan_pr = np.asarray(linescan_pr)
        fig, ax = plt.subplots(1, dist, figsize=(6, 10))
        for v in range(dist):
            # The voltage is the same, but the piezoresponse is
             ↪  different for the different pixels.
            ax[v].plot(data['BEPS_Voltage'][0, 1:256:2],
             ↪  linescan_pr[v, :] * 2E5, color)

    # Get all the point within the square area defined by x0,y0 and
     ↪  x1,y1
    x_dist = x1 - x0
    y_dist = y1 - y0
    x_dist2 = x3 - x2
    y_dist2 = y3 - y2
    horizontal_lines = []
    horizontal_lines2 = []
    piz_lines = []  # Piezoresponses of all lines
    piz_lines2 = []
    for j in range(y_dist):
        linex = np.linspace(x0, x1, x_dist)  # Make equally spaced
         ↪  point from x0 to x1
        linex2 = np.linspace(x2, x3, x_dist2)
        liney = np.zeros(y_dist)+(y0 + j)    # Make a list of the
         ↪  same y-value for the line
        liney2 = np.zeros(y_dist) + (y2 + j)
        horizontal_lines.append([linex, liney])
        horizontal_lines2.append([linex2, liney2])
        # Get the piezoresponse for the line
        linescan_pr = []    # The piezoresponse for each pixel of a
         ↪  line
        linescan_pr2 = []
        for u in range(x_dist):
```

```
        linescan_pr.append(pr_off_avg[int(liney[u]),
         ↪  int(linex[u]), :])  # Piezoresponse for a pixel at
         ↪  all voltages
        linescan_pr2.append(pr_off_avg[int(liney2[u]),
         ↪  int(linex2[u]), :])
    # Get the average piezoresponse for the line
    avg_linescan_pr = np.zeros(128)
    avg_linescan_pr2 = np.zeros(128)
    for pixel in range(x_dist):
        for pr in range(128):
            avg_linescan_pr[pr] += linescan_pr[pixel][pr]
            avg_linescan_pr2[pr] += linescan_pr2[pixel][pr]
    for q in range(128):
        avg_linescan_pr[q] = avg_linescan_pr[q]/x_dist
        avg_linescan_pr2[q] = avg_linescan_pr2[q] / x_dist
    piz_lines.append(avg_linescan_pr)   # Add the average
     ↪  responses from each line to the greater list
    piz_lines2.append(avg_linescan_pr2)

# Average the response from all the lines
avg_resp = np.zeros(128)
avg_resp2 = np.zeros(128)
for line in range(y_dist):
    for val in range(128):
        avg_resp[val] += piz_lines[line][val]
        avg_resp2[val] += piz_lines2[line][val]
for t in range(128):
    avg_resp[t] = avg_resp[t]/y_dist
    avg_resp2[t] = avg_resp2[t] / y_dist

data = voltage_data
plt.rc('axes', labelsize=20)  # fontsize of the x and y labels
plt.rc('xtick', labelsize=25)  # fontsize of the tick labels
plt.rc('ytick', labelsize=25)  # fontsize of the tick labels
fig, ax = plt.subplots(1, 3, figsize=(21, 6))
ax[0].imshow(image_data.reshape(128, 128, 512)[:, :, 0])
LW = 5
for i in range(len(horizontal_lines)):
    ax[0].plot(horizontal_lines[i][0], horizontal_lines[i][1],
     ↪  color='red', linewidth= LW)
    ax[0].plot(horizontal_lines2[i][0], horizontal_lines2[i][1],
     ↪  color='orange', linewidth=LW)
#plt.axis('off')
# Plot the average piezoresponse for the area
ax[1].plot(data['BEPS_Voltage'][0, 1:256:2], avg_resp * 2E5,
 ↪  color='red')
ax[2].plot(data['BEPS_Voltage'][0, 1:256:2], avg_resp2 * 2E5,
 ↪  color='orange')
```

```
    fig.tight_layout()
    fig.savefig('C:/Users/Olav Sandvik/OneDrive -
    ↪   NTNU/10.semester/Figures/OakRidge/PiezoArea' + str(name),
    ↪   dpi=100,
                pad_inches=1)
    return avg_resp


def draw_m_lines(image_data, voltage_data, name, x0, y0, x1, y1, x2,
↪   y2, x3, y3, x4, y4, x5, y5, x6, y6, x7, y7):
    def plot_piezoresponse(dist, color, linex, liney, name):
        plt.rc('axes', labelsize=20)  # fontsize of the x and y
        ↪   labels
        plt.rc('xtick', labelsize=35)  # fontsize of the tick labels
        plt.rc('ytick', labelsize=45)  # fontsize of the tick labels

        linescan_pr = []
        for i in range(dist):
            linescan_pr.append(pr_off_avg[int(liney[i]),
            ↪   int(linex[i]), :])
        linescan_pr = np.asarray(linescan_pr)
        fig, ax = plt.subplots(1, dist, figsize=(3*dist, 9),
        ↪   sharey=True)
        for j in range(dist):
            # The voltage is the same, but the piezoresponse is
            ↪   different for the different pixels.
            ax[j].plot(data['BEPS_Voltage'][0, 1:256:2],
            ↪   linescan_pr[j, :] * 2E5, color)
            ax[j].set_xticks([-10, 0, 10], ['-10', '',  '10'])
            ax[j].xaxis.set_tick_params(width=3, length=7) # Makes
            ↪   the ticks on the x-axis bigger
        ax[0].yaxis.set_tick_params(width=5, length=10)
        fig.savefig('C:/Users/Olav Sandvik/OneDrive -
        ↪   NTNU/10.semester/Figures/OakRidge/Stripes/StripeImage' +
        ↪   str(name) + '--' + str(color) + ' Stripe',
                     dpi=50, pad_inches=1)


    dist1 = int(np.sqrt( (x0-x1)**2 + (y0-y1)**2))
    dist2 = int(np.sqrt((x2 - x3) ** 2 + (y2 - y3) ** 2))
    dist3 = int(np.sqrt((x4 - x5) ** 2 + (y4 - y5) ** 2))
    dist4 = int(np.sqrt((x6 - x7) ** 2 + (y6 - y7) ** 2))

    linex1 = np.linspace(x0, x1, dist1)
    liney1 = np.linspace(y0, y1, dist1)
    linex2 = np.linspace(x2, x3, dist2)
    liney2 = np.linspace(y2, y3, dist2)
    linex3 = np.linspace(x4, x5, dist3)
```

```
    liney3 = np.linspace(y4, y5, dist3)
    linex4 = np.linspace(x6, x7, dist4)
    liney4 = np.linspace(y6, y7, dist4)
    data = voltage_data

    # Making the figure with stripes
    cut = [0.5, 0.5]
    minMax = []
    for j in range(2):
        minMax.append(min(np.array(data[:, :, 0].flatten())))
        minMax.append(max(np.array(data[:, :, 0].flatten())))
    norm = Normalize(vmin=cut[0] * min(minMax), vmax=cut[1] *
     ↪  max(minMax))
    fig1, ax = plt.subplots(1, 1, figsize=(8, 6))
    im = ax.imshow(image_data.reshape(128, 128, 512)[:, :, 0],
     ↪  cmap='viridis')
    fig1.colorbar(im)
    LW = 2
    color1 = 'red'
    color2 = 'darkorange'
    color3 = 'magenta'
    color4 = 'cyan'
    color5 = 'yellow'
    color6 = 'lime'
    color7 = 'maroon'
    color8 = 'hotpink'
    plt.plot(linex1, liney1, color=color1, linewidth= LW)
    plt.plot(linex2, liney2, color=color2, linewidth=LW)
    plt.plot(linex3, liney3, color=color3, linewidth=LW)
    plt.plot(linex4, liney4, color=color6, linewidth=LW)
    plt.axis('off')
    fig1.tight_layout()
    fig1.savefig('C:/Users/Olav Sandvik/OneDrive -
     ↪  NTNU/10.semester/Figures/OakRidge/Stripes/StripeImage' +
     ↪  str(name), dpi=100,
                pad_inches=1)
    plot_piezoresponse(dist1, color1, linex1, liney1, name)
    plot_piezoresponse(dist2, color2, linex2, liney2, name)
    plot_piezoresponse(dist3, color3, linex3, liney3, name)
    plot_piezoresponse(dist4, color6, linex4, liney4, name)


def pca(pca_amp,d1,d2,d3,volt_spec,type_,num_comp):

    X_vec = tl.tensor(pca_amp)
    pca = sk.decomposition.PCA(n_components=2)
    pca.fit(X_vec)
```

```
    # Comment/uncomment as necessary to normalize
    X_vec = (X_vec - np.min(X_vec)) / np.ptp(X_vec)
    nc = num_comp

    # Select decomposition type ('PCA' or 'NMF')
    decomposition_type = type_

    # Run decomposition
    if decomposition_type == 'NMF':
        clf = sk.decomposition.NMF(n_components=nc, random_state=42)
    elif decomposition_type == 'PCA':
        clf = sk.decomposition.PCA(n_components=nc, random_state=42)
    else:
        raise NotImplementedError('Available methods: "PCA", "NMF"')

    X_vec_t = clf.fit_transform(X_vec)
    exp_var_pca2 = clf.explained_variance_ratio_   # Explained
    ↪  variance
    components = clf.components_
    n_pixels = int(X_vec_t.shape[0]**(1/2))
    rows = int(np.ceil(float(nc)/5))
    cols = int(np.ceil(float(nc)/rows))
    gs1 = gridspec.GridSpec(rows, cols)
    fig1 = plt.figure(figsize = (15,7))
    for i in range(nc):
        ax1 = fig1.add_subplot(gs1[i])
        j = 0
        ax1.plot(volt_spec,components[i])
        ax1.set_title('Component ' + str(i + 1))
    fig1.savefig('C:/Users/Olav Sandvik/OneDrive -
    ↪  NTNU/10.semester/Figures/OakRidge/PCA/PCA_' + str(nc) +
    ↪  '_components_plot',
                     dpi=100, pad_inches=1)

    gs2 = gridspec.GridSpec(rows, cols)
    fig2 = plt.figure(figsize = (4*cols, 4*(1+rows//1.5)))
    for i in range(nc):
        ax2 = fig2.add_subplot(gs2[i])
        ax2.imshow(X_vec_t[:, i].reshape(d1, d2), cmap = 'jet')
        ax2.set_title('Component ' + str(i + 1))
    fig2.savefig('C:/Users/Olav Sandvik/OneDrive -
    ↪  NTNU/10.semester/Figures/OakRidge/PCA/PCA_' + str(nc) +
    ↪  '_components_map',
                     dpi=100, pad_inches=1)

    # Explained variance
    cum_sum_eigenvalues2 = np.cumsum(exp_var_pca2)
    fig3 = plt.figure(figsize=(8, 6))
```

```
    ax = fig3.add_subplot()

    plt.bar(range(0, len(exp_var_pca2)), exp_var_pca2, alpha=0.5,
    ↪  align='center', label='Individual explained variance')
    plt.step(range(0, len(cum_sum_eigenvalues2)),
    ↪  cum_sum_eigenvalues2, where='mid',
             label='Cumulative explained variance')
    plt.xticks([0, 1, 2, 3, 4, 5], ['1', '2', '3', '4', '5', '6'])
    print(exp_var_pca2)
    for i in range(len(exp_var_pca2)):
        ax.text(i-0.25, exp_var_pca2[i] + 0.05,
        ↪  str(round(exp_var_pca2[i]*100, 1)) + '%', fontsize=12)
    plt.ylabel('Explained variance')
    plt.xlabel('Principal component')
    plt.legend(loc='center right')
    fig3.savefig('C:/Users/Olav Sandvik/OneDrive -
    ↪  NTNU/10.semester/Figures/OakRidge/PCA/PCA_' + str(nc) +
    ↪  '_explainedVariance',
        dpi=100, pad_inches=1)


def plot_piezoresponse(data, indices, cut, rows, cols):
    voltages = plot_voltage_as_a_function_of_indices('no')
    fig = plt.figure(figsize=(2*cols, 2*rows))
    gs = gridspec.GridSpec(10*rows, 10*cols + 2, wspace=0.01,
    ↪  hspace=0.1)
    minMax= []
    factor = 100000
    for j in range(len(indices)):
        minMax.append(factor * min(np.array(data[:, :,
        ↪  indices[j]]).flatten()))
        minMax.append(factor * max(np.array(data[:, :,
        ↪  indices[j]]).flatten()))

    norm = Normalize(vmin=cut[0]*min(minMax),
    ↪  vmax=cut[1]*max(minMax))



    for i in range(len(indices)):
        ax = fig.add_subplot(gs[(i // cols) * 10 : (i // cols + 1) *
        ↪  9 + (i // cols) * 1 +1, (i % cols) * 10 : (i % cols) *
        ↪  10 + 9])
        ax.set_axis_off()
        ax.set_title(str(round(voltages[indices[i]], 1)) + ' Volt',
        ↪  fontsize=8)
        im = ax.imshow(factor * data[:, :, indices[i]], norm = norm,
        ↪  cmap='viridis')
```

```
    axx = plt.subplot(gs[:, -2:])   # The axis for the color bar
    cbar_ax = fig.add_axes(axx)
    fig.colorbar(cm.ScalarMappable(norm=norm, cmap='viridis'),
    ↪   cax=cbar_ax, extend='both')
    fig.set_size_inches(8, 6)
    fig.savefig('C:/Users/Olav Sandvik/OneDrive -
    ↪   NTNU/10.semester/Figures/OakRidge/Piezoresponse4', dpi=200,
                pad_inches=1)


def plot_topography(topo, cut):
    data = np.loadtxt(topo)
    fig = plt.figure(figsize=(8, 6))
    gs = gridspec.GridSpec(10, 10 + 5, wspace=0.01, hspace=0.1)
    minMax = []
    factor = 1000000000
    minMax.append(factor * min(np.array(data[:, :]).flatten()))
    minMax.append(factor * max(np.array(data[:, :]).flatten()))
    norm = Normalize(vmin=cut[0] * min(minMax), vmax=cut[1] *
    ↪   max(minMax))
    ax = fig.add_subplot(gs[:, :10])    # Add topography to figure
    ax.set_axis_off()
    mAp = 'viridis'
    im = ax.imshow(data, cmap=mAp)
    axx = plt.subplot(gs[:, -1:])  # The axis for the color bar
    cbar_ax = fig.add_axes(axx)
    fig.colorbar(cm.ScalarMappable(norm=norm, cmap=mAp),
    ↪   cax=cbar_ax, extend='both')
    fig.savefig('C:/Users/Olav Sandvik/OneDrive -
    ↪   NTNU/10.semester/Figures/OakRidge/Topography3', dpi=100,
                pad_inches=1)


def plot_pfm(data, cut):
    voltages = plot_voltage_as_a_function_of_indices('no')
    fig = plt.figure(figsize=(8, 6))
    gs = gridspec.GridSpec(10, 10 + 0, wspace=0.01, hspace=0.1)
    minMax= []
    factor = 10000
    minMax.append(factor * min(np.array(data[:, :, 0]).flatten()))
    minMax.append(factor * max(np.array(data[:, :, 0]).flatten()))
    norm = Normalize(vmin=cut[0]*min(minMax),
    ↪   vmax=cut[1]*max(minMax))

    ax = fig.add_subplot(gs[:, :10])
    ax.set_axis_off()
    im = ax.imshow(data[:, :, 0], cmap='viridis')
    cax=cbar_ax, extend='both')
```

```
    fig.savefig('C:/Users/Olav Sandvik/OneDrive -
    ↪  NTNU/10.semester/Figures/OakRidge/PFM_0V', dpi=100,
                pad_inches=1)



### Making my own colormap ####
cmap1 = colors.ListedColormap(['blue', 'yellow','orange', 'red',
 ↪  'magenta', 'cyan', 'black'])
cmap2 = colors.ListedColormap(['blue', 'orange', 'yellow', 'red',
 ↪  'magenta', 'cyan', 'black'])
cmap3 = colors.ListedColormap(['yellow', 'red', 'orange', 'blue',
 ↪  'magenta', 'cyan', 'black'])
cmap4 = colors.ListedColormap(['blue', 'orange', 'magenta', 'red',
 ↪  'yellow', 'cyan', 'black'])
boundaries = [0, 1, 2, 3, 4, 5, 6, 7]
norm = colors.BoundaryNorm(boundaries, cmap1.N, clip=True)
fa1 = 'dodgerblue'
fa2 = 'darkorange'
fa3 = 'gold'
cmapx = colors.ListedColormap([fa1, fa2, fa3, fa3])
boundaries2 = [0, 1, 2, 3]
norm2 = colors.BoundaryNorm(boundaries2, cmapx.N, clip=True)

### Difference in piezoresponse between +15V and -15V ####
plot_difference_between_images(pr_off_avg, [0.4, 0.4], [32, 96])

### Cluster analysis ###
cluster_analysis(2, data2_pr_off, cmap1, 'Cluster2', norm)
cluster_analysis(3, data2_pr_off, cmap2, 'Cluster3', norm)
cluster_analysis(4, data2_pr_off, cmap3, 'Cluster4', norm)
cluster_analysis(5, data2_pr_off, cmap4, 'Cluster5', norm)
cluster_analysis(6, data2_pr_off, 'jet', 'Cluster6')
cluster_analysis(3, data2_pr_off, cmapx, 'NEWCluster3_v2', norm2)


### Plot average hysteresis loop for an area ###
area1 = hysteresis_of_area(56, 36, 61, 41, data2_pr, data, 1)
area2 = hysteresis_of_area(80, 80, 85, 85, data2_pr, data, 2)
area3 = hysteresis_of_area(88, 96, 93, 101, data2_pr, data, 3)
area4 = hysteresis_of_2_area(80, 80, 85, 85, 88, 96, 93, 101,
 ↪  data2_pr, data, 4)


# # Plot the average of the bright and dark areas
avg_hysteresis = []
for i in range(len(area2)):
    avg_hysteresis.append((area2[i] + area3[i])/2)
```

```
avg_hysteresis = np.array(avg_hysteresis)
fig = plt.figure(figsize=(8,8))
plt.plot(data['BEPS_Voltage'][0, 1:256:2], avg_hysteresis * 2E5)
fig.savefig('C:/Users/Olav Sandvik/OneDrive -
↪   NTNU/10.semester/Figures/OakRidge/PiezoAreaAverage', dpi=100,
             pad_inches=1)

#### Line scans ####
draw_m_lines(46, 45, 55, 56,    # RED
              44, 92, 54, 102,     # ORANGE
              10, 110, 20, 100,    # MAGENTA
              30, 120, 40, 110,    # CYAN
              80, 10, 80, 24,   # YELLOW
              20, 68, 30, 78,    # LIME
              70, 85, 84, 85,    # MAROON
              90, 85, 90, 99,    # HOTPINK
              data2_pr, data, 1)

draw_m_lines(data2_pr, data, 3,
             46, 45, 53, 53,    # RED
             44, 92, 52, 99,    # ORANGE
             30, 120, 37, 112,    # MAGENTA
             70, 85, 80, 85)    # LIME

### Principle component analysis ###
X_vec = pca(data2_pr_off.reshape(16384,256),128,128,256,data['BEPS_V⌋
↪   oltage'][0,::2],type_ = 'PCA', num_comp =
↪   6)
X_vec = pca(data2_pr_off.reshape(16384,256),128,128,256,data['BEPS_V⌋
↪   oltage'][0,::2],type_ = 'PCA', num_comp =
↪   4)



### Plotting the piezoresponse as a function of voltage
indices = [0, 11, 22, 32, 64, 75, 86, 96]
plot_piezoresponse(pr_off_avg, indices, cut=[0.4, 0.4], rows=2,
↪   cols=4)



### Plot topography
plot_topography('Survey_EM00014_topo.txt', cut=[0.999, 0.999])

### Plot PFM
plot_pfm(pr_off_avg, cut=[0.5, 0.5])
```

Appendix G

MatLab code for analysis of EBSD data

This appendix presents the MatLab code used to analyze the EBSD data and produce several of the plots presented in section 4.4.

```
% ErMnO3
% 2022-05-03
% Håkon Wiik Ånes (hakon.w.anes@ntnu.no)
% Mofidied by Olav Wadseth Sandvik

clear all
home

res = '-r150';
plotx2east
plotzIntoPlane

dir_kp = 'C:\Users\Olav Sandvik\OneDrive -
↪  NTNU\10.semester\Results\EBSD_experiment\EBSD';
dir_mtex = 'C:\Users\Olav Sandvik\OneDrive -
↪  NTNU\10.semester\MatLab_EBSD\Plots\Pos5';

lattice_parameters = [6.1 6.1 11];
angles = [90 90 120] * degree;
cs = crystalSymmetry('622', lattice_parameters, angles, 'mineral',
↪  'ErMnO3');

ebsd = EBSD.load(fullfile(dir_kp, 'xmap_refori.ang'), cs,...
    'convertEuler2SpatialReferenceFrame', 'setting 2')

% Define ROI
dx = ebsd.y(2) - ebsd.y(1);
roi = [108 62 55 55]; % In EBSD scan unit, um
```

```
% Inspect ROI
figure
plot(ebsd, ebsd.ci)
mtexColorMap black2white
rectangle('position', roi, 'edgecolor', 'r', 'linewidth', 2)

% Restrict data to ROI
ebsd = ebsd(inpolygon(ebsd, roi))

% %% Plot normalized cross-correlation (NCC) score
figure
plot(ebsd, ebsd.ci)
mtexColorbar('title', 'NCC')
mtexColorMap black2white
export_fig(fullfile(dir_mtex, 'maps_ncc.png'), res)

%% Filter data based on NCC score
ebsd2 = ebsd;
ebsd2(ebsd2.ci < 0.21).phase = -1;

%% Reconstruct grains
[grains, ebsd2.grainId, ebsd2.mis2mean] = calcGrains(ebsd2,
↪   'angle',...
    5*degree);

%% Plot IPF color key
ipfkey = ipfHSVKey(ebsd.CS);

figure
plot(ipfkey)
export_fig(fullfile(dir_mtex, 'ipfkey.png'), res)

% Plot IPF color maps and IPF density plots
directions = {xvector, yvector, zvector};
titles = {'x', 'y', 'z'};
for i=1:3
    ipfkey.inversePoleFigureDirection = directions{i};
    omcolor = ipfkey.orientation2color(ebsd2.orientations);
% IPF maps
    figure
    plot(ebsd2, omcolor)
    hold on
    export_fig(fullfile(dir_mtex, ['maps_ipf' titles{i} '.png']),
↪   res)

    % IPF density plots
    figure
```

```
    plotIPDF(ebsd2.orientations, omcolor, directions{i}, 'all')
    export_fig(fullfile(dir_mtex, ['ipf' titles{i} '_scatter.png']),
 ↪  res)
end

%% (0001) pole figure
figure
plotPDF(ebsd2.orientations, Miller(0, 0, 1, ebsd.CS), 'grid', 'all')
export_fig(fullfile(dir_mtex, 'pf0001_scatter.png'), res)

%% Unit cell
cS = crystalShape.hex(ebsd.CS);

%% Plot orientation map with unit cells from big grains
grains_ermno3 = grains('indexed');
big_grains = grains_ermno3(grains_ermno3.grainSize > 200);
big_grains_id = big_grains.id;

for i=1:3
    ipfkey.inversePoleFigureDirection = directions{i};
    omcolor = ipfkey.orientation2color(ebsd2.orientations);

    figure
    plot(ebsd2, omcolor)
    hold on
    plot(grains_ermno3.boundary)
    hold on
    plot(big_grains, 0.5*cS, 'linewidth', 2, 'colored')
    legend('off')
    export_fig(fullfile(dir_mtex,...
        ['maps_grains_ipf' titles{i} '_cell.png']), res)
end

%% Plot map of misorientation to mean orientation within each grain
figure
plot(ebsd2('indexed'), ebsd2('indexed').mis2mean.angle / degree)
caxis([0, 3])
mtexColorbar('title', 'Misorientation to mean orientation [deg]')
mtexColorMap LaboTeX
hold on
plot(grains_ermno3.boundary)
export_fig(fullfile(dir_mtex, 'maps_grains_mis2mean.png'), res)

%% Plot map of kernel average misorientation (KAM)
kam = ebsd2.KAM;

figure
plot(ebsd2, kam / degree)
```

```
caxis([0, 0.5])
mtexColorbar('title', 'Kernel average misorientation [deg]')
mtexColorMap LaboTeX
hold on
plot(grains_ermno3.boundary)
export_fig(fullfile(dir_mtex, 'maps_grains_kam.png'), res)

%% Plot map of grain orientation spread (GOS)
figure
plot(grains_ermno3, grains_ermno3.GOS / degree)
caxis([0, 1.5])
mtexColorbar('title', 'Grain orientation spread [deg]')
mtexColorMap LaboTeX
hold on
plot(grains_ermno3.boundary)
export_fig(fullfile(dir_mtex, 'maps_grains_gos.png'), res)

%% Plot disorientation color key
ckey2 = axisAngleColorKey(ebsd2('indexed').CS);
ckey2.oriRef = grains(ebsd2('indexed').grainId).meanOrientation;
ckey2.maxAngle = 1 * degree;

figure
plot(ckey2)
export_fig(fullfile(dir_mtex, 'color_key_disori.png'), res)

%% Plot disorientation color map
omcolor = ckey2.orientation2color(ebsd2('indexed').orientations);

figure
plot(ebsd2('indexed'), omcolor)
hold on
plot(grains_ermno3.boundary)
export_fig(fullfile(dir_mtex, 'maps_grains_disori.png'), res)

%% Write data to file

% Grains
gam = ebsd2.grainMean(kam);
gam(isnan(gam)) = -1;
fid = fopen(fullfile(dir_mtex, 'grains.txt'), 'w+');
fprintf(fid, '#id,phase,size,gos,gam\n');
dataMat = [...
    grains.id,...
    grains.phase,...
    grains.grainSize,...
    grains.GOS,...
    gam,...
```

```
];
fprintf(fid, '%i,%i,%i,%.5f,%.5f\n', dataMat');
fclose(fid);

% KAM
fid = fopen(fullfile(dir_mtex, 'kam.txt'), 'w+');
fprintf(fid, 'kam\n');
fprintf(fid, '%.5f\n', ebsd2('indexed').KAM);
fclose(fid);

% Misorientation to mean orientation angle
fid = fopen(fullfile(dir_mtex, 'mis2mean.txt'), 'w+');
fprintf(fid, 'mis2mean\n');
fprintf(fid, '%.5f\n', ebsd2('indexed').mis2mean.angle);
fclose(fid);

close all force
sprintf('Done with process')
```

Appendix H

MatLab code for simulating grain orientations from EBSD data

This appendix presents the MatLab code used to produce the figures that compare grain orientation and ferroelectric domains in section 4.4. In addition, it was also utilized to produce the unit cells seen in the simulated strain figures in section 6.3.

```
% ErMnO3
% 2022-05-03
% Håkon Wiik Ånes (hakon.w.anes@ntnu.no)
% Modified by Olav Wadseth Sandvik

clear all
home

res = '-r200';
plotx2east
plotzIntoPlane

dir_kp = 'C:\Users\Olav Sandvik\OneDrive -
 ↪  NTNU\10.semester\Results\EBSD_experiment\EBSD';
dir_mtex = 'C:\Users\Olav Sandvik\OneDrive -
 ↪  NTNU\10.semester\MatLab_EBSD\Plots';

lattice_parameters = [6.1 6.1 11];
angles = [90 90 120] * degree;
cs = crystalSymmetry('622', lattice_parameters, angles, 'mineral',
 ↪  'ErMnO3');

ebsd = EBSD.load(fullfile(dir_kp, 'xmap_refori.ang'), cs,...
    'convertEuler2SpatialReferenceFrame', 'setting 2')

%% Filter data based on NCC score
ebsd2 = ebsd;
```

```
ebsd2(ebsd2.ci < 0.21).phase = -1;

%% Reconstruct grains
[grains, ebsd2.grainId, ebsd2.mis2mean] = calcGrains(ebsd2,
↪  'angle',...
    5*degree);

%% Unit cell
cS = crystalShape.hex(ebsd.CS);

%% Big grains
grains_ermno3 = grains('indexed');
big_grains = grains_ermno3(grains_ermno3.grainSize > 400);
big_grains(1)


%% Make the figure
ipfkey = ipfHSVKey(ebsd.CS);
ipfkey.inversePoleFigureDirection = xvector;
omcolor = ipfkey.orientation2color(ebsd2.orientations);

% Simulated grain
ori1 = orientation.byEuler([70.5 99.8 146.7] * degree, cs);

figure
plot([100 100] + ori1*cS*20, 'linewidth', 1, 'colored')
legend('off')


%% Close figures and show that the process is finished
%close all force
sprintf('Done with process')
```

Olav Wadseth Sandvik

Domain Engineering in Polycrystalline ErMnO3 Using Strain- and Electrical Fields

NTNU
Norwegian University of
Science and Technology